Layer-specific multiscale mechanical modeling of arterial structures with evolving fiber configurations

Mohsen Nakhaei

N°d'ordre NNT : 2020LYSEM014

THÈSE DE DOCTORAT DE L'UNIVERSITÉ DE LYON

opérée au sein de
École des Mines de Saint-Étienne
École Doctorale N° 488
(Sciences, Ingénierie, Santé)
Spécialité de Doctorat: Mécanique et Ingénierie

par

Mohsen Nakhaei

Sujet de thèse :

LAYER-SPECIFIC MULTISCALE MECHANICAL MODELING OF ARTERIAL STRUCTURES WITH EVOLVING FIBER CONFIGURATIONS

Soutenue le 10/07/20 devant le jury composé de

Rapporteurs :	Prof. Christian Hellmich	Technische Universität Wien
	Dr. Daniel George (HDR)	University of Strasbourg
Examinateurs :	Prof. Katherine Yanhang Zhang	Boston University
	Prof. Giuseppe Vairo	University of Rome Tor Vergata
	Prof. Pierre Badel	University of Lyon

Co-directeur : Dr. Claire Morin
Directeur : Prof. Stéphane Avril

Spécialités doctorales	Responsables :	Spécialités doctorales	Responsables
SCIENCES ET GENIE DES MATERIAUX	K. Wolski Directeur de recherche	MATHEMATIQUES APPLIQUEES	O. Roustant, Maître-assistant
MECANIQUE ET INGENIERIE	S. Drapier, professeur	INFORMATIQUE	O. Boissier, Professeur
GENIE DES PROCEDES	F. Gruy, Maître de recherche	SCIENCES DES IMAGES ET DES FORMES	JC. Pinoli, Professeur
SCIENCES DE LA TERRE	B. Guy, Directeur de recherche	GENIE INDUSTRIEL	N. Absi, Maitre de recherche
SCIENCES ET GENIE DE L'ENVIRONNEMENT	D. Graillot, Directeur de recherche	MICROELECTRONIQUE	Ph. Lalevée, Professeur

EMSE : Enseignants-chercheurs et chercheurs autorisés à diriger des thèses de doctorat (titulaires d'un doctorat d'État ou d'une HDR)

ABSI	Nabil	MR	Génie industriel	CMP
AUGUSTO	Vincent	CR	Image, Vision, Signal	CIS
AVRIL	Stéphane	PR2	Mécanique et ingénierie	CIS
BADEL	Pierre	MA(MDC)	Mécanique et ingénierie	CIS
BALBO	Flavien	PR2	Informatique	FAYOL
BASSEREAU	Jean-François	PR	Sciences et génie des matériaux	SMS
BATTON-HUBERT	Mireille	PR2	Sciences et génie de l'environnement	FAYOL
BEIGBEDER	Michel	MA(MDC)	Informatique	FAYOL
BLAYAC	Sylvain	MA(MDC)	Microélectronique	CMP
BOISSIER	Olivier	PR1	Informatique	FAYOL
BONNEFOY	Olivier	PR	Génie des Procédés	SPIN
BORBELY	Andras	MR(DR2)	Sciences et génie des matériaux	SMS
BOUCHER	Xavier	PR2	Génie Industriel	FAYOL
BRODHAG	Christian	DR	Sciences et génie de l'environnement	FAYOL
BRUCHON	Julien	MA(MDC)	Mécanique et ingénierie	SMS
CAMEIRAO	Ana	MA(MDC)	Génie des Procédés	SPIN
CHRISTIEN	Frédéric	PR	Science et génie des matériaux	SMS
DAUZERE-PERES	Stéphane	PR1	Génie Industriel	CMP
DEBAYLE	Johan	MR	Sciences des Images et des Formes	SPIN
DEGEORGE	Jean-Michel	MA(MDC)	Génie industriel	Fayol
DELAFOSSE	David	PR0	Sciences et génie des matériaux	SMS
DELORME	Xavier	MA(MDC)	Génie industriel	FAYOL
DESRAYAUD	Christophe	PR1	Mécanique et ingénierie	SMS
DJENIZIAN	Thierry	PR	Science et génie des matériaux	CMP
BERGER-DOUCE	Sandrine	PR1	Sciences de gestion	FAYOL
DRAPIER	Sylvain	PR1	Mécanique et ingénierie	SMS
DUTERTRE	Jean-Max	MA(MDC)		CMP
EL MRABET	Nadia	MA(MDC)		CMP
FAUCHEU	Jenny	MA(MDC)	Sciences et génie des matériaux	SMS
FAVERGEON	Loïc	CR	Génie des Procédés	SPIN
FEILLET	Dominique	PR1	Génie Industriel	CMP
FOREST	Valérie	MA(MDC)	Génie des Procédés	CIS
FRACZKIEWICZ	Anna	DR	Sciences et génie des matériaux	SMS
GARCIA	Daniel	MR(DR2)	Sciences de la Terre	SPIN
GAVET	Yann	MA(MDC)	Sciences des Images et des Formes	SPIN
GERINGER	Jean	MA(MDC)	Sciences et génie des matériaux	CIS
GOEURIOT	Dominique	DR	Sciences et génie des matériaux	SMS
GONDRAN	Natacha	MA(MDC)	Sciences et génie de l'environnement	FAYOL
GONZALEZ FELIU	Jesus	MA(MDC)	Sciences économiques	FAYOL
GRAILLOT	Didier	DR	Sciences et génie de l'environnement	SPIN
GROSSEAU	Philippe	DR	Génie des Procédés	SPIN
GRUY	Frédéric	PR1	Génie des Procédés	SPIN
HAN	Woo-Suck	MR	Mécanique et ingénierie	SMS
HERRI	Jean Michel	PR1	Génie des Procédés	SPIN
KERMOUCHE	Guillaume	PR2	Mécanique et Ingénierie	SMS
KLOCKER	Helmut	DR	Sciences et génie des matériaux	SMS
LAFOREST	Valérie	MR(DR2)	Sciences et génie de l'environnement	FAYOL
LERICHE	Rodolphe	CR	Mécanique et ingénierie	FAYOL
MALLIARAS	Georges	PR1	Microélectronique	CMP
MOLIMARD	Jérôme	PR2	Mécanique et ingénierie	CIS
MOUTTE	Jacques	CR	Génie des Procédés	SPIN
NAVARRO	Laurent	CR		CIS
NEUBERT	Gilles			FAYOL
NIKOLOVSKI	Jean-Pierre	Ingénieur de recherche	Mécanique et ingénierie	CMP
NORTIER	Patrice	PR1	Génie des Procédés	SPIN
O CONNOR	Rodney Philip	MA(MDC)	Microélectronique	CMP
PICARD	Gauthier	MA(MDC)	Informatique	FAYOL
PINOLI	Jean Charles	PR0	Sciences des Images et des Formes	SPIN
POURCHEZ	Jérémy	MR	Génie des Procédés	CIS
ROUSSY	Agnès	MA(MDC)	Microélectronique	CMP
ROUSTANT	Olivier	MA(MDC)	Mathématiques appliquées	FAYOL
SANAUR	Sébastien	MA(MDC)	Microélectronique	CMP
SERRIS	Eric	IRD		FAYOL
STOLARZ	Jacques	CR	Sciences et génie des matériaux	SMS
TRIA	Assia	Ingénieur de recherche	Microélectronique	CMP
VALDIVIESO	François	PR2	Sciences et génie des matériaux	SMS
VIRICELLE	Jean Paul	DR	Génie des Procédés	SPIN
WOLSKI	Krzystof	DR	Sciences et génie des matériaux	SMS
XIE	Xiaolan	PR0	Génie industriel	CIS
YUGMA	Gallian	CR	Génie industriel	CMP

Mise à jour : 30/08/2018

Acknowledgements

First of all, I would like to express my great gratitude to my advisors, Prof. Stéphane Avril and Dr. Claire Morin, for their continuous support and guidance during my Ph.D. They gave me the great opportunities to work on various interesting topics such as large deformation continuum micromechanics and nonlinear finite element methods. Their insightful comments were very inspiring and challenging, which enriched this thesis.

I also gratefully acknowledge the opportunity of working at Multi-Scale Tissue Biomechanics Lab at Boston University. I would like to express my great appreciation to Prof. Katherine Yanhang Zhang for giving me the opportunity to obtain a deeper perspective of experimental tests and become familiar with developing different constitutive modelings.

I am also grateful to the rest of the wonderful committee members, Prof. Christian Hellmich, Dr. Daniel Georg, Prof. Pierre Badel, and Prof. Giuseppe Vairo, for their insightful comments and suggestions to this thesis work. I have been greatly inspired by the discussion with them.

I would like to thank my lab mates at École des Mines de Saint-Étienne and also at Boston University, too many to list here, who have been excellent sources of inspiration and knowledge.

And lastly, I would like to thank my family for all of their supports, without their unconditional love, encouragement, and spiritual support, this would not have been possible.

Thank you all.

Contents

List of Figures

List of Tables

Nomenclature

Variable or symbol	Description
circ	circumferential direction
rad	radial direction
RVE	representative volume element
SMC	smooth muscle cell
$\mathbb{A}$	fourth-order strain rate concentration tensor
$\mathbb{A}^{\infty}$	fourth-order eigenstrain rate-to-spin concentration tensor in the Eshelby inhomogeneity problem
a_i	half length of the principal axes of the ellipsoidal inclusion
$\mathbb{C}$	fourth-order hypo-elastic stiffness tensor
$\mathbb{C}_0$	fourth-order hypo-elastic stiffness tensor of the matrix of the Eshelby problem
$\mathbb{C}_I$	fourth-order hypo-elastic stiffness tensor of the inclusion of the Eshelby problem
$\mathbb{C}_{hom}$	homogenized fourth-order hypo-elastic stiffness tensor
$\mathbb{C}_r^{eq}$	fourth-order equivalent "stiffness" tensor of phase r accounting for the objective rate
$\mathcal{D}$	dissipation of the system
$\mathcal{D}_1$	intrinsic dissipation of the system
$\mathcal{D}_2$	thermal dissipation of the system
$\boldsymbol{d}$	second-order microscopic Eulerian strain rate tensor
$\boldsymbol{D}$	second-order macroscopic Eulerian strain rate tensor
$\boldsymbol{D}_0$	applied second-order macroscopic Eulerian strain rate tensor in the Eshelby problem

Variable or symbol	Description
d	characteristic length of the heterogeneities
d_2	characteristic length of the heterogeneities of the lower scale representative volume element
$\boldsymbol{d}_r$	second-order microscopic averaged Eulerian strain rate in phase r
$\boldsymbol{d}_M$	second-order microscopic averaged Eulerian strain rate in the matrix phase
dt	time increment
E	Young's modulus
$\underline{e}_r$, $\underline{e}_\theta$, $\underline{e}_\phi$	spherical base vectors
f	volume fraction
$\boldsymbol{f}$	second-order microscopic deformation gradient
$\boldsymbol{F}$	second-order macroscopic deformation gradient
$\mathcal{G}$	Gibbs thermodynamic potential
$\mathbb{I}$	fourth-order identity tensor
$\boldsymbol{I}$	second-order identity tensor
$\mathbb{J}$	volumetric part of the second-order identity tensor
$\mathbb{K}$	deviatoric part of the second-order identity tensor
k	bulk modulus
l	characteristic length of the representative volume element
l_2	characteristic length of a lower scale representative volume element
$\mathcal{L}$	characteristic length of the arterial structure or of the applied loading
$\mathbb{L}^{Esh}$	fourth-order eigenstrain rate-to-velocity gradient concentration tensor in the Eshelby problem
M	denotes the matrix phase
N	number of inclusion phases

Variable or symbol	Description
$\underline{n}$	outward-pointing unit normal vector
$\underline{n}_i$	orthonormal basis of vectors defining the inclusion orientation in the Eshelby problem
P	fiber straightness
$\mathcal{P}^{ext}$	power of external traction forces
$\mathcal{P}^{int}$	power of internal forces
$\mathbb{P}_I$	fourth-order Hill tensor
$\underline{q}$	outward heat flux vector
$\mathbb{R}$	fourth-order strain rate-to-spin concentration tensor
$\mathbb{R}_r$	fourth-order strain rate-to-spin concentration tensor of phase r
$\mathbb{R}^{Esh}$	fourth-order eigenstrain rate-to-spin concentration tensor in the Eshelby problem
$\mathbb{R}^{\infty}$	fourth-order eigenstrain rate-to-spin concentration tensor in the Eshelby inhomogeneity problem
s	entropy per unit mass (also called specific entropy)
$\mathbb{S}^{Esh}$	fourth-order eigenstrain rate-to-strain rate concentration tensor in the Eshelby problem
T	absolute temperature
$\underline{t}$	traction forces
t	time
$\underline{v}$	microscopic velocity field
$\underline{x}$	microscopic location vector
δ_{ij}	Kronecker delta
$\partial\Omega$	boudary surface of the RVE
$\boldsymbol{\eta}$	microscopic second-order eigenstrain rate tensor

Variable or symbol	Description
θ	The co-latitudinal angle between inclusion and the global coordinate system
μ	shear modulus
ν	Poisson's ratio
ν_0	Poisson's ratio of the matrix of the Eshelby problem
ρ	mass density
$\boldsymbol{\sigma}$	microscopic second-order Cauchy stress tensor
$\boldsymbol{\Sigma}$	macroscopic second-order Cauchy stress tensor
ϕ	The longitudinal angle between inclusion and the global coordinate system
ψ	Helmholtz free energy per unit mass
$\boldsymbol{\Omega}$	second-order, skew symmetric, spin tensor
$\boldsymbol{\omega}$	second-order, skew symmetric, microscopic velocity gradient
Ω	volume of the RVE
Ω_I	volume of the ellipsoidal inclusion
ω_i	aspect ratios of the ellipsoidal inclusion
cos	cosine function
$D(.)/Dt = \dot{(.)}$	material derivative of quantity (.)
$\underline{\text{div}}$	divergence operator
$\underline{\text{grad}}$	gradient operator
tan	tangent function
$\tan^{-1}$	arc tangent function (inverse of the tangent function)
tr	trace operator

Variable or symbol	Description
^{T}	transpose operator
:	double contracted product
.	simple contracted product
$\triangle$	objective rate
$\|.\|$	norm of quantity
$\otimes$	dyadic product
$< . >$	spatial average operator over the RVE
Superscripts	Description
low	... of the lower scale RVE
up	... of the upper scale RVE
Subscripts	Description
$b-ad$	... of the collagen bundle phase in the adventitia RVE
$c-in$	... of the collagen phase in the interlamellar space RVE
$c-la$	... of the collagen phase in the lamellae RVE
$el-ad$	... of the elastin phase in the adventitia RVE
$el-in$	... of the elastin phase in the interlamellar space RVE
$el-la$	... of the elastin phase in the lamellae RVE
$f-b$	... of the fibrils in the collagen bundle RVE
M	... of matrix phase
$m-ad$	... of the matrix phase in the adventitia RVE
$m-b$	... of the matrix phase in the collagen bundle RVE
$m-in$	... of the matrix phase in the interlamellar space RVE

Subscripts	Description
$m-la$	... of the matrix phase in the lamellae RVE
M, I	... of the matrix phase of the lower scale RVE attached to the phase I of the upper scale RVE
r	... of phase r
r, I	... of phase r of the lower scale RVE attached to the phase I of the upper scale RVE

General Introduction

Arteries are part of the cardiovascular system which are responsible for circulating blood as a fluid which contains the oxygen and nutrients all over the body. The mechanics of arteries is an important topic as the artery is subjected to stresses occurring over a cyclic load (heartbeat), and it is a complex multiphase material containing active elements involved in large deformation. At present, there is still a pressing need to understand better how the mechanical properties of the artery are related to its structure, which can undergo millions of cycled distensions and still maintain a functional blood circulation. Therefore, there has been important efforts in mechanics to provide better insights regarding arterial structure-function relationships, the pathophysiology, and treatment of arterial diseases [64].

The mechanical properties of arteries originate from physical mechanisms (such as fiber rearrangement and elasticity) and mechanobiological effects (such as cell mechanosensing mediating tissue remodeling), which occur within the microstructure, and these aspects are significantly altered in cardiovascular diseases [67]. The significant role of the microstructure morphology and composition on arterial response motivated us to develop a detailed multi-scale model of the arterial wall. In this study, we developed a model, which accounts for the universal patterns across different scales in the two mechanically significant layers of arteries, namely the adventitia and the media, and introduce the different constituents making up the tissue at these different scales as phases into representative volume elements (RVE). Each phase volume fraction and morphology, as well as its ability to undergo load-driven rotations, were identified from literature and post-processing of multiphoton microscopic images [82]. The framework of finite strain continuum micromechanics [95] was employed in an incremental approach to compute the stress, strain, and phase reorientations, at each load increment. Within the adventitia, two scales were modeled to account

for both the fibril decrimping (through the progressive fibril reorientation at the lowest scale) and bundle realignment (at the macroscopic scale). Within the media, a stack of lamellae and interlamellar space was modeled, and the progressive reorientation of the collagen and elastin fibers were accounted for, all reorientation mechanisms being the source of the nonlinear response of the tissue. We organized this thesis as follows:

- **Chapter 1** presents background on arterial mechanics and structure as well as an introduction of the constitutive models. We described the structure of different layers of an artery at different scales, namely: tissue level (macroscopic), fiber level (microstructure), and fibril level (nanostructure). The main focus was on structure-mechanics relation and load-induced microstructural changes as well as the elementary constituents. The chapter ends with an introduction to the constitutive models of arterial tissue and an overview of the thesis.

- **Chapter 2** describes the theory of continuum micromechanics under large deformation. The thermodynamic formulation of the local hypoelastic constitutive relation was developed, and the homogenization techniques were explained. We construct algorithms for applying different homogeneous boundary conditions, namely strain rate and stress-driven load on the boundary of RVE. Then, the method was extended to a multi-scale approach for the hierarchical structure of heterogeneous materials.

- **Chapter 3** explains the application of the developed framework to model the arterial adventitia layer. The physical parameters of the model were determined through image processing and literature review. Then, we validated the model for the adventitia layer against the experimental data of the individual layer. A sensitivity analysis was performed to all parameters of the model which exhibit variations in the literature, and we studied their impact on mechanical response and microstructure evolution. Next, the ability of the model to capture the mechanical response of the whole artery as well as fiber evolution were investigated considering the arterial media layer as isotropic linear elastic.

- The extension of the model to the arterial media layer is described in **Chapter 4**. The physical parameters of the model were measured using

image processing, and some were determined from the literature. The experimental data of the media layer was employed to validate the arterial media layer individually. Then, we performed a sensitivity analysis to study the impact of the parameters on the model. Finally, we combined the two micromechanical model of the arterial media and adventitia layers to perform a uniaxial simulation of the whole artery and validate the model against the experimental results both in terms of mechanical response and microstructure evolution.

- The finite element implementation of the model and its application to the structural model of arteries are presented in **Chapter 5**. An updated Lagrangian finite element formulation was employed due to the incremental nature of the developed multi-scale constitutive model. First, we validated the finite element solver for a thin wall cylinder. Then, an internal pressure simulation was performed on the artery to study the mechanical response and microstructure evolution over time.

Introduction Générale

Au sein du système cardiovasculaire, les artères sont responsables de la circulation du sang, qui apporte l'oxygène et les nutriments dans tout le corps. Il est de ce fait primordial de maintenir l'intégrité mécanique des artères, et pour cela de caractériser la réponse mécanique des artères lorsque celle-ci est soumise aux contraintes liées au flux sanguin généré par les battements du cœur. Pour résister à ces fortes sollicitations, le tissu artériel est un matériau complexe, hétérogène, pouvant supporter de grandes déformations. À l'heure actuelle, il est toujours important de mieux comprendre comment les propriétés mécaniques de l'artère sont liées à sa microstructure, qui peut supporter des millions de sollicitations cycliques tout en maintenant une circulation sanguine fonctionnelle. Des efforts importants ont été déployés dans le domaine de la mécanique pour mieux comprendre les relations entre la structure et la fonction des artères, la physiopathologie et le traitement des maladies artérielles [64].

Les propriétés mécaniques des artères proviennent de mécanismes physiques (tels que le réarrangement et l'élasticité des fibres) et d'effets mécanobiologiques (tels que le remodelage des tissus par les cellules mécanosensibles), qui se produisent au sein de la microstructure, et ces aspects sont sensiblement modifiés dans les maladies cardiovasculaires [67]. Le rôle significatif de la morphologie et de la composition de la microstructure sur la réponse artérielle nous a motivé à développer un modèle multi-échelle détaillé de la paroi artérielle. Dans cette étude, nous avons élaboré un modèle qui tient compte de la morphologie tissulaire à différentes échelles dans les deux couches mécaniquement importantes des artères, à savoir l'adventice et la média. Les différents constituants qui composent le tissu à ces différentes échelles sont introduits en tant que phases dans des volumes élémentaires représentatifs (VER). Les fractions volumiques et la morphologie de chaque phase ont été identifiées à partir de la littérature et du

post-traitement d'images microscopiques multiphotoniques [82]. Le cadre de la micromécanique des milieux continus en transformations finies [95] a été utilisé dans une approche incrémentale pour calculer la contrainte, la déformation et les réorientations de phase, à chaque incrément de charge. En ce qui concerne l'adventice, deux échelles ont été modélisées pour tenir compte à la fois de la mise sous tension progressive des fibrilles (grâce à une réorientation progressive des fibrilles à l'échelle la plus basse) et du réalignement des faisceaux de fibres (à l'échelle mésoscopique). En ce qui concerne la média, un empilement de lamelles et d'espace interlamellaire a été modélisé, et la réorientation progressive des fibres de collagène et d'élastine a été prise en compte, tous les mécanismes de réorientation étant à l'origine de la réponse non linéaire du tissu. Nous avons organisé cette thèse de la manière suivante :

- Le **chapitre 1** présente le contexte de la mécanique et de la structure artérielle ainsi qu'une introduction des modèles constitutifs. Nous avons décrit la structure des différentes couches d'une artère à différentes échelles, à savoir : le niveau du tissu (macroscopique), le niveau des fibres (microstructure) et le niveau des fibrilles (nanostructure). L'accent a été mis sur la relation structure-mécanique et les changements microstructuraux induits par la charge, ainsi que sur les constituants élémentaires. Le chapitre se termine par une introduction aux modèles de comportement du tissu artériel et un aperçu de la thèse.

- Le **chapitre 2** décrit la théorie de la micromécanique du milieu continu dans le cadre des grandes transformations. La formulation thermodynamique de la relation de comportement hypoélastique locale est présentée, et les techniques d'homogénéisation sont expliquées. Nous construisons des algorithmes pour appliquer différentes conditions aux limites homogènes, à savoir la vitesse de déformation et la charge induite par la contrainte sur les bords du volume élémentaire représentatif. Ensuite, la méthode a été étendue à une approche multi-échelle pour prendre en compte la structure hiérarchique des matériaux hétérogènes.

- Le **chapitre 3** présente la modélisation de la couche d'adventice artérielle dans le cadre développé. Les paramètres physiques du modèle ont été déterminés par le traitement d'images et la revue de la littérature. Ensuite,

nous avons validé le modèle pour la couche adventitielle par rapport aux données expérimentales récoltées par des tests sur adventice seule. Une analyse de sensibilité a été effectuée pour tous les paramètres du modèle qui présentent des variations dans la littérature, et nous avons étudié leur impact sur la réponse mécanique et l'évolution de la microstructure. Ensuite, la capacité du modèle à capturer la réponse mécanique de l'artère entière ainsi que l'évolution des fibres ont été étudiées en considérant la média comme isotrope linéaire élastique.

- L'extension du modèle à la média est décrite au **chapitre 4**. Là encore, les paramètres physiques du modèle ont été mesurés à l'aide du traitement d'images, et certains ont été déterminés à partir de la littérature. Les données expérimentales de la média ont été utilisées pour valider individuellement la réponse mécanique de cette couche du tissu. Ensuite, nous avons effectué une analyse de sensibilité pour étudier l'impact des paramètres sur le modèle. Enfin, nous avons combiné les deux modèles micromécaniques de la média et de l'adventice pour effectuer une simulation uniaxiale de l'artère entière et valider le modèle par rapport aux résultats expérimentaux tant en termes de réponse mécanique que d'évolution de la microstructure.

- La mise en œuvre du modèle par éléments finis et son application à un modèle de structure des artères sont présentées au **chapitre 5**. Une formulation éléments finis lagrangienne actualisée a été utilisée en raison de la nature incrémentale du modèle constitutif multi-échelle développé. Tout d'abord, nous avons validé le solveur éléments finis pour un cylindre à paroi mince. Ensuite, une simulation de la pression interne a été réalisée sur l'artère pour étudier la réponse mécanique et l'évolution de la microstructure dans le temps.

1 Introduction - State of the art

Contents

1.1 Introduction to arterial structure and mechanics

The pathogenesis of many arterial diseases implies dysfunction and loss of the organization of the complex microstructure and components [120, 77, 102, 72, 83]. As prominent examples, structural changes due to aging, atherosclerosis, and aneurysm result in change of arterial mechanical properties [89, 120].

1.1.1 Multiscale Structure of arteries

Arterial tissues exhibit a vast diversity and variability among organs and species [149]. Still, the fundamental hierarchical organization of elastic arterial tissues has remained largely unchanged across most arterial tissues [145, 33], and can be described by means of the following morphological patterns:

- The macrostructure, with a characteristic length of 100 μm to 1 mm, features the three concentric layers of elastic arteries, namely the intima, the media, and the adventitia [145], see Fig. 1.1(B).

- Zooming out pieces of any of these three layers reveals that all layers host various biological cells: fibroblasts in the adventitia (with a characteristic length of 20-30 μm), smooth muscle cells (SMC) in the media (with a characteristic length of 50 μm) [112, 18], and endothelial cells in the intima (with a characteristic length of 50 μm).

- The entire domain outside these cells is called the extracellular matrix. The extracellular matrix is made of structural macromolecules, among which collagen and elastin are arranged hierarchically in networks of fibrils and fibers. The extracellular matrix appears as a composite with a characterisitic size of 50-200 μm, see Fig. 1.1(C). Within this extracellular space at this scale, different families of fibers (mainly collagen and elastin fibers) can be distinguished. Note that in the adventitia layer the collagen fibers are arranged in the form of collagen bundles (see Fig. 1.1(C) in red).

- Finally, the elementary constituents can be distinguished, namely the collagen fibrils, the elastin, and the ground substance.

The precise organization of each layer will be detailed in subsequent sections.

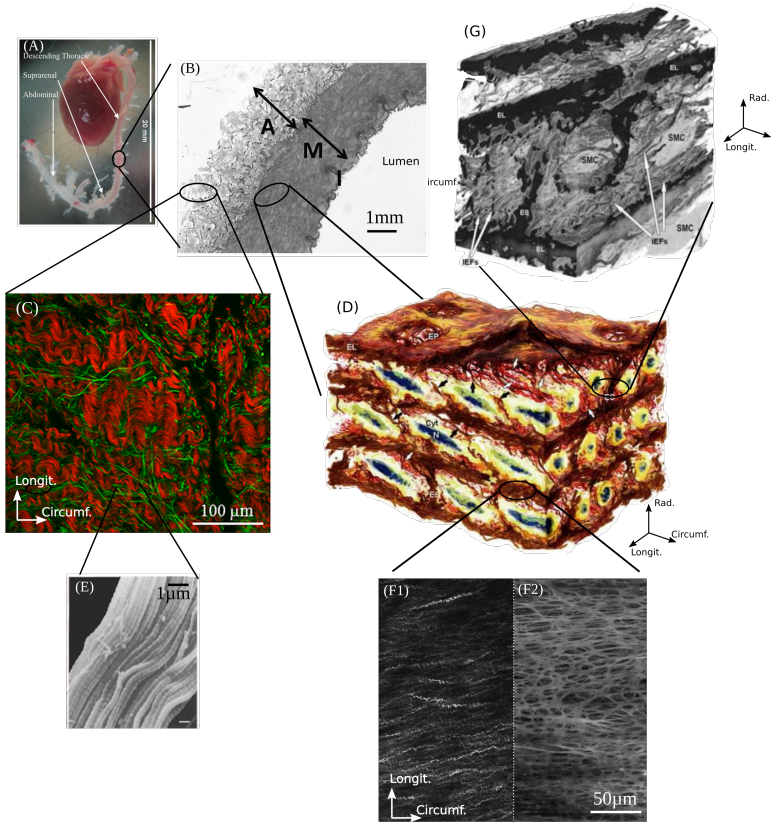

Figure 1.1: The hierarchical structure of arteries. (A) macroscopic artery of a mouse, taken from [74]; (B) the three layers of arterial wall, the adventitia tunica (A), the tunica media (M) and the intima tunica (I) from [112], by means of an electron micrograph; (C) the adventitia is made of an arrangement of collagen bundles (red) and elastin fibers (green) taken from [16], by means of multiphoton microscope; (D) the media is made of an arrangement of lamellae sheets and interlamellar space [100]; (E) the collagen bundles are made of an arrangement of collagen fibrils, as taken from [139], by means of electron microscopy; (F1) & (F2) respectively show the collagen and elastin fibers in the structure of lamellae sheets; (G) the structure of interlamellar space contains elastin, collagen fibers and SMC.

1.1.2 Macroscopic approach to the mechanics of arteries

Historically, different test benches have been developed to characterize the mechanical properties of arteries; they include uniaxial tensile tests on arterial strips [82, 63, 116, 144, 21, 10, 30, 154], planar biaxial tensile tests [38, 75, 160],

bulge-inflation tests [115, 86, 15], and tension-inflation tests [123, 46]. They all reveal a highly non linear mechanical response of arterial tissue, as exemplified in Fig. 1.2, [6, 29]. More precisely, at low applied stresses, the arterial tissue can be easily stretched, resulting in a very low stretch-stress slope. When the applied stress is increased, the tissue progressively stiffens, resulting in an increasing stretch-stress slope, whose microstructural origin is discussed in next section. Another interesting feature of the mechanical behavior of arteries is its anisotropy, although no clear conclusion could be drawn from the different papers [14, 82, 81, 22, 100]: it appears that the global anisotropy of arteries depends on the tissue location and on the species.

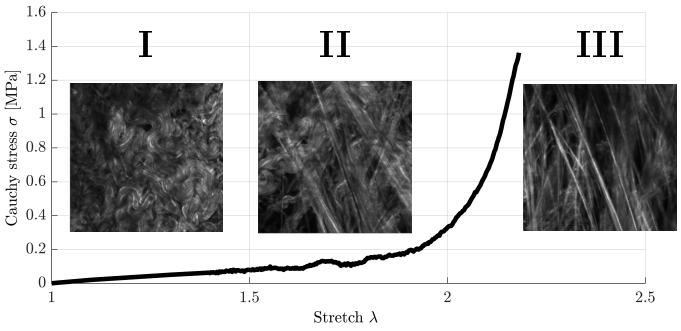

Figure 1.2: Non linear mechanical response under a uniaxial tensile test of a rabbit carotid artery. Collagen fibers are initially crimped (I), then start decrimping (II), and are stretched at large stresses (III).

1.1.3 Structure-mechanics relations

This highly non linear mechanical behavior follows from progressive changes in the arterial morphology: fibers in the tissue are crimped in the unloaded state; by applying a mechanical load, fibers become progressively stretched (see Fig. 1.2). It is widely accepted that the elastin fiber network bears the load when the latter is small [129, 149]. At larger loads, the progressive recruitment of collagen bundles in the adventitia allows them to bear the load and prevent the arteries from overdistension. Changes in the arterial morphology induce variations in the arterial stiffness [54].

1.2 The tunica adventitia

This paragraph focuses on the description of the extracellular matrix of the tunica adventitia from a mechanical point of view.

1.2.1 Role of the fibrous networks in the adventitia morphology

Two main constituents are known to play an important role in adventitia mechanics, namely the collagen bundles and the elastin fibers, which can be tracked by means of multiphoton microscopy, see Fig. 1.1(C) [16, 162, 123, 82]. The latter technique indeed reveals the local orientations of collagen and elastin fibers. First, several studies showed the very limited radial inclination of the fiber networks within the adventitia [114, 123]. We therefore choose to neglect it also in the sequel. Second, while elastin fibers are mainly oriented in the longitudinal direction, the orientation of collagen bundles in the unloaded configuration is more complex to determine due to crimping. Several contributions state that collagen bundles are preferentially aligned along the longitudinal directions [138, 20, 26], while others opt for a diagonal orientation (in the longitudinal-circumferential plane) [19].

1.2.2 Load-induced morphological changes

The adventitia is characterized by important load-induced morphological changes. The latter have been the topic of several studies, see e.g. [123, 19, 22]. They underline the impressive rearrangement capabilities of the collagen bundles: while highly crimped and apparently disorganised in the unloaded configuration [100, 114, 28], the collagen bundles are progressively recruited, i.e. they unfold, straighten, and progressively align towards the load direction [50, 12]. These features can be observed in uniaxial tension [82], biaxial tension [22, 81], and bulge-inflation tests [15], although the biaxial character of the applied load limits the reorientation effects [14]. These two reorientation processes of collagen bundles can also be quantified [17, 123, 22, 160, 82, 81]; two theories are mainly debated: (i) the reorientation of collagen bundles follows an affine kinematics, i.e. the apparent rotation of the fibers follows from the stretching of the tissue, while the fibers are firmly embedded in the matrix; (ii) the reorientation kinematics is larger than the affine kinematics and fibers have the ability to shear the surrounding

matrix to rotate. While the first theory is a good approximation for restricted deformation (such as the physiological deformation) [22, 82, 81], the non-affine kinematics cannot be neglected for larger deformation ranges [82]. Conversely, elastin fibers exhibit only limited load-induced orientation changes [17, 19, 82]. Finally, the preferential longitudinal orientation of the adventitial fiber networks explains the observed anisotropy of the adventitial tissue, namely: the adventitia is stiffer in the longitudinal direction than in the circumferential one [63, 147].

1.3 The tunica media

1.3.1 The media morphology

The tunica media is made of an arrangement of several medial lamellar units, see Fig. 1.1(D) [24, 100]. Each lamellar unit consists in a row of overlapping SMCs surrounded on the lower and upper sides by two concentric elastic lamellae (see Fig. 1.3(a)). More precisely, the elastic lamellae are made of a dense network of circumferentially-oriented elastic fibers [32, 133] (see Fig. 1.3(b)). They have large, round fenestrations, which serve as anchorages for SMCs [28]. Circumferentially-oriented, wavy collagen bundles run parallel to the elastic lamellae [24, 100, 133, 117, 57]. Between these elastic lamellae, the interlamellar space is made of SMCs. SMCs have an elongated shape, about 100-200μm of length and 5-10μm width [66], which display a radial tilting of about 20° and are mainly circumferentially oriented [18, 100]. Along the SMC, type III collagen fibrils contribute to the SMC cohesion and anchorage on the lamellae [24]. Thick radial elastin struts provide cohesion by bridging the lamellae layers together [28, 133, 79]. Finally, thin elastin radial fibers connect the SMC to both lamellae [110, 28].

1.3.2 Load-induced morphological changes

Several studies showed that lamellae of the media tend to be crimped in the unloaded configuration, while the load application leads to their progressive uncrimping, see e.g. [153, 157]. The SMCs also undergo a load-induced reorientation [18]. Still, reorientations occurring in the media are less pronounced than the ones occurring in the adventitia [22]. Besides, the preferred circumferential orientation of the medial fiber networks explains why the media is

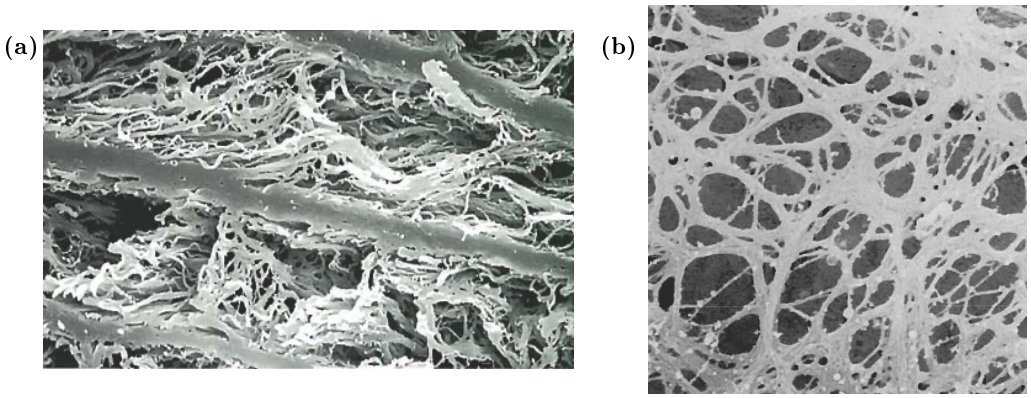

Figure 1.3: The structure of rat aorta media [139]. (a) The transverse section of media, magnification $\times 1,500$. (b) Close view of elastic lamellae, magnification $\times 11,000$.

stiffer in the circumferential direction than in the longitudinal one [100, 63, 147].

1.4 The tunica intima

The tunica intima is the inner layer of the arterial wall. The surface close to the lumen is covered by endothelial cells. From a mechanical point of view, the endothelial cells are sensitive to shear stresses applied by the blood flow on the arterial wall. The endothelial cells respond to this mechanical signal through the reorganization of their actin filament structure [101]. When subjected to high shear stresses, the endothelial cells are stretched along the blood flow direction, and the actin filaments are observed around the cell nucleus [101]. Furthermore, the endothelial cells active Nitric oxide (NO) pathway as an endothelium-derived relaxing factor which affects on SMCs [71].

A dense elastin layer, called the internal elastic lamina (see Fig. 1.4), separates the endothelial cells and the tunica media. Scanning electron microscopy and transmission electron microscopy studies revealed that elastin fibers are mostly longitudinally oriented in internal elastic lamina, while, in the media, the elastin fibers are mostly circumferentially oriented to resist the circumferential stress generated by blood pulsation [32].

Figure 1.4: Internal elastic lamina of rat aorta, magnification $\times 3,000$ [139].

1.5 The elementary constituents

1.5.1 Collagen fibers

Collagen is one of the main elementary and most abundant constituent of biological tissues such as bone, tendon, lung, skin, or arteries. Its main function is to provide structural stability to the tissues [141, 156]. There are more than 28 types of collagen, among which fibril-forming collagens such as types I and III play a major role in the structural mechanics of human tissues [141, 48]. Many studies focused on characterizing the mechanical properties of type I collagen molecules or of arrangements within fibrils or larger structures of this protein, see Table 1.1 for more details. When tested at the molecular scale or in the fibrillar dried state, collagen exhibits a Young's modulus in the range of a few GPa. At the fibrillar scale, in the wet state, the Young's modulus falls to a few hundreds of MPa.

Young's modulus E [MPa]	Specimen & experiment	Reference
2 - 200	Achilles tendon fibrils under atomic force microscopy different aqueous and ethanol environments	[48]
62	Turkey tendon under tensile test	[127]
100	The Achilles tendon of rats under tensile test.	[10]
100 - 800	Bovine Achilles tendon fibrils under atomic force microscopy hydrated collagen fibrils	[141]
350 - 650	hydrated collagen fibrils of Rat tail tendon tensile test	[73]
410 - 1310	hydrated collagen fibrils of Dermis of sea cucumber tensile test	[126]
430	hydrated collagen fibrils in a bovine Achilles tendon tensile test	[121]
1000 - 3900	hydrated collagen fibrils of Bovine Achilles tendon bending experiment by atomic force microscopy	[155]
1700 - 2700	air-dried collagen fibrils of Rat tail tendon tensile test	[73]
2000 - 7000	Bovine Achilles tendon fibrils under atomic force microscopy an-hydrated collagen fibrils	[141]
3750 - 11500	hydrated collagen fibrils of Rat tail tendon atomic force microscopy	[150]

Table 1.1: Overview of the range of values for the Young's modulus of collagen fibril and fiber found in the literature

The mechanical properties of type III collagen are different from the ones of type I collagen. According to our knowledge, the only investigation reporting mechanical properties for type III collagen fibrils relates to human placenta tissue. More precisely, atomic force microscopy on collagen fibrils type I and type III from human placenta was performed by [2] in the hydrated state in a phosphate buffered saline solution. They reported Young's modulus for type I collagen fibrils ranging from 600 kPa to 1.5 MPa and for type III collagen fibrils ranging from 100 kPa to 300 kPa [2].

1.5.2 Elastin fibers

Another main elementary component of arterial tissue is elastin (see Fig. 1.5), which provides its elasticity to arterial tissue; elastin also ensures that arteries can undergo several million deformation cycles without appreciable fatigue [51]. Regarding the mechanical characterization of elastin, the elastic modulus of intact purified elastic fibers from aortas was reported to be 0.3 MPa [10, 55], while the water-swollen, single elastin fiber taken from a bovine ligamentum nuchae [1]

has a Young's modulus up to 1.2 MPa. According to Gundiah et al. (2007), the difference in Young's moduli could be explained by the method for elastin extraction [51], the autoclaving method, as used in Aaron and Gosline (1981), providing higher stiffness values than alkali-treated elastin, as proposed by Burton (1954), see Table 1.2 for more details.

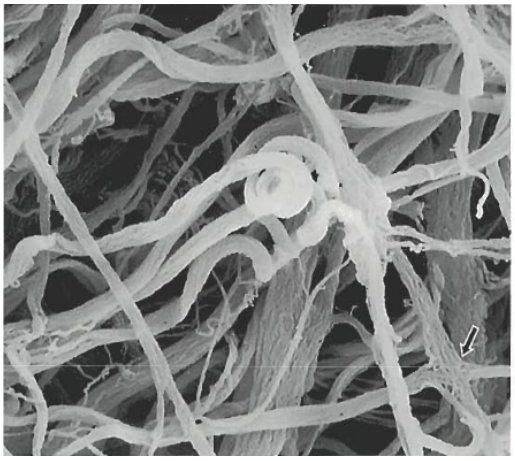

Figure 1.5: Elastin fibers of rat aortic adventitia, magnification $\times 5,500$ [139].

Elastin fiber E [MPa]	Specimen & experiment	Reference
0.24 - 0.7	elastin fibers of rat skin	[104]
0.3	Purified aorta	[10]
0.4 - 1.2	5-8 μm diameter, water-swollen Bovine ligamentum	[1]
0.6	ligamentum nuchae	[6]

Table 1.2: Overview of the range of values for the Young's modulus of elastin fiber found in the literature

1.5.3 Smooth muscle cells

The smooth muscle cells are active constituents of the arterial tissue: they can contract or relax in response to mechanical and/or chemical stimuli, which leads to corresponding changes in the arterial diameter. Thus, the mechanical behavior of the smooth muscle cells change depending on the environment [98, 65]. In the relaxed configuration, SMCs have a long and thin shape, which provides a large surface, and an ellipsoidal nucleus, representing about 5% of the total SMC volume. Contraction implies an important shortening of the SMC which is recovered upon relaxation [100]. This active property arises from the presence of

a dense network of actin-myosin filaments in their cytoplasm. Thanks to their properties, smooth muscle cells are responsible for regulating the rapid stress development in the artery as well as for sustaining the imposed stress [113, 111]. SMCs are oriented circumferentially with an inclination of about 20° in the radial direction [100]. The tensile stiffness of smooth muscle cells harvested from rat thoracic aortas ranges from 10 kPa in the relaxed condition to 100 kPa in the contracted state [98]. In other study the Young's modulus of young and old monkeys were measured by [161] as 4 kPa for young samples and 25 kPa for old samples.

1.5.4 Other constituents

These previously described main constituents are embedded in a soft ground substance, containing water, other cells, and proteins such as proteoglycans and glycosaminoglycans. Some mechanical properties of arteries such as viscoelasticity, permeability, and homeostasis have been shown to be related to these molecules [151].

1.6 State of the art on arterial constitutive models

The art of describing the physical behavior of materials through mathematical formulation according to the physical concepts and experimental observation is called constitutive modeling. A powerful constitutive model plays an important role in the predictivity of structural models. Computational models of biological tissue along with the experimental work accelerated our analysis about different organs to improve and speed up the clinical approaches. Recently, the development of numerical simulations increased dramatically to simulate different pathologies in order to explain, investigate, and predict the behavior of a pathology. These numerical models assist clinical trials in a rapid and low-cost way, which would reduce the required for expensive experiments [119, 146, 78, 69, 42]. However, these experiments remain an essential key to validate the model's assumptions. Finally, the validated model can be used to address questions that cannot be solved experimentally at this moment or treat the pathology in a patient-specific manner. Additionally, these models may enable the investigation in a clinical setting when a physician decides whether

or not a drug or a surgical procedure should be administered to a patient [60]. The main focus here is to develop arterial constitutive models, which are able to predict the elastic mechanical behavior of the tissue, although arterial tissue also exhibits inelastic behavior such as viscoelasticity, damage as well as remodeling and growth.

1.6.1 Hyperelastic models

Over the last decades, researchers have developed diverse models employing the framework of hyperelasticity to predict the mechanical behavior of arteries and to relate tissue structure to its mechanical functions [61, 131, 19, 18, 16]. These models are computationally efficient and precisely reproduce the macroscopic mechanical responses. However, most models remain phenomenological and do not address physical mechanisms and mechanobiological effects occurring within the microstructure of arteries or link these to the observed macroscopic mechanical responses [45, 62, 84].

Hyperelastic material models are based upon a potential function called strain energy density ψ that physically represents the mechanical energy stored in the body per unit volume of mass. In order to satisfy the objectivity requirement the strain energy density is written as a function of the right Cauchy-green deformation tensor $\psi(\boldsymbol{C})$, (whereby $\boldsymbol{C} = \boldsymbol{F}^T\boldsymbol{F}$ and $\boldsymbol{F}$ is the deformation gradient). The thermodynamical requirements for a hyperelastic material where free energy is equal to strain energy yield the relationship between stress and strain. Moreover, the hyperelastic materials exhibit zero dissipation under deformation, where the dissipation can be derived through Clausisus-Duhem expression [118] as,

$$\mathcal{D} = \boldsymbol{\pi} : \frac{1}{2}\frac{\partial \boldsymbol{C}}{\partial t} - \frac{\partial \psi}{\partial t}(\boldsymbol{C}(t)) = 0 \tag{1.1}$$

with $\boldsymbol{\pi}$, the Piola-Kirchhoff stress tensor reads as, $\boldsymbol{\pi} = 2\frac{\partial \psi(\boldsymbol{C})}{\partial \boldsymbol{C}}$. In order to use the hyperelastic models for fibrous soft tissues, in which the fibers are embedded in a soft ground substance; the strain energy density function is usually decomposed into two parts, the contribution of the matrix and the contributions of the fibers. Where the matrix strain energy represents the isotropic behavior ψ_{iso} and fibers strain energy is associated with anisotropic response ψ_{ani}. The fibers in the tissue introduced by planar discrete fiber families (n=2) with direction $\underline{e}_0^1$ and $\underline{e}_0^2$

in the reference configuration. Thus, in general, the strain energy function for the hyperelastic model of the arterial wall with two collagen families can be written as follows,

$$\psi(\boldsymbol{C}, \underline{e}_0^1, \underline{e}_0^2) = \psi_{iso}(\boldsymbol{C}) + \psi_{ani}(\boldsymbol{C}, \underline{e}_0^1, \underline{e}_0^2). \tag{1.2}$$

Based on invariant theory, a polynomial invariant basis is defined for the isotropic part $\psi_{iso}(\boldsymbol{C})$ as $I_{iso} = \{I_1, I_2, I_3\}$ and for anisotropic part $\psi_{ani}(\boldsymbol{C}, \underline{e}_0^1, \underline{e}_0^2)$ the invariant basis is $I_{ani} = \{I_1, I_2, I_3, I_4, I_5, I_6, I_7, I_8\}$, which leads to an isotropic function for the strain energy density. Usually for sake of simplicity and in order to reduce the material parameters one can write the strain energy density in terms of some of its invariant basis [61], as:

$$\psi(\boldsymbol{C}, \underline{e}_0^1, \underline{e}_0^2) = \psi_{iso}(I_1) + \psi_{ani}(I_4, I_6), \tag{1.3}$$

where,

$$\begin{aligned}
I_1 &= \text{tr}\, \boldsymbol{C} \\
I_2 &= \frac{1}{2}\left[(\text{tr}\, \boldsymbol{C})^2 + \text{tr}\, (\boldsymbol{C})^2\right] \\
I_3 &= \det \boldsymbol{C} \\
I_4 &= \boldsymbol{C} : \underline{e}_0^1 \otimes \underline{e}_0^1 \\
I_5 &= \boldsymbol{C}^2 : \underline{e}_0^1 \otimes \underline{e}_0^1 \\
I_6 &= \boldsymbol{C} : \underline{e}_0^2 \otimes \underline{e}_0^2 \\
I_7 &= \boldsymbol{C}^2 : \underline{e}_0^2 \otimes \underline{e}_0^2 \\
I_8 &= (\underline{e}_0^1 \cdot \underline{e}_0^2)\underline{e}_0^2 \cdot \boldsymbol{C}^2 \underline{e}_0^2
\end{aligned} \tag{1.4}$$

Then the corresponding second Piola-Kirchhoff stress tensor is,

$$\begin{aligned}
\boldsymbol{\pi} &= 2f_M \frac{\partial \psi_{iso}(I_1)}{\partial \boldsymbol{C}} + 2f_f \frac{\partial \psi_{ani}(I_4, I_6)}{\partial \boldsymbol{C}} \\
&= 2f_M \left[\frac{\partial \psi_{iso}}{\partial I_1}\frac{\partial I_1}{\partial \boldsymbol{C}}\right] + 2f_f \left[\frac{\partial \psi_{ani}}{\partial I_4}\frac{\partial I_4}{\partial \boldsymbol{C}} + \frac{\partial \psi_{ani}}{\partial I_5}\frac{\partial I_5}{\partial \boldsymbol{C}}\right],
\end{aligned} \tag{1.5}$$

where f_M is the volume fraction of matrix and f_f is the volume fraction of collagen fibers.

1.6.2 Multi-scale approaches

In order to include more structural features into the hyperelastic constitutive models a multi-scale approach was developed by [87, 148] to represent collagen

fibers in the soft tissue. For example in [87], the mechanical response of crimped collagen fibers was described by an equivalent tangent fiber modulus $E_f(\lambda_4, \lambda_6)$ where $\lambda_4 = (I_4)^{\frac{1}{2}}$ and $\lambda_6 = (I_6)^{\frac{1}{2}}$ are fiber stretches, accounting for collagen fiber geometrical crimp (micro-scale) and introducing a worm-like chain model molecular response at the (nano-scale). Thus the strain energy density of fibers in Eq. (1.2) is expressed as follows [90, 91, 8]:

$$\psi_{ani}(\boldsymbol{C}, \underline{e}_0^1, \underline{e}_0^2) = \psi_{ani}(I_4, I_6) = \int_1^{1+\frac{1}{2}[(\lambda_4-1)+(\lambda_6-1)]} \int_1^{1+(\xi-1)} E_f(\eta) d\eta d\xi. \quad (1.6)$$

1.7 Limits of the existing models and overview of the thesis

In most hyperelastic models, the contribution of elastin fibers is assumed as isotropic and combined with the matrix [61, 131, 19, 16, 90, 91, 8] although experiments have shown the anisotropic contribution of elastin fibers in the mechanical response of the tissue [90]. Furthermore, one can only compute the macroscopic stress and deformation through hyperelastic constitutive models in which the fibers are continuously embedded in their surrounding matrix and the fibers follow the macroscopic deformation (affine deformation). However, experimental observations reveal that by increasing the mechanical load fibers are capable to generate shear stresses to rotate faster than the matrix (non-affine deformation) [82]. This exponential strain energy density function [44] was recently extended to exclude the effect of collagen fibers under compression [85] and can reproduce the experimental results with accuracy but the material parameters do not have a direct relationship with microstructural features such as collagen fiber waviness, intramuscular cross-link, and presence of other fibers and molecules [90]. Furthermore, the development of multiscale models allow to include the undulation of collagen fibers and taking into account the anisotropy of collagen fibrils in different scales [99]. Recently, beyond developing the continuum models, discrete network models have also been implemented to describe microstructural details of the soft tissue [152, 92] to include truly microstructural constituents and physical phenomena to bridge with the tissue biology in the constitutive models.

As we discussed in this chapter, the mechanical properties of arteries come from the physical and mechanobiological mechanisms, which occur within the

microstructure, and these aspects are significantly altered in cardiovascular diseases [67]. Arterial tissue is a complex multiphase material containing active components such as cells and structural macromolecules. These components undergo a load-induced progressive morphological rearrangement such that tissue exhibits highly nonlinear anisotropic behavior with the ability to sustain large reversible strains. The significant role of the microstructure morphology and composition on arterial response motivated us to develop a detailed multiscale model of the arterial wall, which could provide new insights into the arterial structure-function relationships. To this aim, we propose a model in the framework of continuum micromechanics under large strains, taking into account universal patterns (representative volume element) of the hierarchical organization of arteries at different scales to relate microstructural mechanisms to their macroscopic mechanical consequences. This aim was reached by achieving the following steps:

- **Developing layer-specific representative volume element (RVE)**: The stacks of images from Krasny experiments [82] were used to reconstruct the RVEs for adventitia and media layers. Image analysis was performed on these images to determine the required physical quantities such as volume fractions and orientation of each constituent. However, the literature was also reviewed to obtain some other physical quantities to build up the three main layers of arterial structure; namely, adventitia, lamellae and interlamellar space. Within the adventitia, two scales were considered so as to account for both the fibril decrimping (through the progressive fibril reorientation at the lowest scale) and bundle realignment (at the macroscopic scale). Within the media, a stack of lamellae and interlamellar space was considered.

- **Multi-scale modeling of the hierarchical structure of artery**: The RVEs considered as a fiber-reinforced soft composite, where the hypoelastic constitutive laws were taken into account to model the constituents within the RVEs. Due to the large deformation, an extension of Eshelby's matrix-inclusion problem was used to compute analytical expressions for the strain rate and spin concentration tensors. These concentration tensors were used in a multi-scale approach to compute averaged strain rate and averaged spin tensors over the phases through the hierarchical structure of

the artery from the applied macroscopic strain rate. The computed averaged strain rate at each phase provides access to the microscopic stress, while the averaged spin tensor determines the load-induced phase rotation.

- **Integrating the homogenized models in a structural model of the artery**: In order to account for the interaction of these RVEs, we implemented the micromechanical framework in a finite element formulation. We considered an arterial segment with a simplified geometry of a hollow cylinder. The multi-scale constitutive model was considered in a home-made finite element code to account for adventitia, lamellae and interlamellar space across the thickness of the arterial wall.

2 | Theoretical framework: continuum micromechanics

Contents

Résumé

La plupart des matériaux rencontrés dans notre vie, allant des matériaux manufacturés aux matériaux naturels, peuvent être considérés comme homogènes à une échelle dite macroscopique, mais ont une microstructure hétérogène. Ils sont constitués de différents constituants présentant généralement une microstructure complexe, voir par exemple la microstructure de la couche la plus externe du tissu artériel présentée Fig. 2.1. Il est important de noter que la disposition des constituants composant la microstructure joue un rôle important dans la compréhension et la prédiction du comportement macroscopique des matériaux hétérogènes. A cet égard, la micromécanique des milieux continus est un cadre possible pour prendre en compte la morphologie de la microstructure afin de développer un modèle mathématique permettant de prédire le comportement global de tels matériaux [59, 132, 158, 159, 125]. Ce chapitre présente les outils théoriques de micromécanique des milieux continus, étendus au cadre des grandes transformations. L'approche est basée sur une loi de comportement hypoélastique, et sur le calcul de la vorticité de chaque phase qui induit une rotation progressive.

2.1 Introduction

Most of the materials encountered in our life, ranging from manufactured to natural materials, can be considered as homogeneous at a so-called macroscopic scale, but have a heterogeneous microstructure. They are built up by different constituents usually exhibiting a complex microstructure, see for instance the microstructure of the most outer layer of arterial tissue shown on Fig. 2.1.

It is important to notice that the arrangement of the constituents making up the microstructure play a significant role in understanding and controlling the macroscopic behavior of heterogeneous materials. In this respect, continuum micromechanics is a possible framework to take into account the microstructure morphology to develop a mathematical model that predicts the overall behavior of such materials [59, 132, 158, 159, 125].

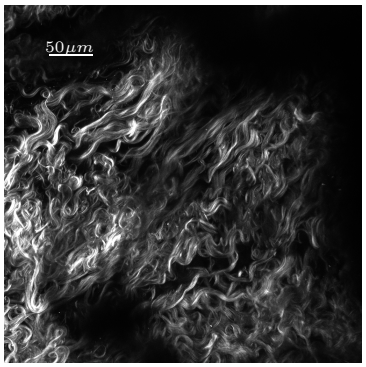

Figure 2.1: Microstructure of the most outer layer (called adventitia) of a rabbit carotid artery, imaged under a multiphoton microscope [82].

2.2 Representative volume element and assumptions of scale separation

In continuum micromechanics, the first step consists in identifying the patterns of the material's microstructure that govern the mechanical response of the material. The complexity of many material's microstructures prevents from accounting for each and every detail: as a remedy, a statistical approach is preferred and sub-volumes with known physical quantities are identified and called material phases. These phases are characterized by their shape, volume fraction, orientation, and homogeneous mechanical properties. The arrangement of the different phases makes up a representative volume element (RVE). For instance, Fig. 2.2 shows a possible representative volume element representing the microstructure of the arterial adventitial layer shown on Fig. 2.1.

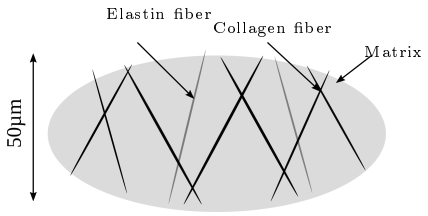

Figure 2.2: Representative volume element of the arterial adventitia layer.

Furthermore, the RVE must satisfy the condition of scale separation, reading

as:

$$d \ll l \ll \mathcal{L} \tag{2.1}$$

- The characteristic length of the heterogeneities (d) must be small enough as compared to the characteristic length of the RVE (l), that is $d \ll l$. This ensures that the homogenized response remains independent of the precise geometry of the RVE, i.e. the RVE is really representative.

- The characteristic length of the RVE must also be small enough in comparison to the characteristic length of the structure ($\mathcal{L}$) and of the loading to which the structure is subjected that is $l \ll \mathcal{L}$, such that the macroscopic fields remain continuous.

Once the different RVEs have been defined under the requirement of scale separation, the geometrical and physical characteristics of their phases must be identified. These characteristics include the phase geometrical shape (and possibly its orientation), as well as its volume fraction and its constitutive relation, these characteristics being in most cases of statistical nature.

2.3 Momentum balance and kinematic compatibility

2.3.1 Hashin boundary condition in large strain continuum micromechanics - strain rate average rule

After the description of the RVE morphology, adequate boundary conditions need to be defined on the RVE. Since the detailed boundary conditions existing on the RVE are not known, and the average conditions which exist (and will be later detailed, see Eqs. (2.4) and (2.8)) lead to an ill-posed problem, homogeneous boundary conditions on the RVE have to be employed [58, 53]: a homogeneous strain rate is assigned on the current boundary $\partial\Omega$ of the RVE (with volume Ω), in terms of a velocity field $\underline{\mathrm{v}}(\underline{\mathrm{x}})$ as follows:

$$\underline{\mathrm{v}}(\underline{\mathrm{x}}) = \boldsymbol{D} \cdot \underline{\mathrm{x}} \qquad \forall \underline{\mathrm{x}} \in \partial\Omega, \tag{2.2}$$

whereby $\boldsymbol{D}$ is the macroscopic strain rate tensor, and $\underline{\mathrm{x}}$ is the microscopic position vector in the current configuration. In addition, compatibility inside the RVE

yields the microscopic strain rate field $\boldsymbol{d}(\underline{x})$ as:

$$\boldsymbol{d}(\underline{x}) = \frac{1}{2}\left(\mathbf{grad}\ \underline{v}(\underline{x}) + [\mathbf{grad}\ \underline{v}(\underline{x})]^T\right) \qquad \forall \underline{x} \in \Omega, \tag{2.3}$$

Thus, the kinematically compatible microscopic strain rates $\boldsymbol{d}(\underline{x})$ inside the RVE, subjected to the homogeneous strain rate $\boldsymbol{D}$, fulfill the Hashin strain rate average rule:

$$\begin{aligned} \boldsymbol{D} &= \frac{1}{|\Omega|}\int_{\Omega} \boldsymbol{d}(\underline{x}) dV = \langle \boldsymbol{d} \rangle, \\ &= \frac{1}{2|\Omega|}\int_{\partial\Omega} \Big[\underline{v}(\underline{x}) \otimes \underline{n}(\underline{x}) + \underline{v}(\underline{x}) \otimes \underline{n}(\underline{x})\Big] dS, \end{aligned} \tag{2.4}$$

whereby we made use of the Green-Ostrogradski theorem to evaluate the rate of deformation at the boundary, $\langle \cdot \rangle$ denotes the spatial average operator, $\underline{n}(\underline{x})$ is the unit normal outward-pointing vector at point $\underline{x}$ of the boundary of RVE, and $\otimes$ is the dyadic product.

2.3.2 Momentum balance and stress average rule - Hill's lemma

The rate of deformation existing on the boundary of the RVE results in the existence of traction forces $\underline{t}(\underline{x})$ on the boundary of RVE which must be in equilibrium, such that:

$$\int_{\partial\Omega} \underline{t}(\underline{x}) dS = \int_{\partial\Omega} \boldsymbol{\sigma}(\underline{x}) \cdot \underline{n}(\underline{x}) dS = 0 \tag{2.5}$$

whereby use of Cauchy's theorem, $\underline{t}(\underline{x}) = \boldsymbol{\sigma}(\underline{x}) \cdot \underline{n}(\underline{x})$, has been made. Once again, applying the Green-Ostrogradski theorem to Eq. (2.5) leads to the expected equilibrium equation at each point of the RVE, reading as:

$$\underline{\mathrm{div}}\ \boldsymbol{\sigma}(\underline{x}) = 0 \qquad \forall \underline{x} \in \Omega. \tag{2.6}$$

Then, one can compute the external power of traction force $\mathcal{P}^{ext}$ on the RVE, by applying Cauchy's theorem and accounting for the Hashin's boundary condition, leading to:

$$\mathcal{P}^{ext} = \int_{\partial\Omega} \underline{t}(\underline{x}) \cdot \underline{v}(\underline{x}) dS = \int_{\partial\Omega} [\boldsymbol{\sigma}(\underline{x}) \cdot \underline{n}(\underline{x})] \cdot [\boldsymbol{D} \cdot \underline{x}] dS = \left(\int_{\Omega} \boldsymbol{\sigma}(\underline{x}) dV\right) : \boldsymbol{D}. \tag{2.7}$$

The position-independent volume integral of microscopic Cauchy stresses in the external power induces the existence of a macroscopic Cauchy stress defined by:

$$\boldsymbol{\Sigma} = \frac{1}{|\Omega|}\int_{\Omega} \boldsymbol{\sigma}(\underline{\mathrm{x}})dV = \langle \boldsymbol{\sigma} \rangle, \tag{2.8}$$

in the form of a stress average rule. The external power on the RVE is therefore a function of the macroscopic stress and strain rate,

$$\mathcal{P}^{ext} = \boldsymbol{\Sigma} : \boldsymbol{D}, \tag{2.9}$$

Furthermore, substituting the stress average rule (2.8) into the principle of virtual power [47] leads to:

$$\mathcal{P}^{ext} = -\mathcal{P}^{int} = \frac{1}{|\Omega|}\int_{\Omega} \boldsymbol{\sigma}(\underline{\mathrm{x}}) : \boldsymbol{d}(\underline{\mathrm{x}})dV = \langle \boldsymbol{\sigma} : \boldsymbol{d} \rangle, \tag{2.10}$$

where $\mathcal{P}^{int}$ is the power of internal forces. Equations (2.9) and (2.10) reveal the Hill's lemma: the average power generated by the microscopic stresses on the microscopic strain rates is equal to the power generated by the macroscopic stress on the macroscopic strain rate reading as,

$$\boldsymbol{\Sigma} : \boldsymbol{D} = \langle \boldsymbol{\sigma} \rangle : \langle \boldsymbol{d} \rangle = \frac{1}{|\Omega|}\int_{\Omega} \boldsymbol{\sigma}(\underline{\mathrm{x}}) : \boldsymbol{d}(\underline{\mathrm{x}})dV = \langle \boldsymbol{\sigma} : \boldsymbol{d} \rangle. \tag{2.11}$$

2.4 Thermodynamic foundation of the microscopic hypo-elastic constitutive relation

The constitutive relations have to satisfy both first and second principles of thermodynamics, which can be combined into the Clausius-Duhem inequality [118], expressing the system's dissipation $\mathcal{D}$, as:

$$\mathcal{D} = \boldsymbol{\sigma} : \boldsymbol{d} - \rho\left(\frac{D\psi}{Dt} + s\frac{DT}{Dt}\right) - \frac{\underline{q}}{T} \cdot \underline{\mathrm{grad}}\, T \geq 0, \tag{2.12}$$

whereby $\boldsymbol{\sigma}$ and $\boldsymbol{d}$ are respectively the Cauchy stress and strain rate tensors, ρ is the mass density, T is the absolute temperature, and s is the (microscopic) entropy per unit mass. Furthermore, the (microscopic) Helmholtz free energy per unit mass, ψ, is chosen here as the thermodynamic potential, and $\underline{q}$ is the outward heat flux vector at the boundary of the structure. The operator $\frac{D(\cdot)}{Dt}$ is the material derivative of quantity $(\cdot)$. For an elastic (i.e. reversible) transformation, the dissipation remains equal to zero, $\mathcal{D} = 0$. The dissipation (2.12) is usually

split into two parts, the intrinsic dissipation $\mathcal{D}_1$, and the thermal dissipation $\mathcal{D}_2$, defined as:

$$\begin{aligned} \mathcal{D}_1 &= \boldsymbol{\sigma} : \boldsymbol{d} - \rho \left(\frac{D\psi}{Dt} + s \frac{DT}{Dt} \right), \\ \mathcal{D}_2 &= -\frac{\underline{q}}{T} \cdot \underline{\text{grad}}\, T. \end{aligned} \tag{2.13}$$

It is usually assumed that each dissipation should be positive, and consequently, for a reversible transformation, one has $\mathcal{D}_1 = 0$. As proposed by Rajagopal [108, 109], we choose to work with the Gibbs thermodynamic potential $\mathcal{G}$ instead of the Helmholtz free energy ψ [96]. The relation between the two potentials results from a partial Legendre transformation on the variable $\boldsymbol{\sigma}$, as defined by:

$$\psi(\boldsymbol{d}, T) = \frac{\partial \mathcal{G}(\boldsymbol{\sigma}, T)}{\partial \boldsymbol{\sigma}} : \boldsymbol{\sigma} - \mathcal{G}(\boldsymbol{\sigma}, T). \tag{2.14}$$

As a consequence, the intrinsic dissipation reads as:

$$\mathcal{D}_1 = \boldsymbol{\sigma} : \boldsymbol{d} - \boldsymbol{\sigma} : \left(\rho \frac{\partial^2 \mathcal{G}(\boldsymbol{\sigma}, T)}{\partial \boldsymbol{\sigma} \partial \boldsymbol{\sigma}} \right) : \frac{D\boldsymbol{\sigma}}{Dt} - \rho \frac{D\mathcal{G}(\boldsymbol{\sigma}, T)}{DT} \frac{DT}{Dt} + \rho s \frac{DT}{Dt} = 0. \tag{2.15}$$

This latter expression of the intrinsic dissipation shows that temperature T and the Cauchy stress $\boldsymbol{\sigma}$ are natural arguments of the Gibbs thermodynamic potential. As a consequence, one gets the following state laws:

$$\begin{aligned} s &= -\frac{\partial \mathcal{G}(\boldsymbol{\sigma}, T)}{\partial T}, \\ \boldsymbol{d} &= \rho \frac{\partial^2 \mathcal{G}(\boldsymbol{\sigma}, T)}{\partial \boldsymbol{\sigma} \partial \boldsymbol{\sigma}} : \frac{D\boldsymbol{\sigma}}{Dt}. \end{aligned} \tag{2.16}$$

To ensure the objectivity of the second state law (i.e. the strain rate should not depend on the motion of the observer), one adds a gyroscopic term [96, 109], defined as:

$$\boldsymbol{\sigma} : \rho \frac{\partial^2 \mathcal{G}(\boldsymbol{\sigma}, T)}{\partial \boldsymbol{\sigma} \partial \boldsymbol{\sigma}} : (-\boldsymbol{\sigma} \cdot \boldsymbol{\Omega} + \boldsymbol{\sigma} \cdot \boldsymbol{\Omega}) = 0, \tag{2.17}$$

where $\boldsymbol{\Omega}$ is the spin skew-symmetric tensor ($\boldsymbol{\Omega}^{-1} = \boldsymbol{\Omega}^T$ and $\text{tr}(\boldsymbol{\Omega}) = 0$). This yields a thermodynamically reversible and objective hypo-elastic constitutive law in the form of:

$$\boldsymbol{d} = \rho \frac{\partial^2 \mathcal{G}(\boldsymbol{\sigma}, T)}{\partial \boldsymbol{\sigma} \partial \boldsymbol{\sigma}} : \left(\frac{D\boldsymbol{\sigma}}{Dt} + \boldsymbol{\Omega} \cdot \boldsymbol{\sigma} - \boldsymbol{\sigma} \cdot \boldsymbol{\Omega} \right). \tag{2.18}$$

Choosing $\boldsymbol{\Omega}$ as the skew-symmetric part of the microscopic velocity gradient, i.e.

$$\boldsymbol{\Omega} = \boldsymbol{\omega} = \frac{1}{2}\left(\mathbf{grad}\ \underline{\mathrm{v}}(\underline{\mathrm{x}}) - [\mathbf{grad}\ \underline{\mathrm{v}}(\underline{\mathrm{x}})]^T\right), \tag{2.19}$$

where **grad** is the Eulerian gradient and ^{T} the transpose operator. Then, a Gibbs potential in the form of $\mathcal{G} = \boldsymbol{\sigma} : \mathbb{C}^{-1} : \boldsymbol{\sigma}$, gives the microscopic constitutive law in a hypo-elastic formulation as follows:

$$\boldsymbol{\sigma}^{\nabla}(\underline{\mathrm{x}}) = \mathbb{C}(\underline{\mathrm{x}}) : \boldsymbol{d}(\underline{\mathrm{x}}), \tag{2.20}$$

where $\boldsymbol{\sigma}^{\nabla}(\underline{\mathrm{x}})$ is the (microscopic) stress rate in its objective form, $\mathbb{C}(\underline{\mathrm{x}})$ is the hypoelastic stiffness tensor, and $\boldsymbol{d}(\underline{\mathrm{x}})$ is the strain rate. The choice of $\boldsymbol{\Omega} = \boldsymbol{\omega}$, yields the objective stress rate as the Jaumann one, reading as:

$$\boldsymbol{\sigma}^{\nabla}(\underline{\mathrm{x}}) = \dot{\boldsymbol{\sigma}}(\underline{\mathrm{x}}) + \boldsymbol{\sigma}(\underline{\mathrm{x}}) \cdot \boldsymbol{\omega}(\underline{\mathrm{x}}) - \boldsymbol{\omega}(\underline{\mathrm{x}}) \cdot \boldsymbol{\sigma}(\underline{\mathrm{x}}), \tag{2.21}$$

where $\dot{\boldsymbol{\sigma}}(\underline{\mathrm{x}}) = \frac{D\boldsymbol{\sigma}(\underline{\mathrm{x}})}{Dt}$ is the time derivative of the microscopic Cauchy stress.

As a summary, the homogenization problem is governed by the following set of equations: local equilibrium (2.6), strain rate compatibility (2.3), local constitutive behavior (2.20), and strain and stress rate average rules (2.4) and (2.8). All these equations are linear; as a consequence, there exists a linear relation between the microscopic strain rate and spin, and the prescribed boundary condition, reading as:

$$\begin{aligned} \boldsymbol{d}(\underline{\mathrm{x}}) &= \mathbb{A}(\underline{\mathrm{x}}) : \boldsymbol{D}(\underline{\mathrm{x}}) \\ \boldsymbol{\omega}(\underline{\mathrm{x}}) &= \mathbb{R}(\underline{\mathrm{x}}) : \boldsymbol{D}(\underline{\mathrm{x}}), \end{aligned} \tag{2.22}$$

where $\mathbb{A}(\underline{\mathrm{x}})$ is the fourth-order strain rate concentration tensor and $\mathbb{R}(\underline{\mathrm{x}})$ is the fourth-order spin concentration tensor. The next section is devoted to estimating expressions for these concentration tensors.

2.5 Mori-Tanaka estimation of strain rate and spin concentration tensors from auxiliary Eshelby problems

Different approaches have been proposed to estimate the concentration relations. One set of methods relies on the use of the variational principles, which allow to bound the effective properties [53, 59]. Depending on the assumptions taken on

the morphology of the RVE, the bounds are more or less restrictive. The other approach consists in the use of a mean field approach. The framework in which our model is developed is based on the latter approach, which is detailed in the following sections.

2.5.1 Eshelby problem as a first estimate of the concentration tensors

In the framework of homogenization, concentration tensors allow to determine the microscopic fields in the phases as functions of the applied macroscopic fields. As a first simple case, an Eshelby matrix-inclusion type problem [31] is used to estimate the concentration tensors. However, we consider not only the strain rate but also the rotation of the inclusion or spin, which provides the basis for a large strain micromechanics theory.

The Eshelby inclusion problem considers an infinite material with stiffness $\mathbb{C}_0$, in which a small ellipsoidal volume Ω_I is subjected to a uniform field of eigenstrain rate $\boldsymbol{\eta}$, while the rest of the material is free from any eigenstrain rate and no loading is applied on the material, see Fig. 2.3(A). Due to the linearity of the problem and to the shape of the inclusion, Eshelby showed that this eigenstrain rate induces a uniform velocity gradient field in the inclusion as:

$$\mathbf{grad}\underline{\mathrm{v}}(\underline{\mathrm{x}}) = \mathbb{L}^{Esh} : \boldsymbol{\eta} \qquad \forall \underline{\mathrm{x}} \in \Omega_I, \tag{2.23}$$

where $\mathbb{L}^{Esh}$ is the Eshelby strain rate-to-velocity gradient tensor, depending on the stiffness of the matrix $\mathbb{C}_0$, and on the shape and the orientation of the ellipsoidal inclusion.

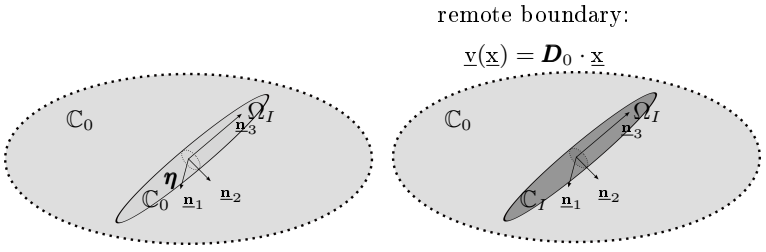

(A) Inhomogeneity problem (B) Eshelby inclusion problem

Figure 2.3: Inhomogeneity and Eshelby inclusion problems.

The orientation of the ellipsoidal inclusion is defined by an orthonormal basis

$\underline{n}_i$ ($i = 1, 2, 3$), which coincides with the principal axes of the ellipsoidal inclusion. The aspect ratios representing the shape of the inclusion are $\omega_1 = \frac{a_3}{a_1}$, $\omega_2 = \frac{a_3}{a_2}$, and $\omega_3 = \frac{a_1}{a_2}$, where $2a_i$ ($i = 1, 2, 3$) are the lengths of the principal axes of the ellipsoidal inclusion, such that: $a_1 \leq a_2 \leq a_3$.

In the present work, we focus on infinitely long cylindrical inclusions (see Fig. 2.4), i.e. $a_3 \to \infty$, and $a_2 = a_1$. In this case, the non zero components of $\mathbb{L}^{Esh}$ are expressed, in the $\underline{n}_i$ basis, in terms of the Poisson's ratio of the isotropic matrix ν_0 [9, 96] as:

$$\begin{aligned}
L^{Esh}_{1111} &= L^{Esh}_{2222} = \frac{4\nu_0 - 5}{8(\nu_0 - 1)} \\
L^{Esh}_{1122} &= L^{Esh}_{2211} = -\frac{4\nu_0 - 5}{8(\nu_0 - 1)} \\
L^{Esh}_{1212} &= L^{Esh}_{1221} = L^{Esh}_{2112} = L^{Esh}_{2112} = \frac{4\nu_0 - 3}{8(\nu_0 - 1)} \\
L^{Esh}_{1133} &= L^{Esh}_{2233} = \frac{-\nu_0}{2(\nu_0 - 1)} \\
L^{Esh}_{3113} &= L^{Esh}_{3223} = L^{Esh}_{3131} = L^{Esh}_{3232} = \frac{1}{2}.
\end{aligned} \tag{2.24}$$

We will also consider lamellar structures, and introduce inclusions in the form of oblate spheroids i.e. $a_3 \to \infty$ and $a_2 \to \infty$. In this case, the non zero $\mathbb{L}^{Esh}$ components for an infinitely thin plate embedded in an isotropic matrix with Poisson's ratio ν_0, read, in the $\underline{n}_i$ basis, as:

$$\begin{aligned}
L^{Esh}_{1111} &= 1 \\
L^{Esh}_{2112} &= L^{Esh}_{2211} = \frac{1 - 2\nu_0}{2(1 - \nu_0)} \\
L^{Esh}_{3113} &= L^{Esh}_{3311} = 1 \\
L^{Esh}_{1212} &= -\frac{1 - 2\nu_0}{2(1 - \nu_0)} \\
L^{Esh}_{1313} &= \frac{\nu_0}{1 - \nu_0}.
\end{aligned} \tag{2.25}$$

More details on derivations of the Eshelby strain rate-to-velocity gradient tensor are provided in the Appendix A.

From the uniform velocity gradient in the inclusion expressed by Eq. (2.23), one can compute the uniform strain rate tensor and the spin tensor within the inclusion respectively as:

$$\boldsymbol{d}(\underline{x}) = \frac{1}{2}\left(\mathbf{grad}\underline{v}(\underline{x}) + [\mathbf{grad}\underline{v}(\underline{x})]^T\right) \qquad \forall \underline{x} \in \Omega_I, \tag{2.26}$$

$$\boldsymbol{\omega}(\underline{\mathrm{x}}) = \frac{1}{2}\left(\mathbf{grad}\underline{\mathrm{v}}(\underline{\mathrm{x}}) - [\mathbf{grad}\underline{\mathrm{v}}(\underline{\mathrm{x}})]^T\right) \qquad \forall \underline{\mathrm{x}} \in \Omega_I, \tag{2.27}$$

these are linearly related to the eigenstrain rate $\boldsymbol{\eta}$ in the domain Ω_I, through the Eshelby strain rate-to-velocity gradient tensor,

$$\boldsymbol{d}(\underline{\mathrm{x}}) = \frac{1}{2}\left(\mathbb{L}^{Esh} + \left[\mathbb{L}^{Esh}\right]^T\right) : \boldsymbol{\eta} = \mathbb{S}^{Esh} : \boldsymbol{\eta} \qquad \forall \underline{\mathrm{x}} \in \Omega_I, \tag{2.28}$$

$$\boldsymbol{\omega}(\underline{\mathrm{x}}) = \frac{1}{2}\left(\mathbb{L}^{Esh} - \left[\mathbb{L}^{Esh}\right]^T\right) : \boldsymbol{\eta} = \mathbb{R}^{Esh} : \boldsymbol{\eta} \qquad \forall \underline{\mathrm{x}} \in \Omega_I, \tag{2.29}$$

where $\mathbb{S}^{Esh} = \frac{1}{2}\left(\mathbb{L}^{Esh} + \left[\mathbb{L}^{Esh}\right]^T\right)$ and $\mathbb{R}^{Esh} = \frac{1}{2}\left(\mathbb{L}^{Esh} - \left[\mathbb{L}^{Esh}\right]^T\right)$ are respectively fourth-order Eshelby concentration tensor for strain rate and spin in the Eshelby inhomogeneity problem, see Fig. 2.3(A).

This first Eshelby problem can then be extended to the following problem: an ellipsoidal inclusion, with stiffness $\mathbb{C}_I$ and occupying the volume Ω_I, is surrounded by an infinite matrix with stiffness $\mathbb{C}_0$; the material is subjected to a macroscopic strain rate $\boldsymbol{D}_0$, at its remote boundary, see Fig. 2.3(B).

The superposition principle is used and this second problem is decomposed as the sum of two problems: first a homogeneous infinite material, with stiffness $\mathbb{C}_0$, is subjected to the boundary conditions $\underline{\mathrm{v}}(\underline{\mathrm{x}}) = \boldsymbol{D}_0 \cdot \underline{\mathrm{x}}$; the second subproblem is the previously described inhomogeneity Eshelby problem, whereby the eigenstrain field $\boldsymbol{\eta}$ is expressed in terms of the stiffness tensors as:

$$\boldsymbol{\eta} = -\mathbb{C}_0^{-1} : [\mathbb{I} + (\mathbb{C}_I - \mathbb{C}_0) : \mathbb{P}_I]^{-1} : (\mathbb{C}_I - \mathbb{C}_0) : \boldsymbol{D}_0, \tag{2.30}$$

where $\mathbb{P}_I = \mathbb{S}^{Esh} : {\mathbb{C}_0}^{-1}$ is the Hill tensor, and $\mathbb{I}$ is the fourth-order identity tensor, with components $I_{ijkl} = \frac{1}{2}(\delta_{ik}\delta_{jl} + \delta_{il}\delta_{jk})$, δ_{ij} being the Kronecker delta, i.e. $\delta_{ij} = 1$, if $i = j$, and zero otherwise.

Substitution of Eq. (2.30) into Eqs. (2.28) and (2.29) gives the linear relation between the prescribed strain rate at the boundary of RVE and the uniform strain rate in the inclusion, reading as:

$$\boldsymbol{d}_I = [\mathbb{I} + (\mathbb{C}_I - \mathbb{C}_0) : \mathbb{P}_I]^{-1} : \boldsymbol{D}_0 = \mathbb{A}^{\infty} : \boldsymbol{D}_0, \tag{2.31}$$

$$\boldsymbol{\omega}_I = -\mathbb{R}^{Esh} : \mathbb{C}_0^{-1} : [\mathbb{I} + (\mathbb{C}_I - \mathbb{C}_0) : \mathbb{P}_I]^{-1} : (\mathbb{C}_I - \mathbb{C}_0) : \boldsymbol{D}_0 = \mathbb{R}^{\infty} : \boldsymbol{D}_0, \tag{2.32}$$

where $\mathbb{A}^{\infty}$ and $\mathbb{R}^{\infty}$ are respectively the expressions of the concentration tensors for strain rate and spin in the Eshelby problem. While the strain rate and spin

are uniform in the inclusion, the strain rate and spin are not uniform outside the inclusion. The strain rate becomes equal to the prescribed strain rate far from the inclusion but close to the inclusion, strong variations in strain rate and spin are encountered.

2.5.2 Mori-Tanaka estimate for fiber-reinforced composites

In this section, we consider heterogeneous materials, whose microstructure can be described by N inclusion phases embedded in a surrounding matrix M, and subjected to a uniform strain rate $\boldsymbol{D}$ at the boundary of the RVE (see Fig. 2.4). In this case, the strain rate and spin fields are not anymore uniform in the inclusions due to their mutual interactions. As a remedy, a mean field approach is used, and the previously described Eshelby problem is taken as an auxiliary problem to evaluate the mean value of the strain rate and spin fields within the inclusion. In this auxiliary problem, the auxiliary matrix has the same mechanical properties as the matrix of the considered material, and the inhomogeneity has the same shape and mechanical properties as the inclusion for which the mechanical response needs to be determined. Equations (2.31) and (2.32) respectively provide the mean strain rate and mean spin in the inclusion. This result is substituted into the strain rate average rule Eq. (2.4) and leads to:

$$\boldsymbol{D} = \sum_{r=1}^{N} f_r \boldsymbol{d}_r + f_M \boldsymbol{d}_M, \tag{2.33}$$

with f_r and f_M respectively as the volume fractions of inclusion phase r and of matrix. This reveals a relation between the prescribed strain rate $\boldsymbol{D}$ at the

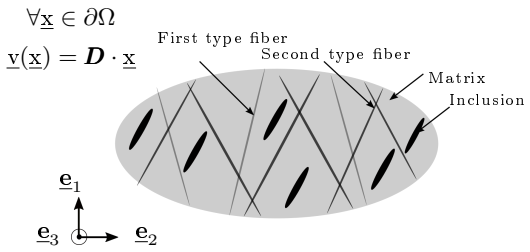

Figure 2.4: Representative Volume Element of heterogeneous materials subjected to homogeneous strain rate as the velocity vector at the boundary.

boundary of the RVE (Fig. 2.4) and the prescribed strain rate at the remote boundary of the auxiliary Eshelby problem, $\boldsymbol{D}_0$ (Fig. 2.3): the auxiliary applied

strain rate is equal to the mean strain rate in the matrix phase of the considered problem, and its expression reads as:

$$\boldsymbol{D}_0 = \boldsymbol{d}_M = \left\{ \sum_{r=1}^{N} f_r \left[\mathbb{I} + (\mathbb{C}_r - \mathbb{C}_0) : \mathbb{P}_r \right]^{-1} + f_M \mathbb{I} \right\}^{-1} : \boldsymbol{D}. \tag{2.34}$$

As a consequence, the mean strain rate and spin in each inclusion phase are expressed as follows:

$$\begin{aligned} \boldsymbol{d}_r &= \left[\mathbb{I} + (\mathbb{C}_r - \mathbb{C}_0) : \mathbb{P}_r \right]^{-1} : \left\{ \sum_{r=1}^{N} f_r \left[\mathbb{I} + (\mathbb{C}_r - \mathbb{C}_0) : \mathbb{P}_r \right]^{-1} + f_M \mathbb{I} \right\}^{-1} : \boldsymbol{D} \\ &= \mathbb{A}_r : \boldsymbol{D}, \end{aligned} \tag{2.35}$$

$$\begin{aligned} \boldsymbol{\omega}_r = \mathbb{R}^{\infty} : {\mathbb{C}_0}^{-1} : \left[\mathbb{I} + (\mathbb{C}_r - \mathbb{C}_0) : \mathbb{P}_r \right]^{-1} : (\mathbb{C}_r - \mathbb{C}_0) \\ : \left\{ \sum_{r=1}^{N} f_r \left[\mathbb{I} + (\mathbb{C}_r - \mathbb{C}_0) : \mathbb{P}_r \right]^{-1} + f_M \mathbb{I} \right\}^{-1} : \boldsymbol{D} = \mathbb{R}_r : \boldsymbol{D}. \end{aligned} \tag{2.36}$$

From Eqs. (2.35) and (2.36), the fourth-order strain rate and spin concentration tensors, $\mathbb{A}_r$, $\mathbb{A}_M$, and $\mathbb{R}_r$ respectively, can be identified as:

$$\mathbb{A}_r = \mathbb{A}_r^{\infty} : \left\{ \sum_{i=1}^{N} f_i \mathbb{A}_i^{\infty} + f_M \mathbb{I} \right\}^{-1} \qquad \forall r \in \{1, 2, 3, ..., N\}, \tag{2.37}$$

$$\mathbb{A}_M = \left\{ \sum_{i=1}^{N} f_i \mathbb{A}_i^{\infty} + f_M \mathbb{I} \right\}^{-1}, \tag{2.38}$$

$$\mathbb{R}_r = \mathbb{R}_r^{\infty} : \left\{ \sum_{i=1}^{N} f_i \mathbb{A}_i^{\infty} + f_M \mathbb{I} \right\}^{-1} \qquad \forall r \in \{1, 2, 3, ..., N\}, \tag{2.39}$$

where $\mathbb{A}_r^{\infty}$ and $\mathbb{R}_r^{\infty}$ are respectively the strain rate and spin concentration tensors of the auxiliary Eshelby problem, defined by Eqs. (2.31) and (2.32). This homogenization scheme is called the Mori-Tanaka scheme [94, 5].

2.6 Algorithmic treatment of fiber kinematics

2.6.1 Motivation for time discretization

The homogenization scheme under large deformation is highly nonlinear due to the conformational changes of the microstructure. Therefore, an incremental

approach is implemented to solve the governing equations: the load history is divided into a finite number of steps and an infinitesimal part of the load is applied at each increment. Thus, the deformation and evolution of the microstructure can be approximated to be linear at each increment. Then one can solve the linearized equations and keep track of all the increments to get the solution of the nonlinear problem. We use an updated Lagrangian description [3], which requires the knowledge of the updated configuration at each increment: the current configuration is used as a reference configuration to compute the fields at the next increment.

Due to the complex dependence of the concentration tensors on the inclusion orientations, a forward Euler scheme is employed for time discretization, i.e. for a quantity a, one has:

$$\dot{a}^t = \frac{a^{t+dt} - a^t}{dt} \tag{2.40}$$

where $\dot{a}$ is the time derivative of the quantity a, with a^t the value of the quantity at time t and a^{t+dt} the value of the quantity after a small time increment dt. At the initial time, the orientation $\theta_r^{t=0}$ and $\phi_r^{t=0}$ of the inclusions $r = \{1, 2, 3, ..., N\}$ are known, as well as the microscopic stress $\boldsymbol{\sigma}_r^{t=0}$ and deformation gradient $\boldsymbol{f}_r^{t=0}$ in all phases, which are respectively equal to zero and to identity. We now discretize each subset of equations, assuming that the state at time t is known, and we try to determine the mechanical state at time $t + dt$.

2.6.2 Concentration equations

The Eqs. (2.35) and (2.36) are evaluated at time instant t, and allow to evaluate the local strain rate $\boldsymbol{d}_r^t$ and local spin tensor $\boldsymbol{\omega}_r^t$ as functions of the strain rate concentration tensor $\mathbb{A}_r^t$ and spin concentration tensor $\mathbb{R}_r^t$ at time t, (i.e. defined as $\mathbb{A}_r^t = \mathbb{A}(\theta_r^t, \phi_r^t)$ and $\mathbb{R}_r^t = \mathbb{R}(\theta_r^t, \phi_r^t)$), and of the applied strain rate at time t, $\boldsymbol{D}^t$, as:

$$\begin{aligned} \boldsymbol{d}_r^t &= \mathbb{A}_r^t : \boldsymbol{D}^t \quad \forall r \in \{1, 2, 3, ..., N, M\}, \\ \boldsymbol{\omega}_r^t &= \mathbb{R}_r^t : \boldsymbol{D}^t \quad \forall r \in \{1, 2, 3, ..., N\}. \end{aligned} \tag{2.41}$$

2.6.3 Local constitutive relations

From equations (2.20) and (2.21), we obtain the local constitutive relation of each phase r in terms of the material derivative of the microscopic Cauchy stress at

time t as follows:

$$\left(\frac{D\boldsymbol{\sigma}_r}{Dt}\right)^t = \dot{\boldsymbol{\sigma}}_r^t = \mathbb{C}_r^t : \boldsymbol{d}_r^t - \boldsymbol{\sigma}_r^t \cdot \boldsymbol{\omega}_r^t + \boldsymbol{\omega}_r^t \cdot \boldsymbol{\sigma}_r^t, \tag{2.42}$$

i.e. for each phase:

$$\begin{aligned} \dot{\boldsymbol{\sigma}}_r^t &= \mathbb{C}_r^t : \boldsymbol{d}_r^t - \boldsymbol{\sigma}_r^t \cdot \boldsymbol{\omega}_r^t + \boldsymbol{\omega}_r^t \cdot \boldsymbol{\sigma}_r^t, \quad \forall r \in \{1, 2, 3, ..., N\}. \\ \dot{\boldsymbol{\sigma}}_M^t &= \mathbb{C}_M^t : \boldsymbol{d}_M^t. \end{aligned} \tag{2.43}$$

Accounting for Eq. (2.41), one can compute the local constitutive equation in terms of the prescribed strain rate at the boundary, as follows:

$$\begin{aligned} \dot{\boldsymbol{\sigma}}_r^t &= \mathbb{C}_r^t : \mathbb{A}_r^t : \boldsymbol{D}^t - \boldsymbol{\sigma}_r^t \cdot (\mathbb{R}_r^t : \boldsymbol{D}^t) + (\mathbb{R}_r^t : \boldsymbol{D}^t) \cdot \boldsymbol{\sigma}_r^t \\ \dot{\boldsymbol{\sigma}}_M^t &= \mathbb{C}_M^t : \mathbb{A}_M^t : \boldsymbol{D}^t. \end{aligned} \tag{2.44}$$

It is interesting to write (2.44) using the index notation, which gives,

$$\begin{aligned} \dot{\sigma}_{ij}^r &= \left[C_{ijkl}^r A_{lkmn}^r - \sigma_{ik}^r R_{kjmn}^r + R_{ikmn}^r \sigma_{kj}^r\right] D_{nm} = C_{ijmn}^{r^{eq}} D_{nm}, \\ \dot{\sigma}_{ij}^M &= \left[C_{ijkl}^M A_{lkmn}^M\right] D_{nm} = C_{ijmn}^{M^{eq}} D_{nm}, \end{aligned} \tag{2.45}$$

whereby all the variables are evaluated at time t and fourth-order equivalent "stiffness" tensors $\mathbb{C}_r^{eq}$ for phase inclusion r and $\mathbb{C}_M^{eq}$ for matrix phase are defined, using the index notation, as:

$$\begin{aligned} C_{ijmn}^{r^{eq}} &= C_{ijkl}^r A_{lkmn}^r - \sigma_{ik}^r R_{kjmn}^r + R_{ikmn}^r \sigma_{kj}^r, \\ C_{ijmn}^{M^{eq}} &= C_{ijkl}^M A_{lkmn}^M. \end{aligned} \tag{2.46}$$

for the current stress state at time t. Finally, since the material derivative is equivalent to a partial derivative with respect to time in the Lagrangian formulation (fixed reference frame) $\frac{D(\cdot)}{Dt} = \frac{\partial(\cdot)}{\partial t}$, using a forward Euler scheme for the time derivative of the Cauchy stress $\dot{\boldsymbol{\sigma}}^t = \frac{\boldsymbol{\sigma}^{t+dt} - \boldsymbol{\sigma}^t}{dt}$, one can compute the updated microscopic Cauchy stress in the form of,

$$\begin{aligned} \boldsymbol{\sigma}_r^{t+dt} &= \boldsymbol{\sigma}_r^t + \mathbb{C}_r^{eq^t} : \boldsymbol{D}^t dt, \quad \forall r \in \{1, 2, 3, ..., N\}. \\ \boldsymbol{\sigma}_M^{t+dt} &= \boldsymbol{\sigma}_M^t + \mathbb{C}_M^{eq^t} : \boldsymbol{D}^t dt. \end{aligned} \tag{2.47}$$

2.6.4 Fiber reorientation and stress average rule

Since the inclusions are not necessarily aligned with the global base frame, the previously introduced base frame $\underline{n}_i$ is replaced by a spherical base frame ($\underline{e}_r$, $\underline{e}_\theta$,

$\underline{e}_\phi$), and a global Cartesian base frame ($\underline{e}_1$, $\underline{e}_2$, $\underline{e}_3$) is introduced and attached to the matrix. The relation between the two base frames reads as:

$$\underline{a}_{cart} = \begin{bmatrix} \sin\theta\cos\phi & \cos\theta\cos\phi & -\sin\phi \\ \sin\theta\sin\phi & \cos\theta\sin\phi & \cos\phi \\ \cos\theta & -\sin\theta & 0 \end{bmatrix} \cdot \underline{a}_{sph}, \tag{2.48}$$

where $\underline{a}_{cart}$ and $\underline{a}_{sph}$ represent the same vector expressed respectively in the cartesian and spherical coordinate system, θ is the co-latitudinal angle with $0 \leq \theta \leq \pi$ and ϕ is the longitudinal angle with $0 \leq \phi < 2\pi$ (see Fig. 2.5). Furthermore, in the presence of inclusions in the material which can reorient

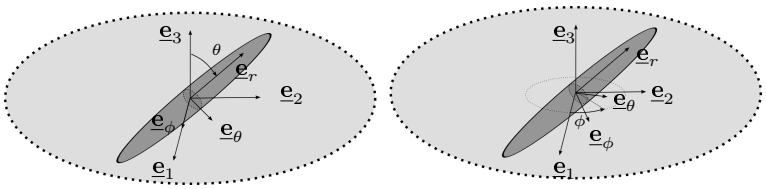

(A)First Eulerian angle θ (B)Second Eulerian angle ϕ

Figure 2.5: Definition of the two Euler angles θ and ϕ.

with the applied load, the evolution of the orientation vectors $\underline{e}_r$, $\underline{e}_\theta$, and $\underline{e}_\phi$ corresponding to each inclusion is determined by the microstructural spin $\boldsymbol{\omega}$ and microstructural strain rate $\boldsymbol{d}$ tensors of each inclusion via,

$$\dot{\underline{e}}_i = (\boldsymbol{d} + \boldsymbol{\omega}) \cdot \underline{e}_i, \qquad i = \{r, \theta\ ,\ \phi\}, \tag{2.49}$$

where $\dot{\underline{e}}_i$ is the time derivative of the base vector $\underline{e}_i$. According to the updated Lagrange formulation, the base vectors attached to each inclusion are updated as follows:

$$\underline{e}_r^{t+dt} = \left[(\boldsymbol{d}_r^t + \boldsymbol{\omega}_r^t)dt + \boldsymbol{I}\right] \cdot \underline{e}_r^t \quad \forall r \in \{1, 2, 3, ..., N\}, \tag{2.50}$$

where $\boldsymbol{I}$ is the second-order identity tensor. The update of the inclusion base vectors allows the update of the Euler angles defining the inclusion inclination, θ_r^{t+dt} and ϕ_r^{t+dt}, as well as of the concentration tensors, $\mathbb{A}_r^{t+dt}(\theta_r^{t+dt}, \phi_r^{t+dt})$ and $\mathbb{R}_r^{t+dt}(\theta_r^{t+dt}, \phi_r^{t+dt})$ through Eqs. (2.37) and (2.39).

Finally, combining the stress average rule (2.8) with the expression of the local mean stress in each inclusion (2.47), one gets the updated macroscopic Cauchy

stress $\boldsymbol{\Sigma}^{t+dt}$ in the form,

$$\begin{aligned}\boldsymbol{\Sigma}^{t+dt} &= \sum_{r=1}^{N} f_r \boldsymbol{\sigma}_r^{t+dt} + f_M \boldsymbol{\sigma}_M^{t+dt} \\ &= \sum_{r=1}^{N} f_r \boldsymbol{\sigma}_r^{t} + \left(\sum_{r=1}^{N} f_r \mathbb{C}_r^{eq^t} : \boldsymbol{D}^t \right) dt + f_M \boldsymbol{\sigma}_M^t + \left(f_M \mathbb{C}_M^{eq^t} : \boldsymbol{D}^t \right) dt, \\ &= \boldsymbol{\Sigma}^t + \left(\mathbb{C}_{hom}^t : \boldsymbol{D}^t \right) dt, \qquad\qquad \forall r \in \{1, 2, 3, ..., N\},\end{aligned} \tag{2.51}$$

whereby the homogenized "stiffness" tensor $\mathbb{C}_{hom}^t$ is defined as:

$$\mathbb{C}_{hom}^t = \sum_{r=1}^{N} f_r \mathbb{C}_r^{eq^t} + f_M \mathbb{C}_M^{eq^t}, \quad \forall r \in \{1, 2, 3, ..., N\}. \tag{2.52}$$

A summary of the numerical scheme is presented in Fig. 2.6.

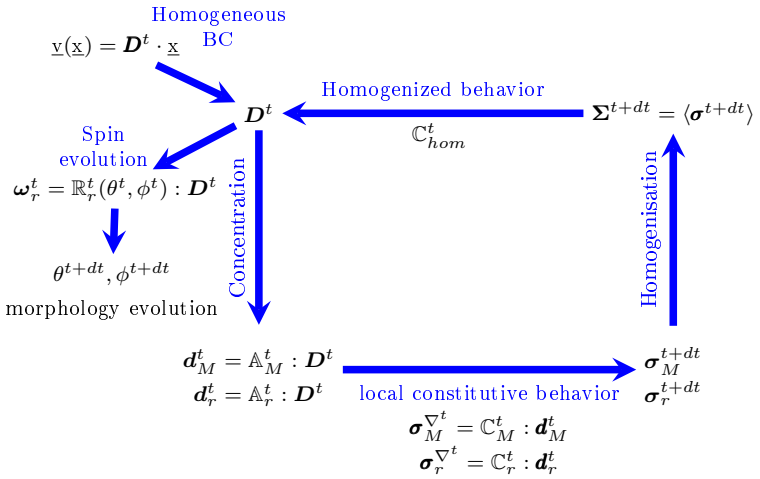

Figure 2.6: Numerical algorithm of homogenization scheme.

2.7 Extension to stress-driven load cases

One can consider a most complex case where traction forces are applied on the boundary of the RVE. The knowledge of the material conformation at the initial time is used in equation (2.52) to compute the homogenized stiffness. Then, the homogenized stiffness allows to calculate the strain rate in a forward Euler scheme as follows, knowing the macroscopic stress at all times,

$$\boldsymbol{D}^t = {\mathbb{C}_{hom}^t}^{-1} : \left(\frac{\boldsymbol{\Sigma}^{t+dt} - \boldsymbol{\Sigma}^t}{dt} \right) \tag{2.53}$$

Then, the previously described numerical scheme is adopted and allows to evaluate the macroscopic stress increment generated by this strain rate. Finally, this macroscopic increment of Cauchy stress is compared with the prescribed one. If there is a difference between the two values the calculation is repeated with the new homogenized stiffness in order to determine the correct strain rate. On the other hand, if the difference between the two macroscopic Cauchy stresses is negligible, we compute the macroscopic deformation gradient as follows,

$$\boldsymbol{F}^{t+dt} = \left(\boldsymbol{D}^t dt + \boldsymbol{I}\right) \cdot \boldsymbol{F}^t, \tag{2.54}$$

where $\boldsymbol{I}$ is the second-order identity tensor and the macroscopic deformation gradient at initial instant is assumed to be the identity matrix ($\boldsymbol{F}^{t=0} = \boldsymbol{I}$). This completes the computational scheme for applied traction forces on the boundary over a small time increment dt. A summary of the numerical scheme for imposed stress conditions is illustrated in Table 2.1.

1. Prescribed macroscopic Cauchy stress $\boldsymbol{\Sigma}^t$ and $\boldsymbol{\Sigma}^{t+dt}$ at time t and $t+dt$
2. Initialize the homogenized behavior of the material $\mathbb{C}^t_{hom}$ at time t according to Eq. (2.52)
3. Perform an iteration loop to applying the Cauchy stress $\Delta\boldsymbol{\Sigma} = \boldsymbol{\Sigma}^{t+dt} - \boldsymbol{\Sigma}^t$
   a) Compute macroscopic strain rate $\boldsymbol{D}^t$ at time t from the linear approximation Eq. (2.53)
   b) For all constituents perform down-scaling, local constitutive behavior and up-scaling
      (i) Compute microscopic strain rate $\boldsymbol{d}^t$ and spin $\boldsymbol{\omega}^t$ at time t from Eq. (2.41)
      (ii) Compute Cauchy microscopic stress $\boldsymbol{\sigma}^{t+dt}$ from Eq. (2.47)
      (iii) For all fibers compute updated orientation angles $\theta^{t+dt}, \phi^{t+dt}$ from from Eq. (2.50)
      (iv) Compute updated homogenized behavior of the material $\mathbb{C}^t_{hom}$ from Eq. (2.52)
      (v) Compute macroscopic Cauchy stress $\hat{\boldsymbol{\Sigma}}^{t+dt}$ from Eq. (2.51)
   c) Compare macroscopic Cauchy stresses (computed and prescribed) and compute the residual:
      $\boldsymbol{R} = \boldsymbol{\Sigma}^{t+dt} - \hat{\boldsymbol{\Sigma}}^{t+dt}$
   d) Check the tolerance: $||\boldsymbol{R}|| \leq$ tol, exit the algorithm, otherwise go back to step 3 and apply the residual $\boldsymbol{R}$ instead of $\Delta\boldsymbol{\Sigma}$
4. Update the homogenized behavior of the material $\mathbb{C}^{t+dt}_{hom}$
5. Compute the macroscopic deformation gradient $\boldsymbol{F}^{t+dt}$ from Eq. (2.54)

Table 2.1: Numerical algorithm for the constitutive model under imposed stress conditions

2.8 Extension to multi-scale approach for hierarchical structure of heterogeneous materials

Many materials and biological tissues, like bone or artery, exhibit a hierarchical microstructure, i.e. a close look at one phase may reveal its heterogeneous internal structure which impacts its mechanical behavior. It is then possible to model this hierarchical structure in a multi-scale approach by considering a lower scale RVE, which takes into account the heterogeneity of that phase (see Fig. 2.7). This lower RVE has a characteristic length l_2, with $l_2 \leq d$. Again, the RVE representing the phase must follow the scale separation rule, that is $d_2 \ll l_2$, with d_2 as the characteristic length of the lower scale heterogeneities, to build up the multi-scale homogenization scheme (see Fig. 2.7).

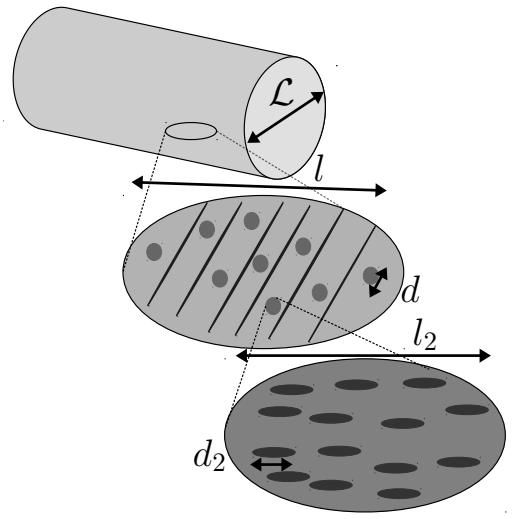

Figure 2.7: Representation of the different RVEs in a multi-scale homogenization scheme.

In the present study, a multi-scale approach is introduced by considering a lower scale RVE to model the heterogeneous structure of the material phase (see Fig. 2.8). The material properties of the heterogeneous inclusion in the upper scale is estimated by homogenization over the RVE of the lower scale. The orientation of heterogeneities in the lower RVE is taken into account by two Euler angles θ^{low} and ϕ^{low}, defining an orthonormal spherical basis ($\underline{e}_r^{low}$, $\underline{e}_\theta^{low}$, $\underline{e}_\phi^{low}$) with respect to the inclusion basis in the upper RVE, ($\underline{e}_r^{up}$, $\underline{e}_\theta^{up}$, $\underline{e}_\phi^{up}$). Accordingly, the upper base

frame, attached to the inclusion in the upper scale RVE, is defined with respect to the global base frame ($\underline{e}_1$, $\underline{e}_2$, $\underline{e}_3$) by the two Euler angles θ^{up} and ϕ^{up}. The two local bases are linked by the following base change relation:

$$\underline{a}^{low} = \begin{bmatrix} \sin\theta^{low}\cos\phi^{low} & \sin\theta^{low}\sin\phi^{low} & \cos\theta^{low} \\ \cos\theta^{low}\cos\phi^{low} & \cos\theta^{low}\sin\phi^{low} & -\sin\theta^{low} \\ -\sin\phi^{low} & \cos\phi^{low} & 0 \end{bmatrix} \cdot \underline{a}^{up}, \tag{2.55}$$

with $\underline{a}^{low}$ and $\underline{a}^{up}$ being the expressions of the same vector respectively in the lower and upper scale spherical coordinate systems, while another Eq. (2.55) related the coordinate systems ($\underline{e}_r^{up}$, $\underline{e}_\theta^{up}$, $\underline{e}_\phi^{up}$) and ($\underline{e}_1$, $\underline{e}_2$, $\underline{e}_3$).

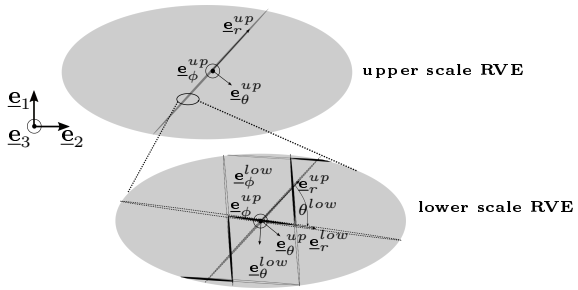

Figure 2.8: Representative Volume Elements for heterogeneous materials exhibiting a hierarchical microstructure.

The method to obtain the macroscopic effective constitutive relation is described hereafter, and follows the three previously described steps, i.e. (i) concentration of the applied loading into the different phases, (ii) use of the phase-specific constitutive relations, and (iii) use of the average rules to obtain the conjugated macroscopic quantities. In more details, for strain rate-driven load cases, it reads as:

Strain rate concentration The macroscopic strain rate $\boldsymbol{D}$ is localized in each inclusion of the upper scale RVE:

$$\begin{aligned} \boldsymbol{d}_r^{up} &= \mathbb{A}_r^{up} : \boldsymbol{D}, \\ \boldsymbol{\omega}_r^{up} &= \mathbb{R}_r^{up} : \boldsymbol{D}, \qquad \forall r \in \{1, ..., N^{up}\}, \end{aligned} \tag{2.56}$$

with N^{up} as the number of phases in the upper scale RVE. Then, the local strain rate $\boldsymbol{d}_I^{up}$ of the inclusion I on which a zoom is made is applied as a homogeneous boundary condition on the lower scale RVE. One can compute the local strain rate and spin tensors of the N_I^{low} phases in the lower scale RVE according to the

same Eqs. (2.35) and (2.36), i.e.:

$$\begin{aligned} \boldsymbol{d}_{r,I}^{low} &= \mathbb{A}_{r,I}^{low} : \boldsymbol{d}_I^{up}, \\ \boldsymbol{\omega}_{r,I}^{low} &= \mathbb{R}_{r,I}^{low} : \boldsymbol{d}_I^{up}, \qquad \forall r \in \{1,2,3,...N_I^{low}\}, \end{aligned} \tag{2.57}$$

where $\boldsymbol{d}_{r,I}^{low}$ is the strain rate in the lower scale phase r, $\boldsymbol{\omega}_{r,I}^{low}$ is the spin tensor of the inclusions of phase r of the lower scale RVE, and $\mathbb{A}_{r,I}^{low}$ and $\mathbb{R}_{r,I}^{low}$ are the respective concentration tensors in phase r of the lower scale RVE attached to inclusion I of the upper scale RVE.

Load-driven inclusion reorientation The evolution of the orientation vectors $\underline{e}_r^{low}$, $\underline{e}_\theta^{low}$, and $\underline{e}_\phi^{low}$ corresponding to the inclusion phase r in the lower scale RVE is determined by the microstructural spin $\boldsymbol{\omega}_{r,I}^{low}$ and microstructural strain rate $\boldsymbol{d}_{r,I}^{low}$ tensors of the inclusion in the lower scale via,

$$\dot{\underline{e}}_i^{low} = \left(\boldsymbol{d}_{r,I}^{low} + \boldsymbol{\omega}_{r,I}^{low}\right) \underline{e}_i^{low}, \qquad i \in \{r,\theta,\phi\} \tag{2.58}$$

where $\dot{\underline{e}}_i^{low}$ is the standard time derivative of $\underline{e}_i^{low}$. Similarly, for the upper scale RVE, the evolution of the base vectors attached to the upper scale RVE is determined by the following equation:

$$\dot{\underline{e}}_i^{up} = \left(\boldsymbol{d}_I^{up} + \boldsymbol{\omega}_I^{up}\right) \underline{e}_i^{up}, \qquad i \in \{r,\theta,\phi\} \tag{2.59}$$

Effective mechanical properties The homogenized mechanical properties are first computed for the lower scale RVE, according to Eq. (2.52). This effective "stiffness" tensor corresponds to the effective properties of inclusion I of the upper scale RVE. Accordingly, its expression reads as:

$$\mathbb{C}_I = \sum_{r=1}^{N_I^{low}} f_{r,I}^{low} \mathbb{C}_{r,I}^{eq^{low}} + f_{M,I}^{low} \mathbb{C}_{M,I}^{eq^{low}}, \qquad \forall r \in \{1,2,3,...,N_I^{low}\}. \tag{2.60}$$

where $f_{r,I}^{low}$ and $f_{M,I}^{low}$ are respectively the volume fractions of phase r and of the matrix in the lower scale RVE, $\mathbb{A}_{r,I}^{low}$ and $\mathbb{A}_{M,I}^{low}$ are the strain rate concentration tensors into the phase r and the matrix phase in the lower scale RVE, and $\mathbb{C}_{r,I}^{low}$ and $\mathbb{C}_{M,I}^{low}$ are the fourth-order stiffness tensors of the phase r and of the matrix in the lower scale RVE, all of them being attached to the phase I of the upper RVE. $\mathbb{C}_{r,I}^{eq^{low}}$ and $\mathbb{C}_{M,I}^{eq^{low}}$ follow from Eq. (2.46), incorporating into this equation the concentration tensors $\mathbb{A}_{r,I}^{low}$, $\mathbb{A}_{M,I}^{low}$, and $\mathbb{R}_{r,I}^{low}$, as well as the local stress tensor $\boldsymbol{\sigma}_{r,I}^{low}$. $\mathbb{C}_I$ is the homogenized stiffness tensor over the lower scale RVE, which allows to

compute the effective (homogenized) Cauchy stress tensor over the lower scale RVE. A summary of the numerical scheme is illustrated in Fig. 2.9.

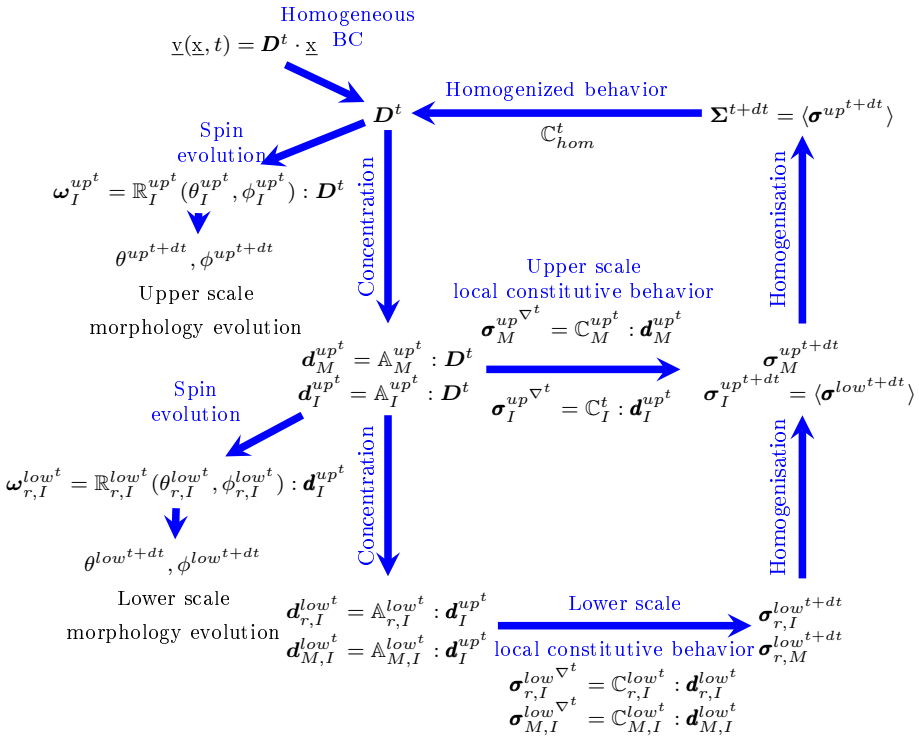

Figure 2.9: Numerical algorithm for the multi-scale homogenization scheme.

2.9 Conclusion

In this chapter, we developed the framework of finite strain continuum micromechanics. As the RVEs undergo large morphological changes, a Mori-Tanaka scheme extended to inclusion reorientation is adopted to compute analytical expressions for the strain rate and spin concentration tensors. Based on homogenization theory, these concentration tensors are then used to compute the averaged strain rate and spin tensor in each phase of RVE from the applied macroscopic strain rate on the boundary.

The phases in the RVE are represented as infinitely long cylinders embedded in a matrix, where Mori-Tanaka scheme defines the interaction between different phases in which a local hypoelastic constitutive model is defined. The computed spin tensor for each phase determines the load-induced rotation of the phase. This approach will ensure the non-affine deformation of the phases in the RVE.

Furthermore, the method is extended to a multi-scale homogenization scheme to be capable of modeling the hierarchical structure of artery.

3 Multi-scale modelling of the arterial adventitia

Contents

Résumé

Afin de développer un modèle de comportement de l'artère motivé par la microstructure, l'approche micromécanique multi-échelle qui a été expliquée au chapitre 2 a d'abord été appliquée à l'adventice, qui est la couche externe de l'artère. Ce chapitre présente les étapes nécessaires pour construire le modèle de l'adventice avec des volumes élémentaires représentatifs spécifiques à plusieurs échelles élaborés à partir d'observations microstructurales du tissu. Ensuite, la simulation de la traction uniaxiale a été réalisée sur le modèle d'adventice pour étudier le rôle des changements de morphologie des réseaux de fibres de collagène et d'élastine et la contribution de ces réseaux à la réponse mécanique. Enfin, ces résultats ont été comparés aux résultats expérimentaux et aux observations afin d'évaluer la capacité du modèle micromécanique à prédire les observations expérimentales.

3.1 Introduction

In order to develop a microstructurally motivated constitutive model for the artery, the multi-scale micromechanical approach which was explained in Chapter 2 was first applied to the arterial adventitia layer. This chapter presents the steps required to construct the arterial adventitia model with specific multi-scale RVEs from the multiphoton image stacks of the tissue. Then, the uniaxial tensile simulation was performed on the adventitia model to investigate the role of the collagen and elastin fiber networks morphology changes and contribution of these networks in the mechanical response. Finally, these results were compared against the experimental results and observations to evaluate the capacity of the micromechanical model to predict the experimental evidences.

3.2 Micromechanical representation of the adventitia

3.2.1 Modelling the adventitia at the scale of a few hundreds of micrometers

As detailed in Chapter 1 and illustrated in Fig. 3.1, the microstructure of the adventitia is very complex and cannot be resolved in full details. As a remedy, we

here use the previously introduced theoretical framework to propose a multi-scale model of the adventitia.

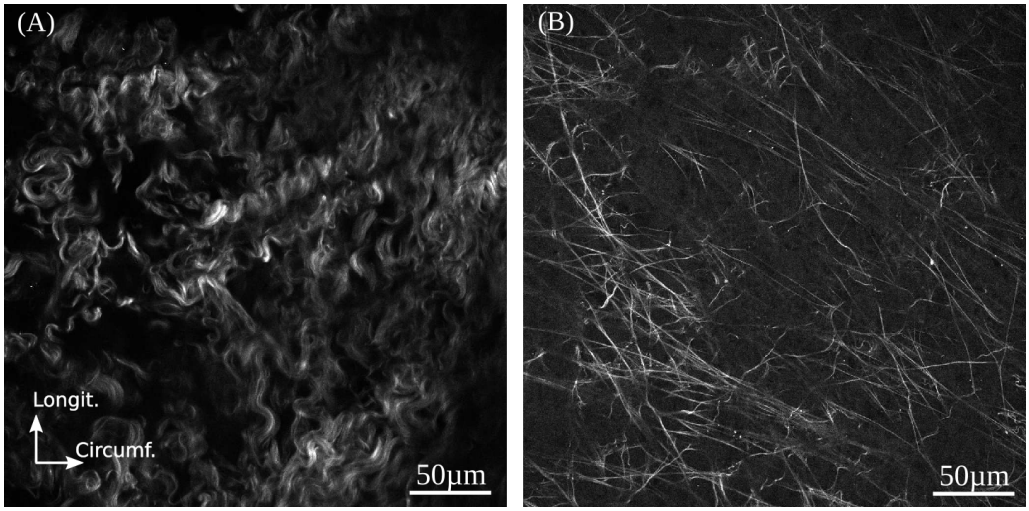

Figure 3.1: Multiphoton microscopic imaging of fibers in the adventitia [82]. (A) collagen bundles; (B) elastin fibers.

The starting point is the definition of a RVE, with a characteristic length l, fulfilling the scale separation requirements, see Eq. (2.1) in Chapter 2. The mechanical properties of the adventitia result in a first approximation from the interplay of the collagen and elastin fiber networks embedded in a soft ground substance matrix. Analysis of microscopy images reveals that collagen bundles have a diameter ranging between 5-10 μm [139], while the adventitial elastin fibers have a diameter of 1-6 μm [49] (see Fig. 3.2). As regards to the characteristic size of the RVE, confocal microscopic stacks of images reveal that $l = 100$ μm is a convenient choice for having a sufficiently large number of fibers so as to be representative of the adventitia microstructure.

Given these characteristic length scales, the description of the RVE needs to be reduced to mechanically relevant details. Based on the fiber morphology, we choose to model both fiber networks as infinitely-long cylindrical inclusions, with orientation characterized by the two Eulerian angles θ and ϕ, i.e. by the classical spherical coordinates as defined by Fig. 3.3 and Eq. (2.48) in Chapter 2. The remaining space of the RVE is filled by the ground substance matrix. In the sequel, the collagen bundle phase is labeled by subscript "$b-ad$", while the

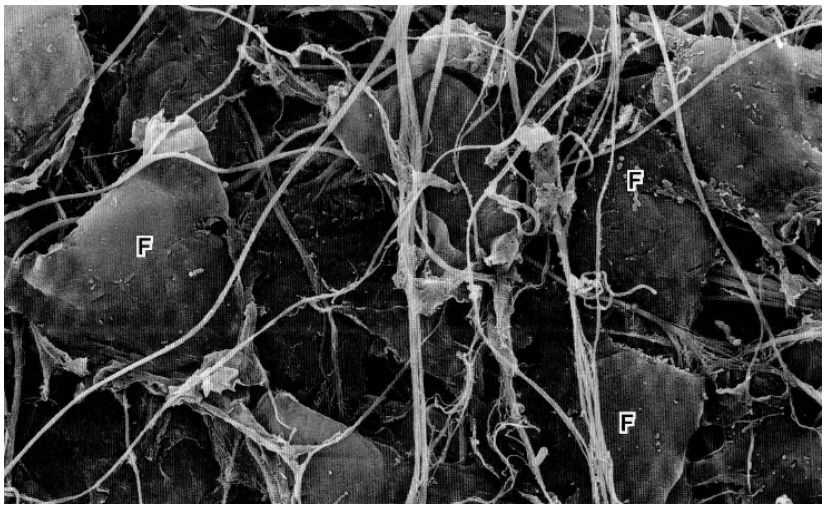

Figure 3.2: Elastin fiber and fibroblast (F) in aortic adventitia of rat, magnification $\times 1,700$ [140].

elastin phase is labeled by subscript "$el-ad$", and the matrix phase by "$m-ad$". Accordingly, the respective volume fractions of each of these phases read as f_{b-ad}, f_{el-ad}, and f_{m-ad}, with their sum being equal to 1.

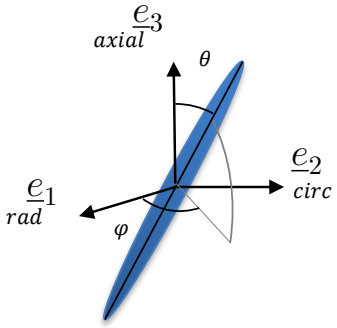

Figure 3.3: Orientation of a fiber in the arterial wall. θ represents the fiber inclination with respect to the axial direction of artery, and ϕ its direction in the radial-circumferential plane.

The morphology of the adventitia layer motivates the choice of a Mori-Tanaka scheme to account for all interactions between the different phases.

3.2.2 Modelling the collagen bundles of adventitia at the scale of a few micrometers

The collagen bundles modeling needs to be further refined, since collagen bundles are made, at a lower scale, of a staggered arrangement of collagen fibrils. As reviewed in Chapter 1, the recruitment process of collagen fibers has a significant impact on the mechanical response of arteries and therefore needs to be accounted for. Following the multi-scale homogenization procedure described in Section 2.8 of Chapter 2, we introduce a lower scale RVE, with a characteristic length of 5-10 μm, i.e. satisfying the scale separation conditions, and hosting heterogeneities in the form of infinitely long cylindrical inclusions representing the collagen fibrils, which have a characteristic size of 30–100 nm [139]. The remaining volume of the RVE is made of a ground substance matrix. The fibrils and matrix are respectively labeled by subscripts "$f-b$" and "$m-b$", and their respective volume fractions read as f_{f-b} and $f_{m-b} = 1 - f_{f-b}$. We assume an helicoidal crimping: the collagen fibers are isotropically distributed in the transverse plane, i.e., $\phi \in [0 - 2\pi]$.

Once again, a Mori-Tanaka scheme is chosen to account for fibers-matrix interactions. The resulting multi-scale micromechanical model representing the arterial adventitia layer is illustrated in Fig. 3.4.

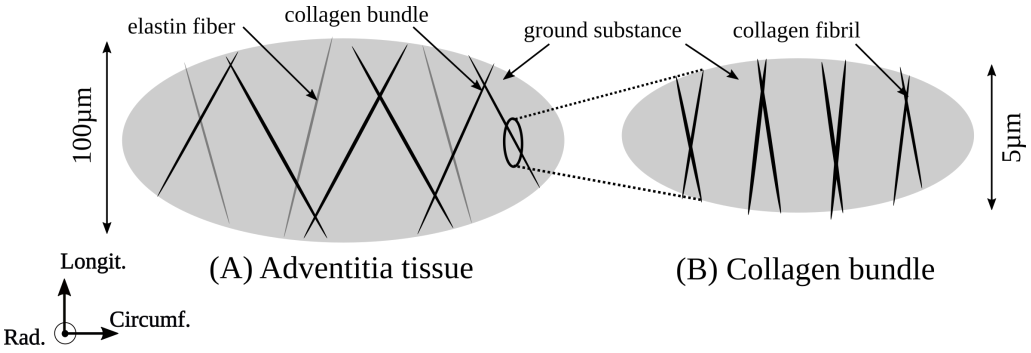

Figure 3.4: Micromechanical RVEs representing the adventitia. (A) RVE representing the adventitia tissue scale; (B) RVE representing the collagen bundles.

3.3 Determination of the parameters of the model

The proposed multi-scale approach for the mechanical modeling of the arterial adventitia introduces several physical and morphological parameters whose determination is discussed in the present section. It is important to note that, among all parameters, the vast majority are actually universal parameters, since their values will remain fixed, based on experimental observations. First, as reviewed in Chapter 1, all adventitial fiber networks have a negligible transmural angle, and therefore all ϕ angles are set to $\frac{\pi}{2}$.

3.3.1 Mechanical properties of elementary constituents

Our adventitia model introduces three distinct elementary constituents namely: (i) type I collagen fibers, (ii) elastin fibers, and (iii) ground substance matrix. We assign to these three constituents a hypoelastic constitutive behavior, as introduced in the Section 2.4 of Chapter 2. Despite the vast literature discussing the possible anisotropy of these constituents, we assume isotropic linear elastic properties for all constituents, i.e. the stiffness tensor of phase r, $\mathbb{C}_r$, is defined as :

$$\mathbb{C}_r = 3k_r\mathbb{J} + 2\mu_r\mathbb{K}, \tag{3.1}$$

whereby k_r and μ_r are respectively the bulk and shear moduli of phase r, which can be expressed as functions of the Young's modulus E_r and of the Poisson's ratio ν_r by $k_r = \frac{E_r}{3(1-2\nu_r)}$ and $\mu_r = \frac{E_r}{2(1+\nu_r)}$. Furthermore, $\mathbb{J}$ is the volumetric part of the fourth-order identity tensor $\mathbb{I}$ with components $J_{ijkl} = \frac{1}{3}\delta_{ij}\delta_{kl}$, and $\mathbb{K}$ is its deviatoric part, $\mathbb{K} = \mathbb{I} - \mathbb{J}$. The components of the fourth-order identity tensor $\mathbb{I}$ read as $I_{ijkl} = \frac{1}{2}(\delta_{ik}\delta_{jl} + \delta_{il}\delta_{jk})$. δ_{ij} stands for the Kronecker delta.

The literature review of Section 1.5 in Chapter 1 was guided our choice for the isotropic properties of collagen fibers, elastin fibers, and ground substance, which are summarized in Table 3.1. For all constituents, the Poisson's ratio is taken equal to 0.34 [143, 25].

Constituent	Young's modulus [MPa]	Specimen & experiment	Reference
Collagen fibril type I	250	Tensile test on abovine Achilles tendon collagen type I	[48, 141]
Elastin fiber	1	Tensile test on a water-swollen bovine ligamentum	[1]
Ground substance	0.1	Resistance of single cell to elastic deformation	[4, 130, 106, 11]

Table 3.1: Mechanical parameters of the adventitita micromechanical model.

3.3.2 Volume fraction of elementary constituents

Amount of collagen fibrils in the collagen bundles

Different studies report cross-sectional views of collagen bundles, imaged by means of transmission electron microscopy, see Fig. 3.5. Automatic segmentation of these microscopy images (using the Otsu method [103] to determine the thresholding grey value) allows to access the volume fraction of these fibrils, for different tissues, which we report in Table 3.2.

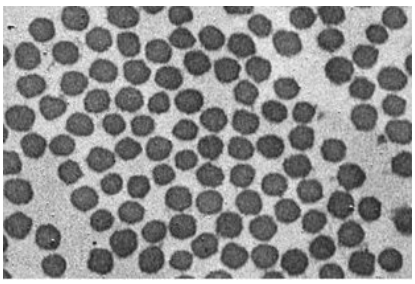

Figure 3.5: Cross section of a collagen bundle of a mouse adventitia [137].

Specimen	Imaging method	Volume fraction	Reference
Mouse blood vessel adventitia	electron microscopy	63%	[93]
Mouse thoracic aorta adventitia	electron microscopy	51%	[137]
Rat inferior vena cava adventitia	two-photon fluorescent microscopy	31%	[52]
Rat aorta adventitia	transmission electron microscope	30%	[7]

Table 3.2: Collagen fibril volume fraction within a collagen bundle

This literature survey motivates our choice of a volume fraction of collagen fibrils of 30 %. An analysis is performed to understand the effect of a variation of this volume fraction on the overall result, see section 3.5 of this chapter.

Amount of collagen bundles in the adventitia

The stacks of adventitia images of rabbit carotid arteries taken by Witold Krasny [82] were analyzed with ImageJ to separate the two recorded channels: second harmonic generation (collagen bundles signals) and autofluorescence (elastin fibers signals). Then, the Otsu thresholding technique [103] is performed to extract binary images. Since the fraction of collagen is not uniform through the thickness of the arterial adventitia, the fraction is computed from taking the average through the image stacks of each sample. Finally, we set the fraction of collagen bundles to 30%, corresponding to the average of the fractions computed for the nine tested samples, which is in agreement with other studies [16, 17].

Specimen	Imaging method	Volume fraction	Reference
Porcine coronary adventitia	multiphoton microscopy	33%	[17]
Porcine coronary adventitia	multiphoton microscopy	33%	[16]
Rabbit carotid adventitia	multiphoton microscopy	30% ± 10%	Image processing from [82]

Table 3.3: Reported values for the volume fraction of collagen bundles in the adventitia

Amount of elastin fibers in the adventitia

In the literature, the amount of elastin fibers has been evaluated in different tissue samples by a commercial image analysis software such as SIGMA SCAN PRO 5 [129] or ImageJ [43]. We also processed the different stacks of images resulting from uniaxial tensile tests on rabbit carotid arteries performed by Witold Krasny [82]. The microscopic images of the adventitia tissue were analyzed with ImageJ and the Otsu thresholding technique [103] performed on the autofluorescence channel allows to access the elastin volume fraction. All values are reported in Table 3.4. The last line of Table 3.4 corresponds to our own evaluation of the elastin fraction. We noticed a great variation in the elastin fraction among the different samples. Given the higher values reported in the literature, we finally decided to adopt a volume fraction of 20%. The sensitivity of the model with respect to this parameter will be discussed later.

Specimen	Imaging method	Volume fraction	Reference
Porcine coronary adventitia	multiphoton microscopy	25.7%	[137]
Porcine coronary adventitia	multiphoton microscopy	22%	[17]
Rabbit carotid adventitia	multiphoton microscopy	15% ± 10%	Image processing from [82]
Porcine thoracic adventitia	light microscopy	5%	[129]

Table 3.4: Reported values for the volume fraction of elastin fibers in the adventitia

3.3.3 Orientation of the different fiber networks

Orientation of the collagen fibrils in the collagen bundles

The fiber waviness (or its inverse, the fiber straightness) is an often-reported parameter for collagen bundles. It is defined as the ratio of the total length of the collagen bundle on the end-to-end distance of the crimped collage bundle. The fiber straightness P is directly related to the orientation of the crimps, through the following relation: $\cos(\theta) = P$, whereby θ is the angle between the main bundle axis and the local crimp orientation, see Fig. 3.6. Table 3.5 reports the values collected from the literature on different tissue samples. We here adopt the average value of all values reported in Table 3.5. Once again, a sensitivity analysis on this parameter will be performed in a later section.

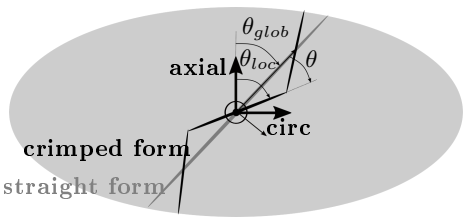

Figure 3.6: Representative straight form and crimped form of collagen bundle and corresponding angles.

Specimen	Straightness	Corresponding θ	Reference
Porcine coronary adventitia	0.85	31°	[160]
Porcine coronary adventitia	0.85	31°	[22]
Porcine coronary adventitia	0.82	35°	[19]
Porcine coronary adventitia	0.81	36°	[19]
Rabbit carotid adventitia	0.8	37°	[123]
Rabbit carotid adventitia	0.72	44°	[114]

Table 3.5: The waviness and corresponding local angle of collagen bundles

Orientation of the collagen bundles

The orientation of fibers was analyzed using orientationJ, a series of ImageJ plugins for directional image analysis [107, 114], which was employed previously to compute the global orientation and waviness of collagen bundles in the axial-circumferential plane. Through this method, they extracted a global orientation at around 45° for the collagen bundles of the adventitia layer in the relax condition [114]. However, since this parameter is difficult to estimate from our images, and since the results are very sensitive to this parameter, we decided to determine this parameter by curve fitting.

Orientation of the elastin fibers

Microscopic observations [17, 19, 82] show that the elastin fibers are mainly oriented along the axial direction, i.e. $\theta_{el-ad} = 0$.

The summary of model parameters and constants is presented in Table 3.6.

Parameters		Collagen	Elastin	Matrix
mechanical constant		$E_b = 250$ MPa	$E_{el} = 1$ MPa	$E_m = 0.01$ MPa
		$\nu_b = 0.34$	$\nu_e = 0.34$	$\nu_m = 0.34$
volume fraction	upper scale	$f_{b-ad} = 30\%$	$f_{el-ad} = 20\%$	$f_{m-ad} = 1 - \sum_i f_i$
	lower scale	$f_{f-b} = 30\%$	NA	NA
orientation	upper scale	$\theta_{b-ad} =$ Free parameter	$\theta_{el-ad} = 0°$	NA
		$\phi_{b-ad} = 90°$	$\phi_{el-ad} = 90°$	NA
	lower scale	$\theta_{f-b} = 35°$	NA	NA
		$\phi_{b-ad} = 90°$	NA	NA

Table 3.6: The summary of arterial adventitia model parameters and constants

3.4 Results

In this section, we validate the micromechanical model by comparing our model predictions with the macroscopic mechanical response obtained experimentally on each layer of human coronary arteries according to experiments from [63] and of human thoracic aorta according to [147]. This validation was performed individually for the adventitia layer. The parameters of the model were chosen based on Section 3.3.2 and summarized in Table 3.6. The only free parameter of the model, the global angle of collagen bundles in the adventitia θ_{b-ad}, was calibrated by minimizing the gap between experimental and computational stress-strain curves using a genetic algorithm. Furthermore, as a first estimate, a linear elastic representation of the media was considered along with the adventitia micromechanical model in order to evaluate the model by comparing the mechanical response and kinematics of the fibers with experiments performed by [82] on rabbit carotid artery.

3.4.1 Tensile test on the arterial adventitia

Uniaxial tensions were simulated based on the micromechanical model of the adventitia in order to compare the predicted mechanical response with the experimental results according to [63] (see Fig. 3.7(a)) and also according to [147] (see Fig. 3.7(b)) individually in the circumferential and longitudinal directions. A genetic algorithm was employed to fit the circumferential and longitudinal results simultaneously with the experiment by adjusting θ_{b-ad} as a free parameter. An orientation of $\theta_{b-ad} = 38.5°$ for human coronary artery and $\theta_{b-ad} = 40°$ for human thoracic aorta was obtained, which leads to a good agreement between model predictions and experimental results. Those values of θ_{b-ad} are also in good agreement with the measurements reported by [124] being 40° for human abdominal aortas.

Furthermore, the evolution of fiber angles were predicted by the model during uniaxial tension, individually in circumferential and longitudinal directions (see Fig. 3.8(b)). They are in good agreement with experimental observations, namely the bundles tend to align with the direction of tension at large stretches. Note that fiber alignment is not completely circumferential or longitudinal at the end of the simulation, as also observed by Witold Krasny during his experiments [82, 81].

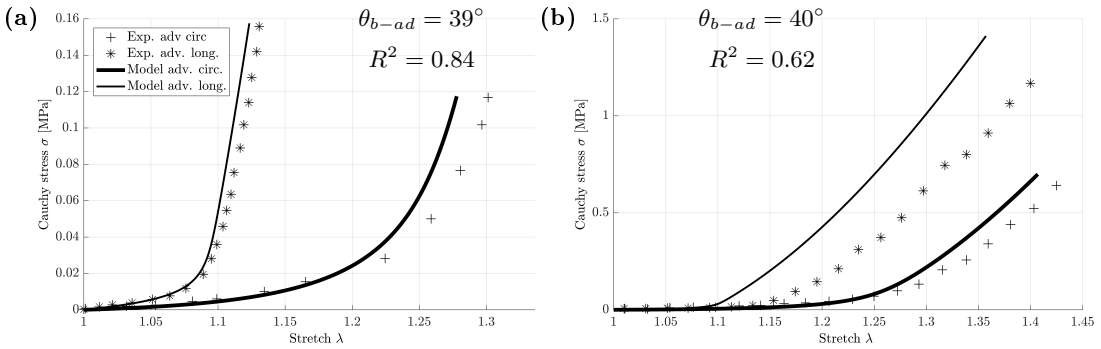

Figure 3.7: Macroscopic mechanical response of adventitia, (a) human coronary artery according to [63] and (b) human thoracic aorta according to [147] . The free parameter θ_{b-ad} and R^2 are reported for each tissue.

We compared the bundle rotations with the affine kinematic model, where the θ angle evolution is given by the following equation:

$$\theta = \tan^{-1}\left(\frac{\lambda_{circ}}{\lambda_{long}} \tan\Theta\right) \tag{3.2}$$

whereby λ_{circ} and λ_{long} respectively stand for the measured circumferential and longitudinal stretches and Θ is the initial bundle orientation.

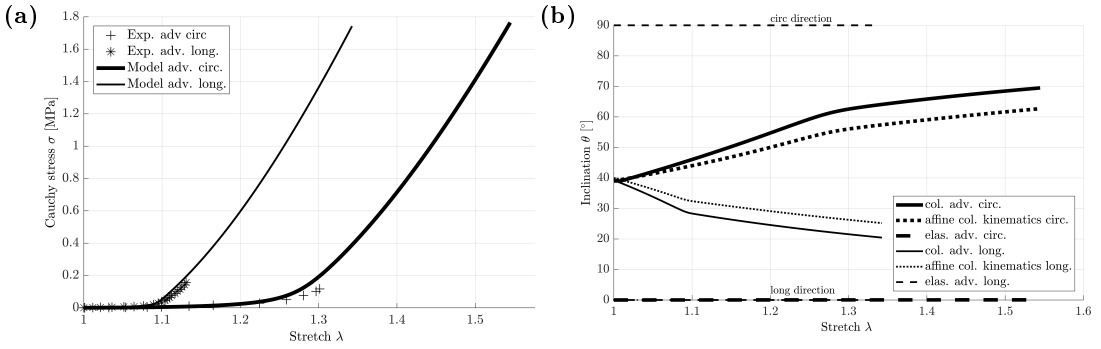

Figure 3.8: (a) Macroscopic mechanical response of adventitia at high stress. (b) Evolution of fiber angles under uniaxial tension in the adventitia.

The comparison between the bundle kinematics predicted by our model and the affine kinematics shows that the affine kinematics is a good approximation of the bundle kinematics for a restricted range of stretch, but underpredicts the bundle rotation as compared to our model; similar observations were also made

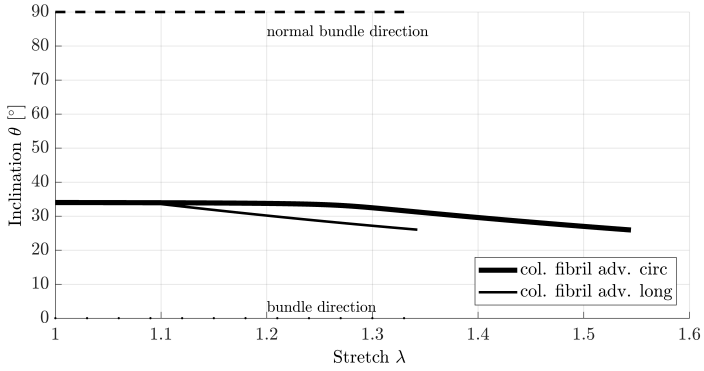

Figure 3.9: Evolution of fibril angle under uniaxial tension

when comparing experimentally-observed bundle rotation to the affine kinematics. The model is also able to predict the fibril decrimping, where fibrils tend to align with the bundle direction, as shown on Fig. 3.9 (although the predicted decrimping remains very limited here). It is interesting to notice that the decrimping does not occur from the beginning of the load application, which is in agreement with experimental observations [82, 22]. In the present model, the non linearity of the mechanical response arises from the combined reorientation of the collagen bundles and fibrils, while the elastin fibers exhibit very limited reorientations (again in good agreement with experiments).

3.4.2 Tensile test on artery

Finally, the global response of the arterial wall was computed by averaging across the whole thickness, pooling together the adventitia and the media in order to compare the results of the model with the experiment performed on a carotid artery strip [82]. The arterial structure is stratified. Therefore, when loading the structure in directions parallel to the layers, the average response is equal to the Voigt bound, and reads as:

$$\boldsymbol{D}_{artery} = \boldsymbol{D}_{adv} = \boldsymbol{D}_{med} \tag{3.3}$$

$$\boldsymbol{\sigma}_{artery} = f_{adv}\,\boldsymbol{\sigma}_{adv} + f_{med}\,\boldsymbol{\sigma}_{med} \tag{3.4}$$

As a first estimate the mechanical response of the media layer considered as a linear elastic with Young's modulus of E_{med}. Parameters of the adventitial micromechanical model are chosen identical to the previous validation case. Nevertheless, the only free parameter of the model, i.e. the global orientation

of collagen bundles θ_{b-ad}, was chosen as a free parameter and determined by calibrating the modeled response against experiments using a genetic algorithms. Choosing $\theta_{b-ad} = 68°$ for sample preconditioned longitudinally and $\theta_{b-ad} = 31°$ for sample preconditioned circumferentially lead to the best fitting with $R^2 = 0.67$. These values of θ_{b-ad} were also in good agreement with the morphology of the tissue. Fiber tracking was performed on few stacks of images recorded by Witold Krasny [82], and it was interesting to notice that the preconditionning of the sample induces a preferred global orientation of the collagen bundles: on these processed stacks, a global orientation of 60° ±10° was obtained in the longitudinal direction, whereas the circumferential sample exhibited a global orientation of 35° ±10°. This justifies the use of two different values for the two loading directions. Interestingly also, the global orientation was found to be further away from the 45° angle as compared to the tests performed on the adventitia alone on porcine arteries. The mechanical responses of the arterial model, taking into account the media as a linear elastic with different Young's modulus (E_{med}) of 0.1, 0.5 and 1 MPa are illustrated in Fig. 3.10.

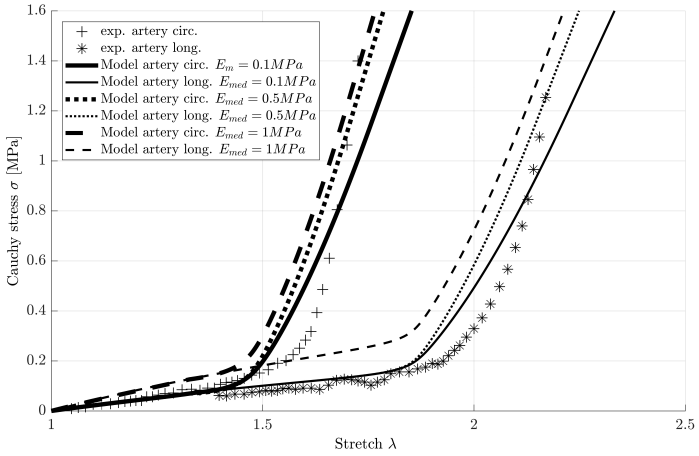

Figure 3.10: Comparison of the mechanical response of the model with the experiment carried out by [82] for whole carotid artery sample, taking into account the media as a linear elastic material with different Young's moduli E_{med}, 0.1, 0.5 and 1 MPa.

Accounting for the media as a linear material is a good first approximation, since it allows to retrieve the correct initial slope of the curve (which would be

much smaller if no media would have been accounted for). However, developing a multiscale model for the media would permit to gain in non linearity and anisotropy of the global mechanical response of the tissue, as will be shown in the next chapter.

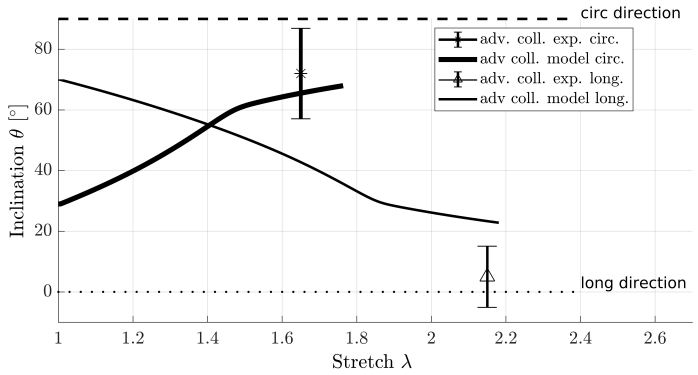

Figure 3.11: Comparison of the fiber kinematics with the experiments carried out by [82] for whole carotid artery sample.

Our model also allows to compare the predictions of the reorientation of the collagen bundles to the experimentally measured ones: Very good agreement is reached, as shown on Fig. 3.11.

3.5 Discussion

The multiscale micromechanical approach has been used to model the nonlinear and anisotropic mechanical responses of adventitia including directly phenomena occurring at the microscopic scale such as collagen fiber recruitment and non-affine fiber rotations. The objective was to propose a model for the adventitia layer built on the minimum of microstructural information, which is necessary to obtain reliable predictions of macroscopic mechanical behavior. To this aim, the main orientation of collagen and elastin fibers was obtained from image analysis of the adventitia images and considered in our representative volume element. Note that modeling the main fiber orientation instead of the fiber networks was also used in the well-established soft tissue models [45, 62, 61, 63].

3.5.1 Non-linearity

The use of hypoelasticity in the framework of micromechanical modeling permits to account for the large deformation of the tissue and the microstructural evaluation (non-affine fiber rotations). While, hypoelasticity has been previously used to model soft tissue biomechanics [36, 37]. In our model, the constituents of the model (elastin fiber, collagen fibril, and soft ground matrix) were modeled as linear elastic material (hypoelastic modulus and the hypoelastic Poisson's ratio) and the only source of non-linearity is due to the fiber reorientation. The fibers at upper scale RVE reoriented toward the load direction (fiber decrimping, see Fig. 3.8 (b)), where the two regimes of fiber reorientation were observed; (i) affine fiber rotation at low stresses, where the fibers have the same deformation as matrix, (ii) non-affine fiber rotation at higher stresses, where the fibers can generate shear stresses to rotate more than the matrix, which is in good agreement with experimental observations [82, 81]. Furthermore, the fibrils in the lower scale RVE tend to align with the fiber direction (fibril decrimping, see Fig. 3.9), where the decrimping does not happen right after the load application in agreement with the experimental observations [82, 22].

3.5.2 Anisotropy

In the model, at the lower scale, the matrix phase and collagen fibrils are isotropic materials, while the homogenized RVE (collagen bundle at upper scale) behaves anisotropically. Therefore, at the upper scale, the collagen bundles are anisotropic, while the matrix is isotropic and finally the homogenized response of the adventitia behaves anisotropically. The shape and the orientation of the fibers and fibrils phase within the RVEs dictate the anisotropy behavior of the model. This hierarchical structure and preferred orientation of constituents have been often seen in the biological tissues, where the micromechanical framework has been applied before to model this anisotropic behavior in bone [40, 41, 39].

3.5.3 Sensitivity analysis on load increment size

The developed multiscale model is highly non linear, which requires the development of an incremental algorithm, as developed in Chapter 2. Besides, the implicit dependence of the different concentration operators on the orientations

of the inclusions were solved with an explicit scheme for the discretization of the equations. We therefore propose a sensitivity analysis to verify the convergence of the results for different increment sizes. The results are reported in Fig. 3.12, in which the variation of mechanical response was not significant. Hence, increments of 0.2 kPa were chosen to perform the simulations.

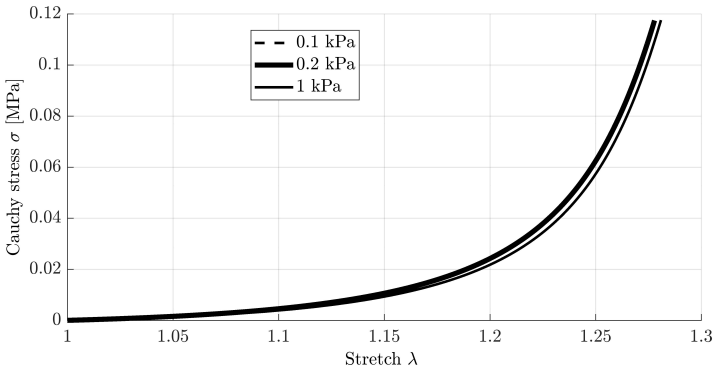

Figure 3.12: Increment size of load step in simulation of uniaxial tension on arterial adventitia

3.5.4 Sensitivity analysis on the collagen orientation and fraction at both scales

We extended our sensitivity analysis to all parameters of the models whose values exhibited variations in the literature, namely: the volume fractions of collagen fibrils and bundles and their orientations. For each parameter, we here show its impact on the response while maintaining all other parameters constant and equal to the value indicated above in Table 3.6.

The most influential parameter is the orientation of the collagen bundles: the variation of only 4° in the bundle orientation produces in fact the similar scattering in the mechanical response as the variation of 15° in the fibril orientation (compare Fig. 3.13(a) and Fig. 3.14(a)). Increasing the angle between collagen bundles and direction of the load (i.e. in circumferential tension $90-\theta_{b-ad}$) leads to increasing the time it takes to stiffen the material, since it takes more time for the fiber to reorient and to align with the load direction. As seen in Fig. 3.13(b), by increasing the angle between collagen bundles and direction of the load, the fiber is aligned with the direction of the load at higher stretches. While by increasing the angle between collagen fibrils and collagen bundles, collagen fibrils reorient less (see

Fig. 3.14(b)).

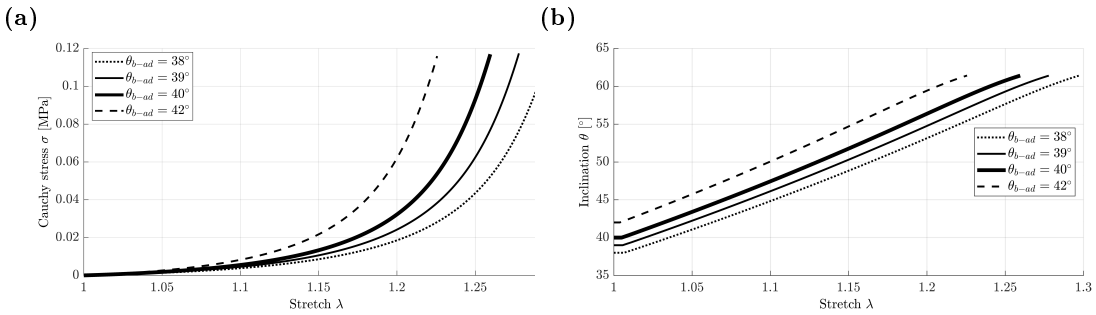

Figure 3.13: The impact of global orientation of collagen bundles on the mechanical response (a) and fiber kinematics (b) of arterial adventitia

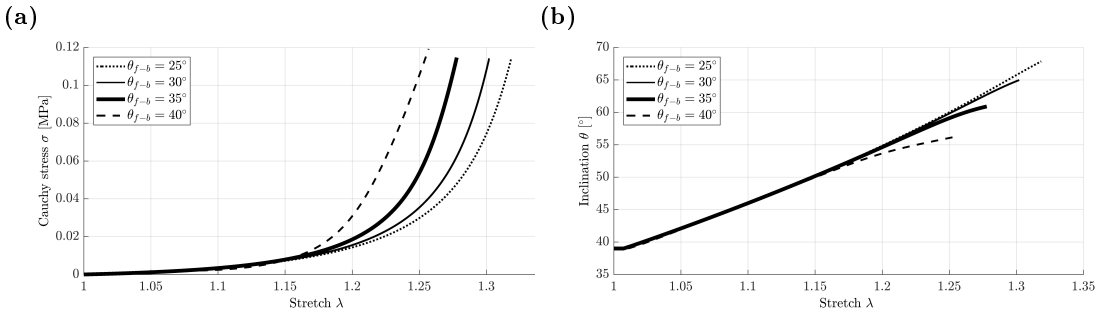

Figure 3.14: The impact of orientation of collagen fibrils on the mechanical response (a) and fiber kinematics (b) of arterial adventitia

The precise volume fraction of collagen bundles does influence the results, whereas the fraction of fibrils does not (compare Fig. 3.15 and Fig. 3.16). Increasing the volume fraction of collagen bundles leads to decreasing the time needed to stiffen the material. In this condition, we have less volume fraction of ground substance and more interaction between bundles which leads to faster reorientation with the load direction.

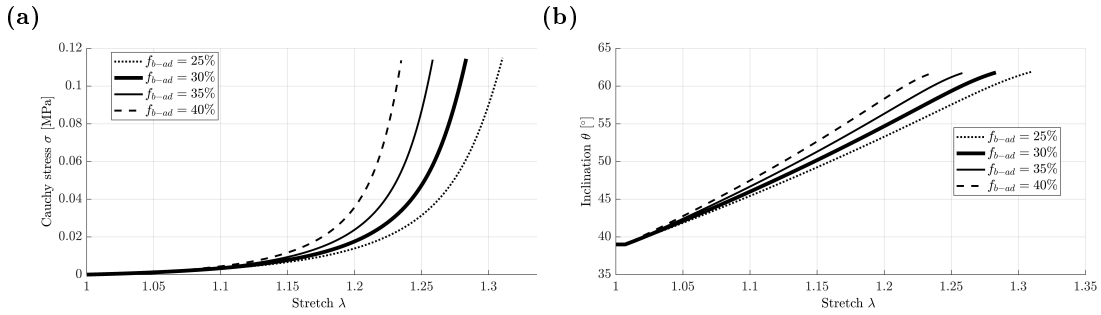

Figure 3.15: The impact of collagen bundles volume fraction on the mechanical response (a) and fiber kinematics (b) of arterial adventitia

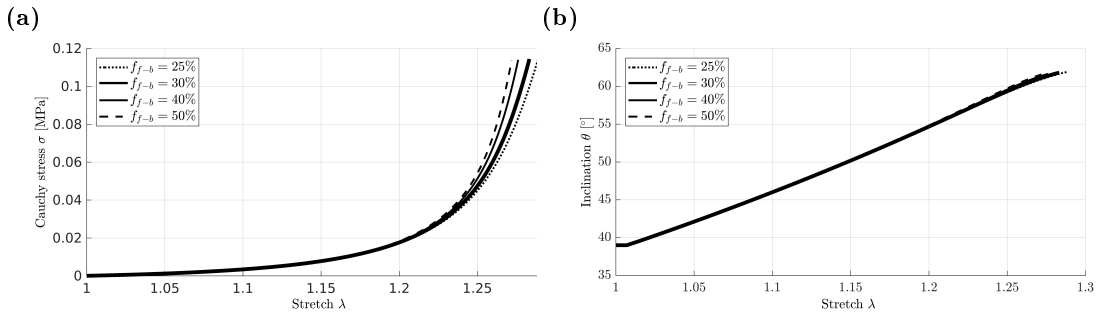

Figure 3.16: The impact of collagen fibrils volume fraction on the mechanical response (a) and fiber kinematics (b) of arterial adventitia

Parameters at the lower scale RVE have less impact on the mechanical response and fiber kinematics of arterial adventitia than parameters in the upper sclae. This sensitivity analysis together with the difficulty to determine it by post-processing of image stacks confirm our choice of determining the bundle inclination through a fitting process based on a genetic algorithm.

3.5.5 Contribution of the matrix stiffness

We here test how the matrix stiffness affects the mechanical response of the adventitia. To this aim, the matrix Young's modulus at both scales was varied in the range [1-100] kPa, and the effect is shown in the Fig. 3.17. The matrix stiffness influences the different slopes of the mechanical response: at low stresses, when collagen is still crimped and disoriented, as expected, the stiffer the matrix,

the stiffer the response; at large stresses however, the tendency is reverse: the stiffest the matrix, the longer it takes to stiffen the material: this is due to a more limited contrast between the stiffness of the rotating inclusions and the one of the matrix.

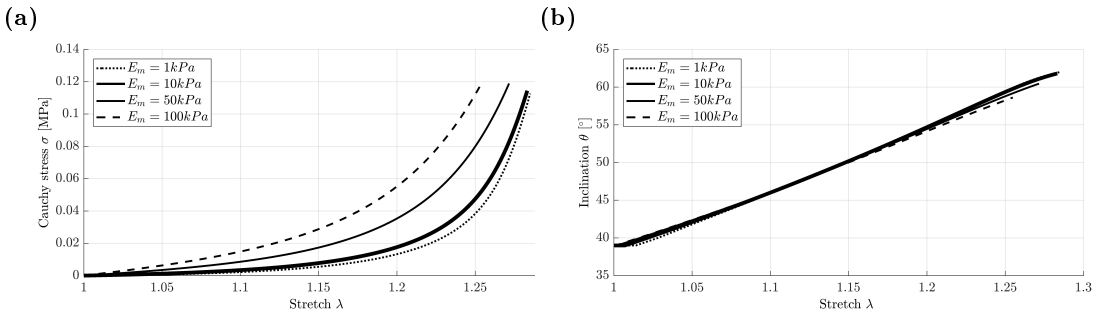

Figure 3.17: The impact of the matrix stiffness on the mechanical response (a) and fiber kinematics (b) of arterial adventitia

3.5.6 Contribution of elastin in the mechanical response

A similar sensitivity analysis was performed for the contribution of elastin. The results, plotted in the Fig. 3.18, show that the elastin fraction has a limited impact on the initial slope of the mechanical response, but it changes the stretch at which the collagen recruitment starts, and therefore the time necessary for slope changes.

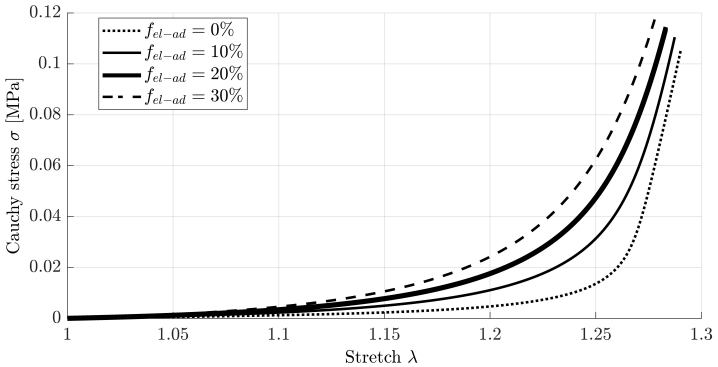

Figure 3.18: The impact of the elastin fraction on macroscopic mechanical response of adventitia.

3.6 Conclusion

The micromechanical modeling was employed in a multi-scale approach to address the non-affine deformation of fibers at large deformation as well as taking into account the anisotropy of collagen and elastin fibers. To the best of our knowledge, the developed constitutive model is the first to address the nonlinearity of the adventitia tissue through the collagen bundle reorientation and the anisotropy through the preferred orientation of the fibers as it has been observed experimentally [22, 82]. The modeling of these microstructural phenomena and access to the microstructural deformation and stresses is crucial for the constitutive model to be capable of accounting for the growth and remodeling, damage and modeling of other pathologies.

The model built on the minimum microstructural information, which can directly be measured from images and predictions of the macroscopic and the microscopic mechanical behavior of adventitia. It is interesting to note that our model well captures the macroscopic mechanical response of the adventitia, with only one fitted parameter, all the others being taken from the microstructural analysis. As the results demonstrate, the model predicts the contribution of collagen and elastin to mechanical load as well as the evolution of micromechanical parameters such as microstructural stresses and microstructural evolution.

In order to have a better understanding of the contribution of the arterial media layer into nonlinearity and anisotropy of the mechanical response of the artery, it is required to build a detailed, microstructural model. This is the aim of the next chapter.

4 | Multi-scale modelling of the arterial media

Contents

Résumé

Dans ce chapitre, nous étendons le modèle micromécanique à la média, qui est la couche intermédiaire dans le tissue artériel. Le modèle cherche à prendre en compte la contribution non linéaire et anisotrope de cette couche dans la réponse mécanique de l'artère. De la même façon que pour le développement du modèle micromécanique de la couche adventice, ce chapitre est consacré à la discussion des étapes nécessaires à la construction du modèle micromécanique de la média

avec des volumes élémentaires représentatifs spécifiques, construits à partir des piles d'images multiphotoniques du tissu. La validation de notre modèle repose sur la simulation d'un essai de traction uniaxiale et sur la comparaison avec les données expérimentales correspondantes.

4.1 Introduction

In this chapter, we extend the micromechanical model to the arterial media layer, to take into account the nonlinear and anisotropic contribution of this layer in the mechanical response of the artery. Similarly to the development of the micromechanical model of the adventitia layer, this chapter is devoted to discussing the steps required to construct the micromechanical model of the media with specific RVEs built from the multiphoton image stacks of the tissue. The validation of our model relies on the simulation of a uniaxial tension test and on the comparison with the corresponding experimental data.

4.2 Micromechanical representation of media

The media layer is made of lamellar units, each unit being made of lamellae, consisting of oblate spheroids containing dense networks of elastin and collagen (see Fig. 4.1), as well as of interlamellar space in between where smooth muscle cells are living (see Fig. 4.2). The mechanical properties of these layers arise from the interplay of their constituents. We here employ the previously introduced theoretical framework (see chapter 2) to propose a micromechanical model of the media, which whose microstructure was described in details in chapter 1.

4.2.1 At the scale of a few hundreds of micrometers

The modeling of the media layer at the scale of a few hundreds of micrometers consists in defining an RVE containing a pile of infinitely long oblate spheroids representing the elastic lamellae and of infinitely long oblate spheroids representing the interlamellar space (see the left RVE of Fig. 4.3). Multiphoton microscopic stacks of images reveal that a characteristic size of the RVE of $l = 100$ μm is a convenient choice for having a sufficiently large number of lamellae to be representative of the media microstructure. Under uniaxial tension, as the load is

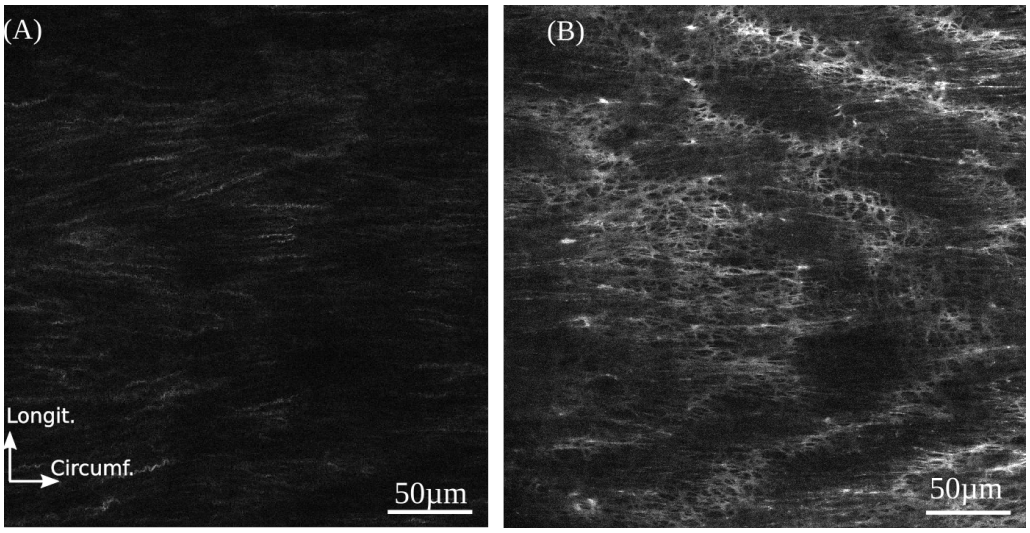

Figure 4.1: Multiphoton microscopic imaging of fibers in the media. (A) collagen fibers; (B) elastin fibers [82].

parallel to the lamellae and interlamellar space, the average response of the RVE is computed from the Voigt bound Eq. (3.3).

4.2.2 At the scale of a few micrometers

Modeling the elastic lamellae

The elastic lamellae are made of dense networks of elastin fibers, and a few percent of collagen fibers type I and III. In the elastic lamellae micromechanical model, these fibers are modeled as infinitely long cylinders embedded in a soft ground substance, which is a suitable candidate for the Mori-Tanaka homogenization scheme (see Fig. 4.3 (C)) [94]. The collagen fiber phase is labeled by the subscript "$c-la$", while the elastin phase is labeled by the subscript "$el-la$", and the matrix phase by "$m-la$". Accordingly, the respective volume fractions of each of these phases read as f_{c-la}, f_{el-la}, and f_{m-la}, with their sum being equal to 1.

Modeling the interlamellar space

The interlamellar space contains SMCs, elastin, and collagen fibers type I and III. Similarly, in the interlamellar space micromechanical model, the collagen and elastin fibers are modeled as infinitely long cylinders embedded in a soft ground

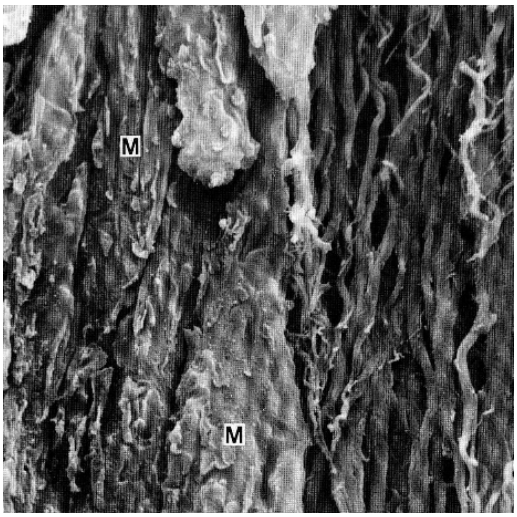

Figure 4.2: Scanning electron micrographs of a tangentially cut surface of the media in the rat aorta. The elastin fibrils and smooth muscle cells (M) covered the surface of the elastic lamellae, magnification $\times 3,500$ [140].

substance containing the SMCs, which is a suitable candidate for the Mori-Tanaka homogenization scheme (see Fig. 4.3 (B)) [94]. The collagen fiber phase is labeled by the subscript "$c-in$", while the elastin phase is labeled by the subscript "$el-in$", and the matrix phase by "$m-in$". Accordingly, the respective volume fractions of each of these phases read as f_{c-in}, f_{el-in}, and f_{m-in}, with their sum being equal to 1.

4.3 Determination of the parameters of the model

4.3.1 Mechanical properties of elementary constituents

The micromechanical models for both lamellae and interlamellar space introduce three distinct elementary constituents, namely: (i) type I and type III collagen fibers, (ii) elastin fibers, and (iii) ground substance matrix. The mechanical parameters for the elementary constituents of the media layer, i.e., of elastin and collagen fibers as well as of the ground substance are the same as those of the adventitia layer model, which are summarized in Table 3.1. In particular, for sake of simplicity, we choose to consider the same mechanical properties for all collagen fibers (i.e. type I and type III). Regarding the mechanical properties of the interlamellar space matrix, the mechanical properties of SMCs have been

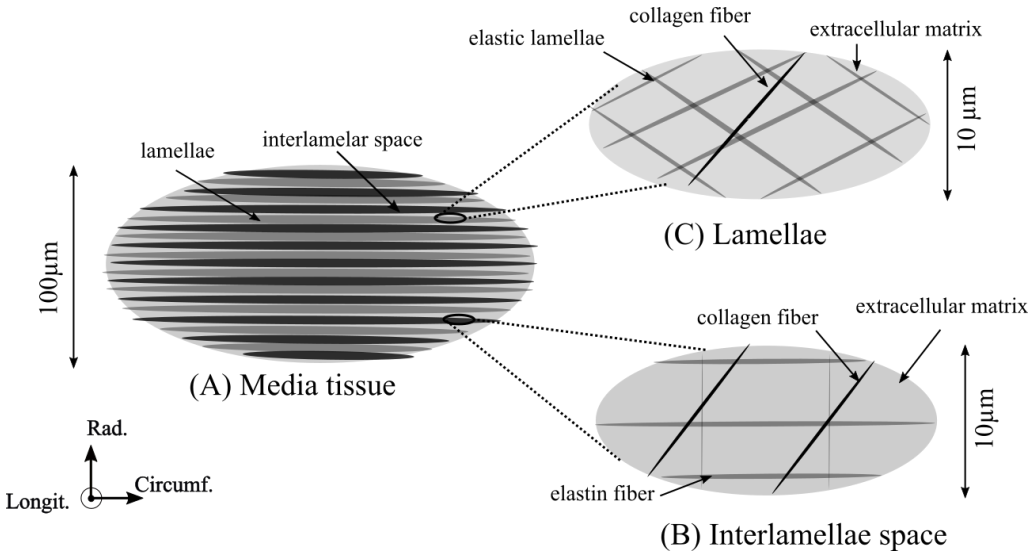

Figure 4.3: Micromechanical RVEs representing the media. (A) RVE representing the tissue scale; (B) RVE representing the interlamellar space; (C) RVE representing the lamellae.

reviewed in Chapter 1, and a Young's modulus of 50 kPa was chosen for the ground substance of the interlamellar space.

4.3.2 Volume fraction of elementary constituents

Amount of elastin fibers in the media

The multiphoton stacks of medial tissue from rabbit carotid arteries taken by Witold Krasny [82] were analyzed using the same procedure as for the adventitia, namely: first, ImageJ allows to separate the two channels of the second harmonic generation (collagen signal) and autofluorescence (displaying mainly the elastin fibers, but also few collagen fibers). Then, the Otsu thresholding technique [103] allows to access the fiber fraction by means of conversion to binary images. As a result the elastin fibers volume fraction amounts to 25% as estimated by the average over the nine samples. This is in good agreement with an medial elastin volume fraction of 29% as measured in rat aorta by [100]. Our estimated value is also in good agreement with the amount of elastin measured in small animals arteries, as reported in Table 4.1. Bigger species, like porcs, sheeps, or even humans, have a larger amount of elastin. Besides, [100] stated that approximately

71% of the total medial elastin belongs to the lamellae. Thus, if we split the total volume fraction of medial elastin between 50% lamellae and 50% interlamellar space such that 71% of elastin is present in the lamellae, we can compute an elastin volume fraction in the lamellae of around 35% and in the interlamellar space of around 15%.

Specimen	Imaging method	Volume fraction	Reference
Human abdominal aorta	photomicrograph	40% to 60%	[136]
Sheep carotid	photomicrograph	40% to 50%	[27]
Rat subrenal aorta	photomicrograph	35% to 45%	[80]
Porcine aorta	photomicrograph	30% to 50%	[135]
Wistar rats aorta	photomicrograph	20% to 25%	[56]

Table 4.1: Review of the volume fraction of elastin fibers in the media

Amount of collagen fibers in the media

The volume fraction of medial collagen fibers is also evaluated using the second harmonic generation channel through ImageJ followed by the Otsu thresholding technique [103]. As a result, the fraction of collagen fiber in the media amounts to around 25% as given by the average over the nine samples tested by Witold Krasny [82], which falls well in the range of all other measures reported in the literature, as summarized in Table 4.2.

It has been observed experimentally that the collagen fibers are distributed between the lamellae and the interlamellar space [100], but the exact proportions are not reported. For simplicity, we split the total volume fraction of medial collagen between 50% in the lamellae and 50% in the interlamellar space, such that the fraction of collagen fiber in the lamellae and interlamellar space becomes equal to 25%.

Specimen	Imaging method	Volume fraction	Reference
Sheep carotid	photomicrograph	40% to 50%	[27]
Wistar rats aorta	photomicrograph	20% to 25%	[56]
Porcine aorta	photomicrograph	15% to 22%	[135]
Human abdominal aorta	photomicrograph	12% to 20%	[136]

Table 4.2: Review of the volume fraction of collagen fibers type I and III in the media

Amount of SMCs in the media

Although this fraction is not needed in our model, we here report values for the volume fraction of SMCs in the media, for a future extension of the model, explicitely accounting for the SMCs. The volume fraction of SMCs has been assessed by a stereological method on histological sections of the medial porcine abdominal aorta by [134]. They reported a volume fraction of around 65% for the SMCs. Other studies, as summarized in Table 4.3, report smaller fractions of SMC for other species and arteries.

Specimen	Imaging method	Volume fraction	Reference
Porcine abdominal aorta	photomicrograph	65%	[134]
Rat subrenal aorta	photomicrograph	50% to 55%	[80]
Human abdominal aorta	photomicrograph	40% to 45%	[136]

Table 4.3: Review of the volume fraction of SMCs in the media

4.3.3 Orientation of the different fiber networks

In the medial model, we also chose to model both fiber networks (collagen and media) as infinitely-long cylindrical inclusions, with orientation characterized by the two Eulerian angles θ and ϕ, i.e. by the classical spherical coordinates as defined by Fig. 4.4 and Eq. (2.48) in Chapter 2.

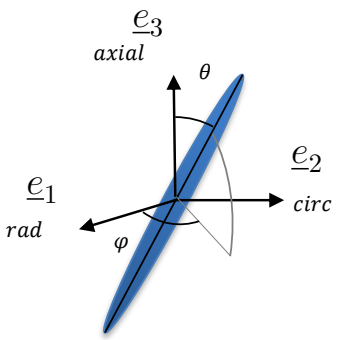

Figure 4.4: Orientation of a fiber in the arterial wall. θ represents the fiber inclination with respect to the axial direction of artery, and ϕ its direction in the radial-circumferential plane.

Orientation of the elastin fibers

Different contributions [100, 18, 157] showed that the elastin fibers in the media are mainly oriented along the circumferential direction both in the lamellae and the interlamellar space, i.e. $\theta_{el-med} = 90°$. A small fraction of elastin (5%) was assigned a longitudinal orientation, $\theta_{el-med} = 0°$ to represent the interconnection of the elastin network. This circumferential orientation was also found when analyzing the multiphoton stacks of Witold Krasny [82]. Besides, some portion of the elastin fibers are tilted in the radial-circumferential plane, with an orientation parallel to the tilting of the SMC, i.e. $\phi_{el-in} = \phi_{el-la} = 70°$ [100], while some elastin fibers networks display no radial tilting, i.e. $\phi_{el-in} = \phi_{el-la} = 90°$. The existence of truss fibers in the interlamellar space motivates us for the introduction of a small portion (5%) of elastin fibers with a purely radial orientation, i.e. $\phi_{el-in} = 0$ [100].

Orientation of the collagen fibers

The orientation of collagen fibers was analyzed using OrientationJ, a series of ImageJ plugins for directional image analysis [107, 114]. We extracted a main orientation for medial collagen fibers $\theta_{c-med} = 85°$, which is in good agreement with the results of [100, 22]. According to the literature [100], these collagen fibers have an inclination in the radial-circumferential plane but no study reported this angle. Thus, the inclination of collagen fibers in the radial-circumferential plane of the media ϕ_{c-med} is chosen as a free parameter. We consider that the collagen fibers have the same initial orientation in the lamellar and interlamellar space.

A summary of model parameters and constants is given in table 4.4.

Parameters		Collagen	Ground substance
mechanical constant		$E_c = 250$ MPa	$E_{m-la} = 0.01$ & $E_{m-in} = 0.05$ MPa
		$\nu_b = 0.34$	$\nu_m = 0.34$
volume fraction	Lamellae	$f_{c-la} = 25\%$	$f_{m-la} = 1 - \sum_i f_i$
	Interlamellar space	$f_{c-in} = 25\%$	$f_{m-in} = 1 - \sum_i f_i$
orientation	Lamellae	$\theta_{c-med} = 85°$	NA
		ϕ_{c-med} = Free parameter	NA
	Interlamellar space	$\theta_{c-med} = 85°$	NA
		ϕ_{c-med} = Free parameter	NA

Parameters		Elastin 1	Elastin 2	Elastin 3
mechanical constant		$E_{el1} = 1$ MPa	$E_{el2} = 1$ MPa	$E_{el3} = 1$ MPa
		$\nu_{el1} = 0.34$	$\nu_{el2} = 0.34$	$\nu_{el3} = 0.34$
volume fraction	Lamellae	NA	$f_{el2-la} = 30\%$	$f_{el3-la} = 5\%$
	Interlamellar space	$f_{el1-in} = 5\%$	$f_{el2-in} = 5\%$	$f_{el3-in} = 5\%$
orientation	Lamellae	NA	$\theta_{el2-med} = 90°$	$\theta_{el3-med} = 0°$
		NA	$\phi_{el2-la} = 70°$	$\phi_{el3-la} = 90°$
	Interlamellar space	$\theta_{el1-med} = 90°$	$\theta_{el2-med} = 90°$	$\theta_{el3-med} = 0°$
		$\phi_{el1-in} = 0°$	$\phi_{el2-in} = 70°$	$\phi_{el3-in} = 90°$

Table 4.4: Summary of the medial model parameters and constants.

4.4 Results

4.4.1 Tensile test on the arterial media

Uniaxial tensions were simulated with the micromechanical model of the media to compare the predicted mechanical response with the experimental results reported for human coronary arteries [63] in the circumferential and longitudinal directions. A genetic algorithm was employed to determine the collagen inclination ϕ_{c-med} so as to fit simultaneously the circumferential and longitudinal curves. Finally, an orientation of $\phi_{c-med} = 53°$ for human coronary artery leads to the best agreement between model predictions and experimental results (see Fig. 4.5 (a)). Although the model could predict correctly the mechanical response of the media in the circumferential direction, the prediction of the mechanical response in longitudinal direction remains linear. As the microstructure of the specimen is not reported for the human coronary artery, further investigation was performed on the model to have a better estimation of the mechanical response in both circumferential and longitudinal directions. This investigation shows that the collagen dispersion toward longitudinal direction provides a nonlinear mechanical response in the longitudinal direction. Finally, the collagen fiber dispersion with equal volume

fraction (12.5%) in $\theta_{c-med} = 85°$ and $\theta_{c-med} = 70°$ leads to a better prediction of the mechanical response of the human coronary artery (see Fig. 4.5 (b)). Note that even for a sample of the rabbit carotid artery was observed dispersion and inclination of collagen fibers around the main orientation ($\theta_{c-med} = 80°$).

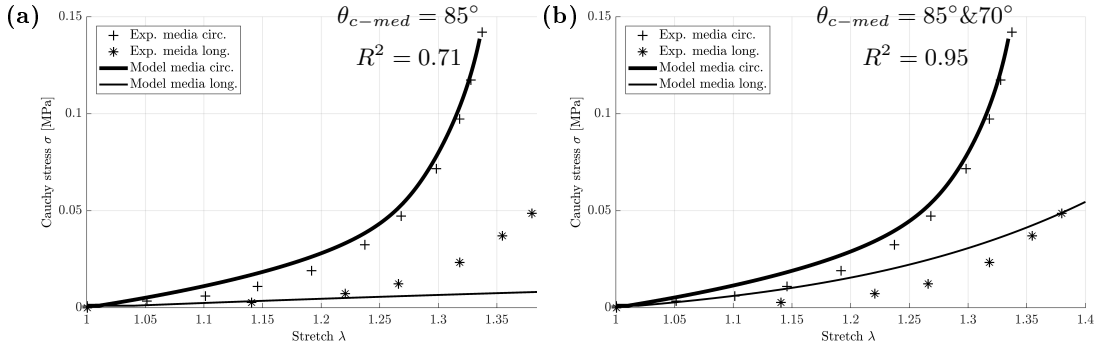

Figure 4.5: Macroscopic mechanical response of the media human coronary artery according to [63], (a) $\theta_{c-med} = 85°$. (b) $\theta_{c-med} = 85°\&70°$.

Furthermore, the evolution of fiber angles was predicted by the model during uniaxial tension, both in the circumferential and longitudinal directions (see Fig. 4.6). The results are in good qualitative agreement with the experimental ones reported by Krasny [82] and Chow [22]: the medial fiber networks undergo a very limited reorientation.

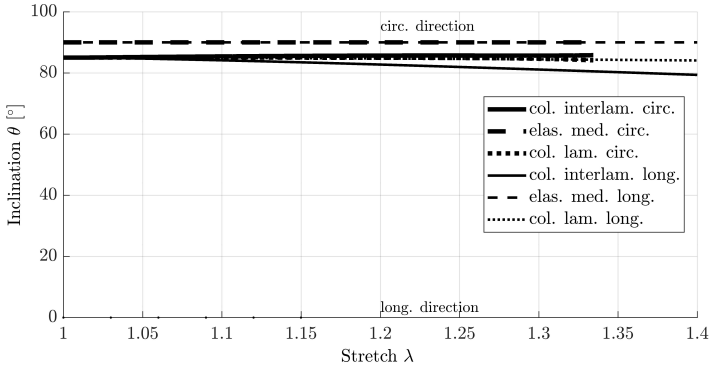

Figure 4.6: Evolution of fiber angles under uniaxial tension in the media.

4.4.2 Tensile test on artery

Finally, the global response of the arterial wall was computed by averaging across the whole thickness, pooling together the adventitia and the media to compare the

results of the model with the experiment performed on the whole carotid artery [82]. The overall stress of the artery is obtained from Eq. (3.3) by assuming the same strain rate in the adventitia and media layers (according to the arrangement of the layers with respect to the load directions).

The constants of the micromechanical model of the media and adventitia are the ones reported for the previous validations. Nevertheless, the free parameter of the adventitia model, i.e. the global orientation of collagen bundles θ_{b-ad} and the free parameter of the media model ϕ_{c-med} were determined by fitting the predicted response to the experimental response using a genetic algorithm. The inclination of collagen fibers in the radial-circumferential plane of the media for all the carotid artery samples is obtained as $\phi_{c-med} = 50°$. The global orientation of adventitial collagen bundles θ_{b-ad}, obtained after calibration, is reported in Table 4.5 for each carotid artery sample. The results also show the effect of preconditioning, which also observed from experimental tests [82] as discussed in Chapter 3. Good agreements are found between the modeled response and the experiments, both in terms of macroscopic stress-stretch behavior and in terms of rotations of microstructural components. Results are shown in Fig. 4.7.

Sample	Preconditioning	θ_{b-ad}	R^2
Sample 1	circ	30	0.82
	long	67.5	
Sample 2	circ	37	0.87
	long	66	
Sample 3	circ	31.5	0.75
	long	71	
Sample 4	circ	29.5	0.78
	long	68.5	

Table 4.5: Obtained model parameters after calibration for each carotid artery sample.

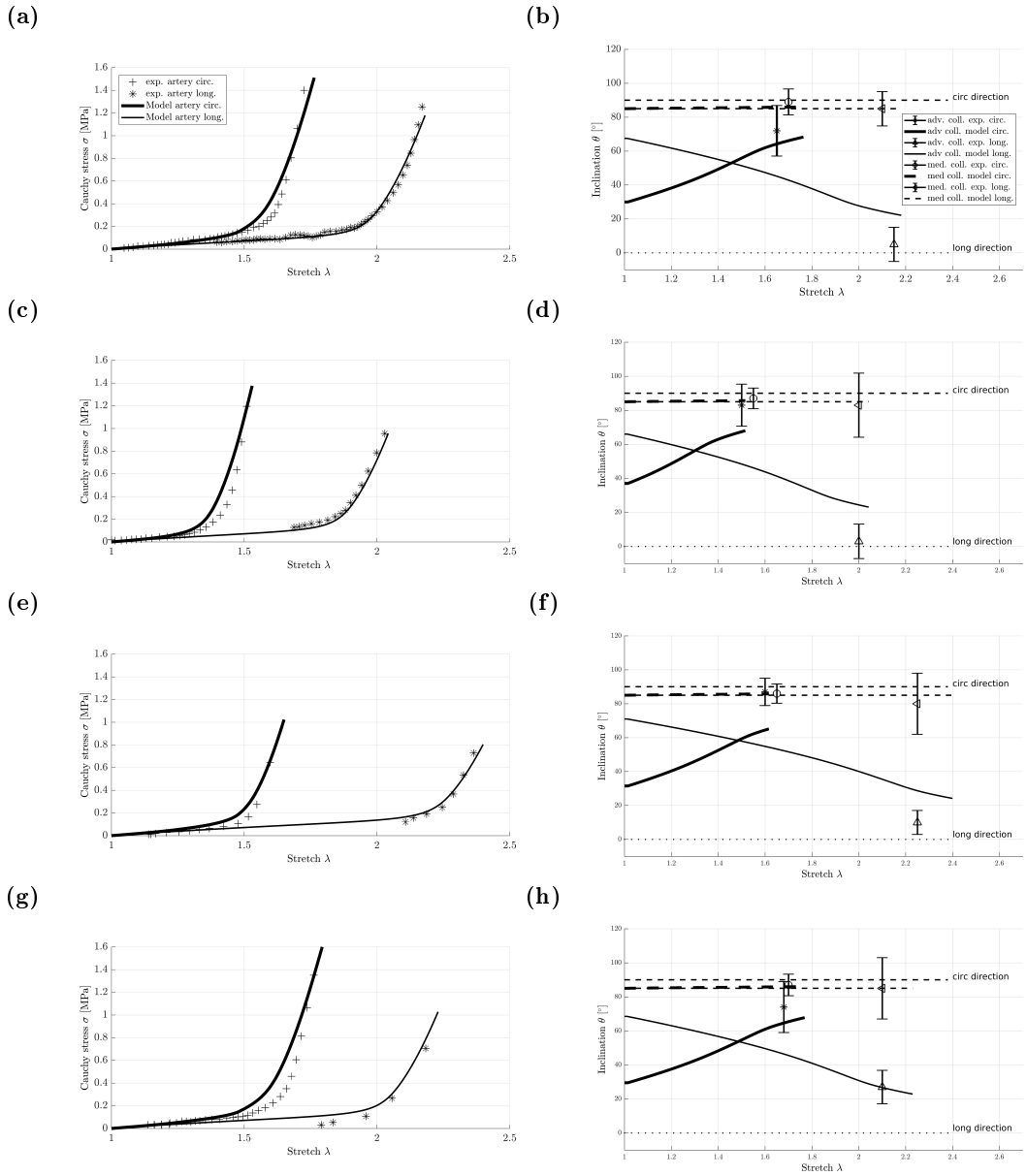

Figure 4.7: Comparison of the modeled mechanical response and fiber kinematics with the experiments [82] for different carotid artery samples. $\phi_{c-med} = 50°$ for all samples.

4.5 Discussion

The micromechanical approach was extended to model as well the medial layer of artery. For the sake of simplicity two RVEs represent the media layer namely: elastic lamellae and interlamellar space. The minimum microstructural information, which is necessary to achieve reliable predictions of macroscopic mechanical behavior was taken into account to establish the RVEs. Then, the media layer was modeled as a lamellar structure of these two units, which has been observed experimentally [100]. The RVE of elastic lamellae consists of elastin and collagen fibers and interlamellar space's RVE consists of elastin and collagen fibers, and smooth muscle cells (SMCs). In the RVE of interlamellar space, SMCs was represented as a soft ground substance, since modeling the SMCs as inclusion (see primary media's RVEs in Fig. 4.8) have shown not to have an important impact on the mechanical response of the medial layer due to its low stiffness compared to the other constituents. Furthermore, in the primary micromechanical media's RVEs, lamellae modeled with two scales; at the upper scale, elastic lamellae and collagen fibers embedded in a soft matrix, and the lower scale was represented the dense networks of elastin fibers in the elastic lamellae (see Fig. 4.8). These arrangements had almost doubled the parameters but could not improve the prediction of the model (see Fig. 4.9, $R^2 = 0.88$).

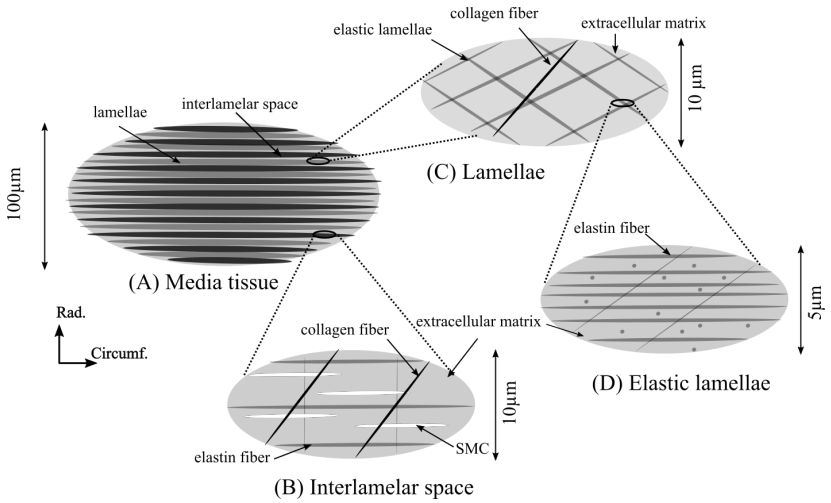

Figure 4.8: Primary micromechanical RVEs representing the media. (A) RVE representing the tissue scale; (B) RVE representing the interlamellar space; (C) RVE representing the lamellae; (D) RVE representing the elastic lamellae.

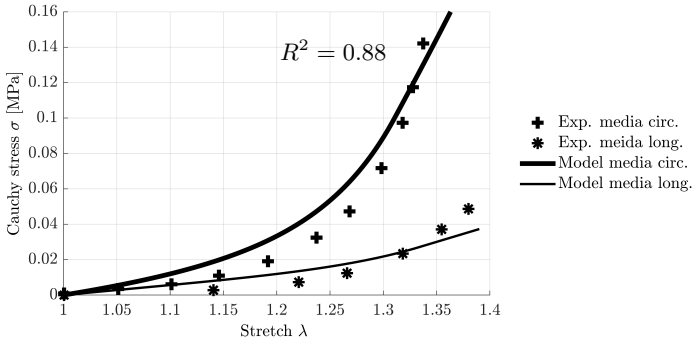

Figure 4.9: Primary model macroscopic mechanical response of the media human coronary artery according to [63].

The results show that the model is capable of capturing the macroscale mechanical response and the microscale fiber kinematics for the medial layer. The fibers in the medial layer under load do not reorient largely as in the adventitial layer (compare Fig. 4.6 to Fig. 3.8 (b) from Chapter 3 for the adventitial fiber reorientations), which is also in good agreement with experimental observations [82, 22]. This fibers' interaction has been correctly predicted by the Mori-Tanaka assumption [94], although Mori-Tanaka scheme only considers the modeling of fiber-matrix interaction, in which fibers can only feel each other through the matrix rather than the direct interaction between the network of fibers. Furthermore, considering all these interactions in a complex biological tissue through the implementation of finite element is computationally expensive [76].

Although for the sake of simplicity we consider one family of collagen fibers, results show the fiber dispersion can improve the prediction of the mechanical behavior of the medial layer (compare Fig. 4.5(a) and Fig. 4.5(b)). Note that we did not have access to the microstructural information of the tested medial samples on the human coronary artery by [63], and microstructural information was obtained from the rabbit carotid artery images. The mechanical responses of the whole artery obtained from the Voigt bound estimation Eq. (3.3), this is only valid when the load direction is parallel to the direction of the layers. In order to apply more complex load conditions such as an inflation test on the artery, the implementation of the finite element method is necessary to account for the interaction of these RVEs.

Among the parameters introduced in the medial model, the different volume

fractions vary in wide ranges, depending on the species or on the considered organ. We therefore chose to perform a sensitivity analysis, so as to understand how these volume fractions impact the overall medial mechanical response. In this sensitivity analysis, we also include the inclination parameter which was determined by a genetic algorithm. For each parameter, we here show its impact on the uniaxial circumferential response of the media, while maintaining all other parameters constant and equal to the value indicated above in Table 4.4.

The investigation reveals that the most influential parameter is the orientation of the collagen fibers ϕ_{c-med}: increasing the angle between the fibers and the load directions (i.e. in circumferential tension $90-\phi_{c-med}$) leads to increasing the time it takes to stiffen the material, since it takes more time for the fiber to reorient and to align with the load direction (see Fig. 4.10(a)). In contrast to ϕ_{c-med}, the angle θ_{c-med} does not have an impact on the results as collagen fibers are aligned almost circumferentially and therefore are already aligned with the load direction (see Fig. 4.10(b)).

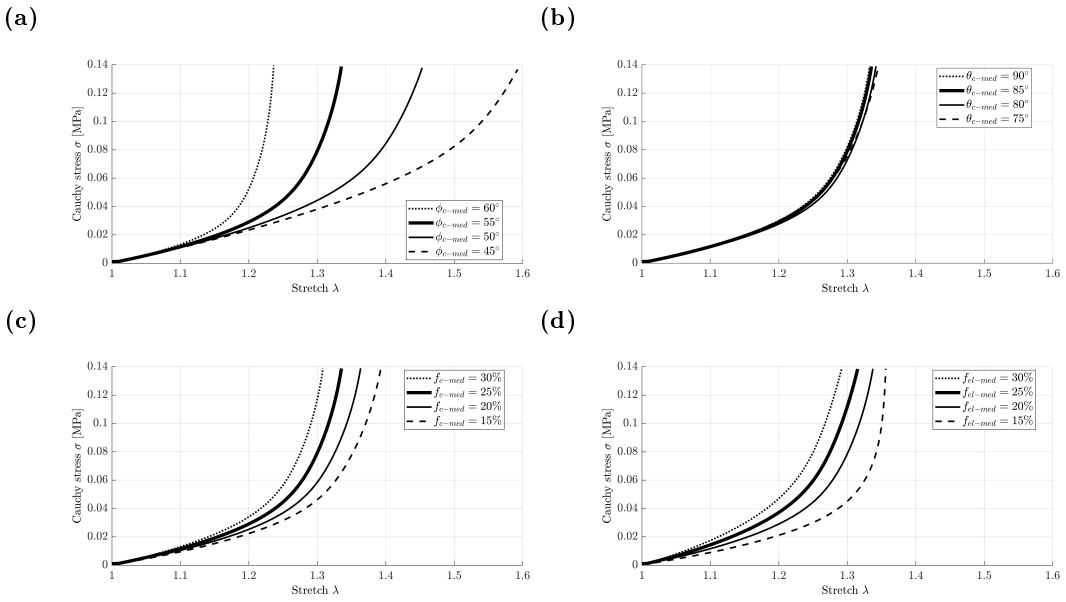

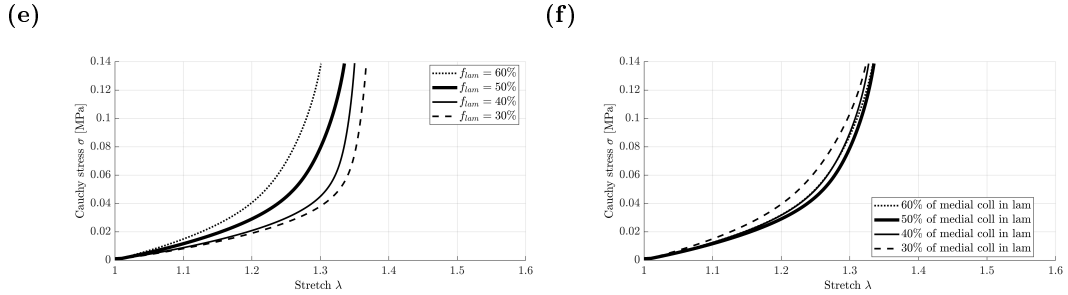

Figure 4.10: The impact of different parameters of the media model on the circumferential mechanical response (a) out of axial-circumferential plane inclination angle of medial collagen ϕ_{c-med} (b) in axial-circumferential plane inclination angle of the medial collagen θ_{c-med} (c) fraction of collagen in the media f_{c-med} (d) fraction of elastin in the media f_{el-med} (e) fraction of lamellae in the media f_{lam} (f) different proportions of collagen fraction in the medial lamellae.

Increasing the volume fraction of collagen and elastin fibers lead to decreasing the time it takes to stiffen the material. In this condition, we have less volume fraction of ground substance and more interaction between bundles which leads to faster reorientation with the load direction (see Fig. 4.10(c) & (d)). The other parameter whose value exhibited variations in the literature is the proportion of the lamellae and interlamellar space in the media. As lamellae contains higher fraction of elastin fibers which make it stiffer as compared to the interlamellar space, these elastin fibers as well resist against reorientation of collagen fibers. Increasing the fraction of lamellae leads to decreasing the time it takes to stiffen the material as well as decreasing the non-linear behavior of the material (see Fig. 4.10(e)). Further investigations show increasing or decreasing the volume fraction of collagen fibers in the lamellae dose not impact the mechanical responses of the model (see Fig. 4.10(f)).

4.6 Conclusion

In this chapter, the micromechanical approach was extended to model the medial layer. The developed hypoelastic constitutive model in the framework of continuum micromechanics correctly predicted the nonlinear and anisotropic mechanical responses of arteries at the elastic regime. The multiscale layer-specific

model includes directly phenomena occurring at the microscopic scale, such as fibers interaction through the matrix, collagen fiber recruitment, and non-affine fiber rotations, and takes into account universal patterns of the hierarchical organization of arteries at different scales.

The results illustrate the capability of the model to capture the macroscopic mechanical response of the tissue as well as micromechanical evolution. We hope that this microstructure-based model will bring improvements in the prediction of damage and strength of arterial tissue, since failure of the different constituents can be predicted and upscaled to predict the rupture of the tissue.

5 | Layer-specific structural model of artery: finite element implementation

Contents

Résumé

Dans ce chapitre, un code éléments finis fait maison a été écrit en tenant compte du modèle constitutif artériel multi-échelle pour la structure spécifique de l'artère

en couches, à savoir : lamelles, espace interlamellaire et adventice. En raison de la nature incrémentale du modèle constitutif matériel, une formulation lagrangienne actualisée des éléments finis a été utilisée pour prendre en compte les RVE aux points intégraux de chaque élément et mettre à jour la morphologie de la microstructure à chaque incrément. Après validation du modèle par rapport aux solutions semi-analytiques, le modèle d'éléments finis est utilisé pour simuler un test d'inflation artérielle. La pression interne en fonction du rayon interne a été calculée pendant la simulation et les résultats ont été comparés aux résultats expérimentaux de l'artère rénale de la souris [35]. De plus, la distribution des contraintes et l'orientation des fibres ont été étudiées sur la paroi artérielle.

5.1 Introduction

In this chapter, a home-made finite element code was written by taking into account the multi-scale arterial constitutive model for the layer-specific structure of the artery; namely: lamellae, interlamellar space, and adventitia. Due to the incremental nature of the material constitutive model, an updated Lagrangian finite element formulation was employed to take in to account the RVEs at integral points of each element and update the morphology of the microstructure at each increment. After validating the model against the semi-analytical solutions, the finite element model is used to simulate an arterial inflation test. The internal pressure versus inner radius was calculated during the simulation and the results were compared with the experimental results of the mouse renal artery [35]. Furthermore, the distribution of stress and fiber orientations were investigated across the arterial wall.

5.2 Position of the problem

We consider an arterial segment with a simplified geometry of a hollow cylinder with length L , internal radius R_i, and thickness H, and made of two concentric layers, namely the adventitia as the outer layer and the media as the inner one (see Fig. 5.1). The intima is not modeled due to its negligible role in the arterial mechanics. This initial configuration is considered as the unloaded configuration and the reference for stresses and strains is chosen on this configuration. The arterial segment is subjected to a pressure field P_{im} on the inner surface $\partial\Omega^i$,

while the outer surface $\partial\Omega^o$ is let free of traction forces. Finally, a zero velocity is imposed on the two crosssectional surfaces $\partial\Omega^{end}$. The hypoelastic constitutive models developed in chapters 3 and 4 are chosen for modeling the response of the adventitial and medial layers respectively. This problem can be summarized by the following set of equations:

$$\underline{\mathrm{div}}\,(\boldsymbol{\Sigma}(\underline{X},t)) = 0 \qquad \forall \underline{X} \in \Omega, \tag{5.1}$$

$$\boldsymbol{\Sigma}(\underline{X},t)\cdot\underline{n}(\underline{X},t) = P_{im}(\underline{X},t)\,\underline{n}(\underline{X},t) \qquad \forall \underline{X} \in \partial\Omega^i, \tag{5.2}$$

$$\boldsymbol{\Sigma}(\underline{X},t)\cdot\underline{n}(\underline{X},t) = \underline{0} \qquad \forall \underline{X} \in \partial\Omega^o, \tag{5.3}$$

$$\underline{V}(\underline{X},t)\cdot\underline{e}_z = \underline{V}(\underline{X},t)\cdot\underline{e}_\theta = \underline{0} \qquad \forall \underline{X} \in \partial\Omega^{end}, \tag{5.4}$$

$$\dot{\boldsymbol{\Sigma}}(\underline{X},t) = \mathbb{C}(\underline{X},t) : \boldsymbol{D}(\underline{X},t) \qquad \forall \underline{X} \in \Omega, \tag{5.5}$$

whereby $\boldsymbol{\Sigma}$, $\boldsymbol{D}$, $\underline{V}$, $\underline{X}$ and $\underline{n}$ are respectively the macroscopic Cauchy stress tensor, the macroscopic Eulerian strain rate, the macroscopic velocity vector, the macroscopic location vector, and the outer unit normal vector, all of them being evaluated at time t and location $\underline{X}$; Ω, $\partial\Omega^i$, $\partial\Omega^o$, and $\partial\Omega^{end}$ are respectively the cylinder volume, inner and outer surfaces, and crosssectional surfaces. Finally, the macroscopic field of hypoelastic stiffness is defined as:

$$\mathbb{C}(\underline{X},t) = \begin{cases} \mathbb{C}_{adv} & \text{if } \underline{X} \in \Omega_{adv} \\ \mathbb{C}_{lam} & \text{if } \underline{X} \in \Omega_{lam} \\ \mathbb{C}_{in} & \text{if } \underline{X} \in \Omega_{in} \end{cases}$$

with subscripts adv, lam, and in denoting respectively the adventitia, the lamellar space, and the interlamellar space.

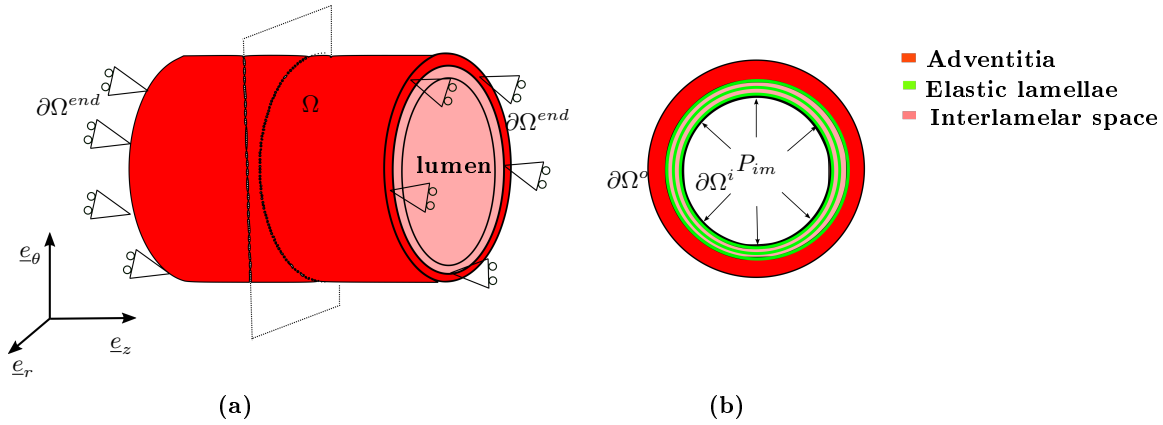

Figure 5.1: (a) The geometry of the problem. (b) Crosssection of cylinder.

5.3 Numerical strategy

5.3.1 Weak formulation

The inflation problem is solved by a numerical scheme, which requires rewriting the previously described problem in a weak formulation. To this aim, the equilibrium equation (5.1) is multiplied by a virtual velocity field $\underline{\tilde{V}}$ and integrated over the arterial volume Ω. Then the divergence theorem is used, and the different boundary conditions need to be accounted for. In more details, one gets:

$$\begin{aligned}\int_\Omega \boldsymbol{\Sigma} : \tilde{\boldsymbol{D}}\, d\Omega &= \int_{\partial\Omega} (\boldsymbol{\Sigma}\cdot\underline{n})\cdot\underline{\tilde{V}}\, dS,\\ &= \int_{\partial\Omega^i} (\boldsymbol{\Sigma}\cdot\underline{n})\cdot\underline{\tilde{V}}\, dS + \int_{\partial\Omega^o} (\boldsymbol{\Sigma}\cdot\underline{n})\cdot\underline{\tilde{V}}\, dS + \int_{\partial\Omega^{end}} (\boldsymbol{\Sigma}\cdot\underline{n})\cdot\underline{\tilde{V}}\, dS.\end{aligned} \tag{5.6}$$

The second integral of the right-hand side is zero according to the boundary condition (5.3). The virtual velocity field $\underline{\tilde{V}}$ belongs to the set of continuous and continuously differentiable field on Ω, which are kinematically admissible with the problem defined by Eqs. (5.1) to (5.5). Accordingly, the third equation of the right-hand side is also equal to zero. Therefore, Eq. (5.6) simplifies as:

$$\begin{aligned}&\int_\Omega \boldsymbol{\Sigma} : \tilde{\boldsymbol{D}}\, d\Omega = \int_{\partial\Omega^i} (P_{im}\,\underline{n})\cdot\underline{\tilde{V}}\, dS,\\ &\underline{\tilde{V}}(\underline{X},t)\cdot\underline{e}_z = \underline{\tilde{V}}(\underline{X},t)\cdot\underline{e}_\theta = \underline{0} \qquad\qquad \forall \underline{X}\in\partial\Omega^{end}.\end{aligned} \tag{5.7}$$

5.3.2 Temporal discretization

Due to the non-linear nature of the problem (resulting from the hypoelastic constitutive formulation), a temporal discretization is introduced; all variables are evaluated at a series of time instants t represented by a constant time interval dt. As in the previous chapters, an explicit forward Euler scheme is used, i.e. any time derivative is evaluated as follows:

$$\dot{a}^t = \frac{a^{t+dt} - a^t}{dt} \overset{\text{def}}{=} \Delta a^t. \tag{5.8}$$

Leading, for the Cauchy stress field, to:

$$\boldsymbol{\Sigma}^{t+dt} = \boldsymbol{\Sigma}^t + \dot{\boldsymbol{\Sigma}} dt = \boldsymbol{\Sigma}^t + \mathbb{C}^t : \boldsymbol{D}^t dt, \tag{5.9}$$

where equation (5.5) has been accounted for.

Considering that all mechanical configurations are known up to time t, one aims at computing the mechanical equilibrium at time $t + dt$. Incorporating Eq. (5.9) into Eq. (5.7), written for the configuration at time $t + dt$, leads to:

$$\begin{aligned} \int_{\Omega^{t+dt}} \boldsymbol{D}^t : \mathbb{C}^t : \tilde{\boldsymbol{D}}\, d\Omega = & \int_{\partial\Omega^{i,t+dt}} \left(P^t_{im} \underline{n}^{t+dt} \right) \cdot \underline{\tilde{V}}\, dS \\ & + \int_{\partial\Omega^{i,t+dt}} \left(\Delta P^t_{im} \underline{n}^{t+dt} \right) \cdot \underline{\tilde{V}}\, dS - \int_{\Omega^{t+dt}} \boldsymbol{\Sigma}^t : \tilde{\boldsymbol{D}}\, d\Omega, \\ \underline{\tilde{V}}(\underline{X}, t+dt) \cdot \underline{e}_z = \underline{\tilde{V}}(\underline{X}, t+dt) \cdot \underline{e}_\theta = \underline{0} & \qquad \forall \underline{X} \in \partial\Omega^{end}, \end{aligned} \tag{5.10}$$

whereby the pressure field P_{im} has been discretized according to Eq. (5.8).

5.3.3 Simplifying assumptions for solving the problem

The weak formulation Eq. (5.10) is written on the configuration at time $t + dt$, which remains unknown, and on which there is no certainty that the stress at time t is in equilibrium with the internal pressure at time t (i.e. that the first and last terms on the right-hand side cancel). Also, the stiffness of the tissue and the hidden concentration tensors are evolving with the load application. To overcome these difficulties, extra assumptions need to be made: (i) the stiffness remains constant during the load increment, (ii) the geometry change during the interval dt is small enough to assume that the stress field and the applied pressure at time t are in equilibrium on the configuration at time $t + dt$, and (iii) the update of the tissue stiffness does not induce a further imbalance. In other words, we assume that the loading is discretized in sufficiently small steps, and therefore,

the geometry change between two successive configurations can be neglected and iterations between local enforcement of the constitutive relation and the global equilibrium can be neglected. As a result, the equilibrium reduces to:

$$\begin{aligned} &\int_{\Omega^t} \boldsymbol{D}^t : \mathbb{C}^t : \tilde{\boldsymbol{D}}\, d\Omega = \int_{\partial\Omega^{i,t}} \left(\Delta P^t_{im} \underline{n}^t\right) \cdot \underline{\tilde{V}}\, dS, \\ &\underline{\tilde{V}}(\underline{X}, t) \cdot \underline{e}_z = \underline{\tilde{V}}(\underline{X}, t) \cdot \underline{e}_\theta = \underline{0} \qquad\qquad \forall \underline{X} \in \partial\Omega^{end}. \end{aligned} \tag{5.11}$$

5.3.4 Finite element discretization

In order to solve the spatial integral over the volume of the geometry at each time increment, a finite element approach is used. As it is shown in Fig. 5.1, both the geometry and the loading applied on the artery display a cylindrical symmetry.

This reduces the problem to an axisymmetric problem. The study is restricted to the surface corresponding to the intersection of the hollow cylinder with the plane $(\underline{e}_r, \underline{e}_z)$ defined in cylindrical coordinate system by a constant θ angle (see Fig. 5.2). The equilibrium equation (5.1) in cylindrical coordinates, reads as:

$$\begin{aligned} &\frac{\partial \Sigma_{rr}}{\partial r} + \frac{\partial \Sigma_{rz}}{\partial z} + \frac{\Sigma_{rr} - \Sigma_{\theta\theta}}{r} = 0 \\ &\frac{\partial \Sigma_{rz}}{\partial r} + \frac{\partial \Sigma_{zz}}{\partial z} + \frac{\Sigma_{rz}}{r} = 0, \end{aligned} \tag{5.12}$$

and the boundary conditions reduce to:

$$\begin{aligned} &\boldsymbol{\Sigma} \cdot \underline{n} = \underline{P}_{im} \qquad\qquad \text{on } \partial\Omega^i, \\ &\boldsymbol{\Sigma} \cdot \underline{n} = \underline{0} \qquad\qquad \text{on } \partial\Omega^o, \\ &\underline{\tilde{V}}(\underline{X}, t) \cdot \underline{e}_z = \underline{0} \qquad\qquad \forall \underline{X} \in \partial\Omega^{end}. \end{aligned} \tag{5.13}$$

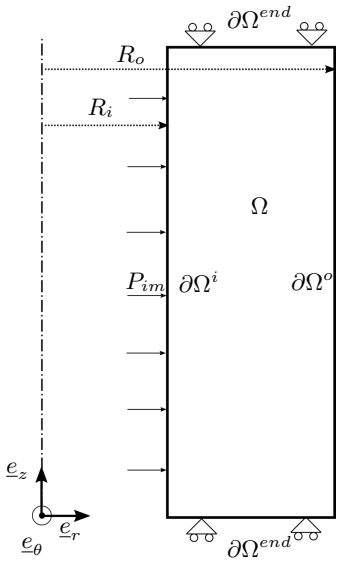

Figure 5.2: Imposed boundary condition on the geometry accounting for symmetry conditions.

5.3.5 Algorithm for constitutive model implementing

The homogenization method discussed in detail in Chapter 2 was employed to compute homogenized stiffness of material through Eq. (2.52) for each time increment. Due to the incremental nature of the hypoelastic local constitutive model, the finite element formulation was simplified in an incremental form, where the deformation and evolution of the microstructure can be approximated to be linear at each increment. The homogenized fourth order stiffness matrix $\mathbb{C}$ at each time increment was used to compute the element stiffness matrix. Furthermore, the computed spin tensor at each increment was utilized to update the microstructure evolution θ and ϕ. A summary of the numerical scheme for the finite element implementation is illustrated in Table 5.1.

1. Given macroscopic incremental pressure ΔP_{im}^t
2. Initialize $\boldsymbol{\Sigma}^t$, $\boldsymbol{F}^t$, and the homogenized behavior of the material $\mathbb{C}_{hom}^t$ at time t from Eq. (2.52)
3.Perform an iteration loop to compute deformation gradient $\boldsymbol{F}^{t+dt}$ and Cauchy stress $\boldsymbol{\Sigma}^{t+dt}$
   a) For every element $i = 1$ to n
   b) Compute the coordinates of nodes
   c) Initialize the stiffness matrices $\boldsymbol{K}$ and $\boldsymbol{K}_e$ and right hand sides $\underline{b}$ and $\underline{b}_e$ to zero
      (i) Loop over the Gauss points
      (ii) Compute the Gauss weights w_i
      (iii) Compute the shape functions
      (iv) Compute the Jacobian
      (v) Evaluate the derivatives of the shape functions
      with respect to the global coordinates
      (vi) Compute the stiffness matrix $\boldsymbol{K}_e$
      and right hand side $\underline{b}_e$ for the element
   d) Assemble into the global stifness matrix $\boldsymbol{K}$ and right hand side $\underline{b}$ and solve for
      $\boldsymbol{K}\underline{V} = \underline{b}$
   e) Compute deformation gradient $\boldsymbol{F}^{t+dt}$ and Cauchy stress $\boldsymbol{\Sigma}^{t+dt}$
4. Update the homogenized behavior of the material $\mathbb{C}_{hom}^{t+dt}$
5. Update the microstructure morphology θ and ϕ using spin tensor $\boldsymbol{\omega}$
6. Update the geometry based on deformation gradient

Table 5.1: Numerical algorithm for finite element implementation.

5.4 FEM solver validation test cases

5.4.1 Validation with a commercial FEM code: Linear elasticity

As a first step, we considered a linear elastic material with a Young's modulus $E = 1$ MPa and a Poisson's ratio $\nu = 0.34$ for the arterial wall. The cylinder has an inner radius $R_i = 0.275$ mm and a thickness $H = 0.1$ mm. 20 quadrilateral elements are taken into account through the thickness of the cylinder. An internal pressure $P_{im} = 225$ mmHg is imposed on the inner surface of the cylinder. The results of the implemented FEM model are compared with the same model in an FEM commercial software (Abaqus). As seen on Fig. 5.3, both the final displacement field and the final stress field are correctly predicted by our finite element implementation. A maximum error of 3% has been observed with respect to the Abaqus results. The biggest error in the prediction occurs for the normal

axial stress, which is predicted uniform through the wall thickness by our model, although it is not the case in the non-linear Abaqus code [128]. It seems that the above-mentioned error caused by our linearization approach as this uniform axial stress through the wall thickness is also observed when we solve the problem with the linearized Abaqus code [128] (see Fig. 5.4).

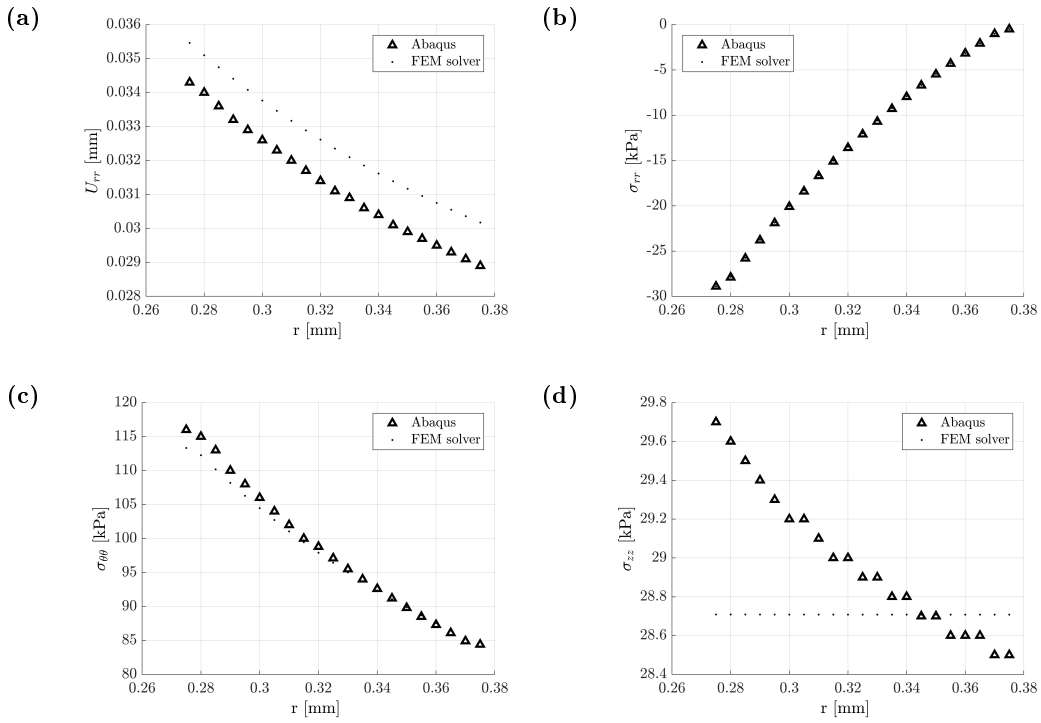

Figure 5.3: (a) Radial displacement, (b) radial stress, (c) circumferential stress, and (d) axial stress of the nodes across the thickness of the cylinder as computed by our implemented FEM and by Abaqus for a linear elastic material.

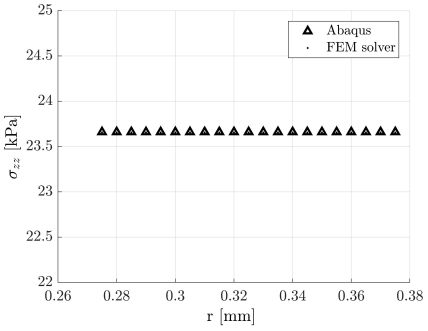

Figure 5.4: Axial stress of the nodes across the thickness of the cylinder as computed by linearized Abaqus code and developed FEM solver for a linear elastic material.

5.4.2 Validation for a thin-wall cylinder by comparison with an equivalent problem on a RVE

As a second validation test case, we consider a thin-wall cylinder (with average radius $R_a = 0.28mm$ and thickness $H = 0.01mm$) subjected to an inner pressure P_{im} on the inner surface, while all other surfaces are considered as traction free. The cylinder is made up of the adventitial material as described in chapter 3 (see Fig. 5.5).

The analytical expression of the stress field of such a problem reads as:

$$\mathbf{\Sigma} = \begin{bmatrix} \Sigma_{rr} & 0 & 0 \\ 0 & \Sigma_{\theta\theta} & 0 \\ 0 & 0 & 0 \end{bmatrix}, \tag{5.14}$$

with,

$$\begin{aligned} \Sigma_{\theta\theta} &= \frac{P_{im} R_a}{H} \\ \Sigma_{rr} &= -\frac{P_{im}}{2}. \end{aligned} \tag{5.15}$$

The stress is computed from Eq. (5.15) based on the pressure and the current geometry of the body (R_a and H are respectively deformed average radius and deformed thickness) at each increment. The stress is imposed as a homogeneous boundary condition on the RVE, and the algorithm described in Chapter 2 (see page 46) allows to compute the subsequent deformation field, which, in turn, allows to update the geometrical parameters R_a and H used in the next loading

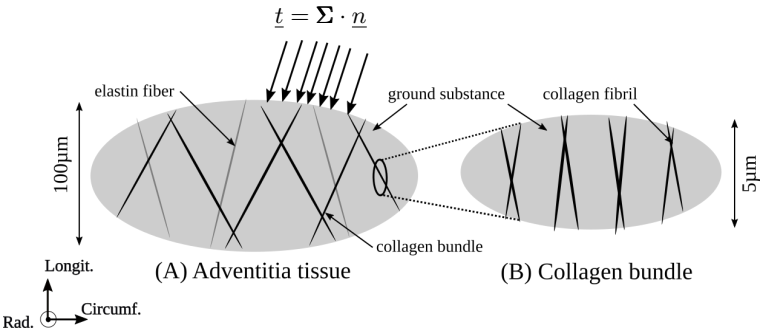

Figure 5.5: The adventitia RVE is remotely subjected to traction forces at its remote boundary.

step. Then, assuming a uniform stress field in the thin wall cylinder, we compared the response of an RVE with the FEM implementation.

Thus, an inflation simulation was performed using the finite element solver, then the computed inner radius-pressure curve was compared with the analytical solution. The FE simulation was performed with different numbers of elements (2, 5 and 10 elements) across the thickness of the cylinder, with four integration points per element. The constitutive relation being computed at the integration point, one RVE is assigned to each integration point. The results show that a convergence is reached with 5 elements across the thickness (see Fig. 5.6). Furthermore, the results show an excellent agreement between the finite element and analytical solutions (0.5% error with respect to the analytical solution).

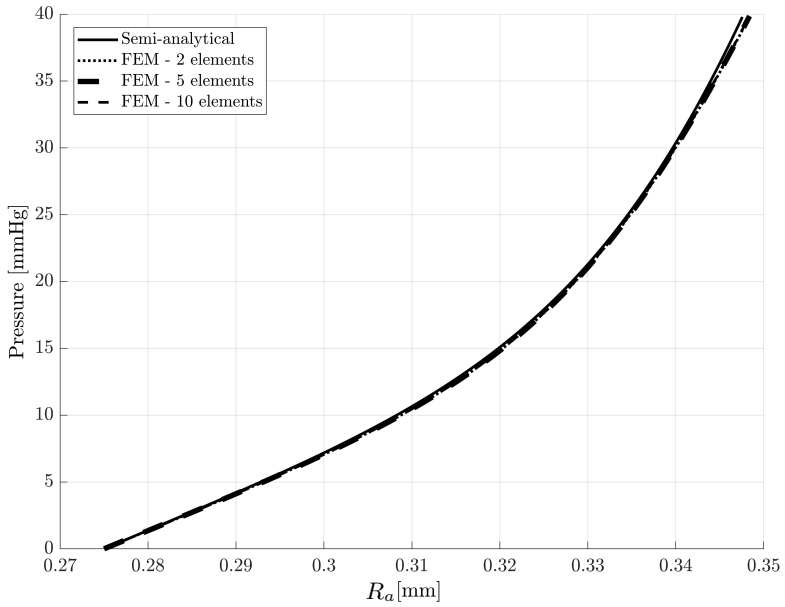

Figure 5.6: The inner radius-pressure curve observed in mesh convergence study of a cylinder having a thickness of H =0.01mm.

Similar simulations are performed with different thicknesses of cylinder wall (H =0.025mm and H =0.05mm) for the further validation of the finite element implementation. As we expected the FEM and analytical results perfectly agree for a thin wall cylinder for which the analytical solution is valid (see Fig. 5.7). However, by increasing the thickness, we do not obtain a uniform stress across the cylinder wall as it was assumed for the analytical solution, thus there is an increasing discrepancy between the analytical and FE results. The error is 0.9% for the cylinder with a thickness of H =0.025mm and is 1.3% for the cylinder with a thickness of H =0.05mm.

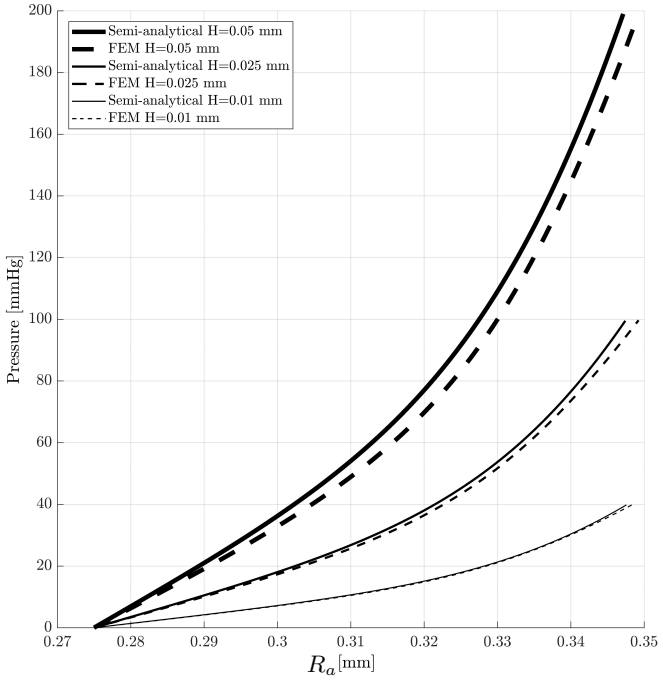

Figure 5.7: Comparing the inner radius-pressure curve from FEM and analytical solution of a thin wall cylinder with different wall thicknesses (H =0.01mm, H =0.025mm, and H =0.05mm), considering five elements across the thicknesses.

5.5 Application to the arterial inflation

Since the inflation test is the closest test to the physiological conditions [68, 88, 157], we here simulate the experiments performed on mice samples by Gilles Faury [35]. More precisely, the experiments were performed as follows: a segment of the mouse renal artery was quickly excised and placed in a physiological buffer. Then, the artery was cleaned of connective tissue and fat before being mounted onto a pressure arteriograph, where the proximal and distal ends of the arterial segment were grasped with extra-fine-point no. 5 microforceps and held in position on the microcannula with a Lexan pinch clamp [35, 34] (see Fig. 5.8). The experiments were performed at 37°C in a bath filled with physiological buffer. The setup was placed under an inverted microscope connected to a computerized system

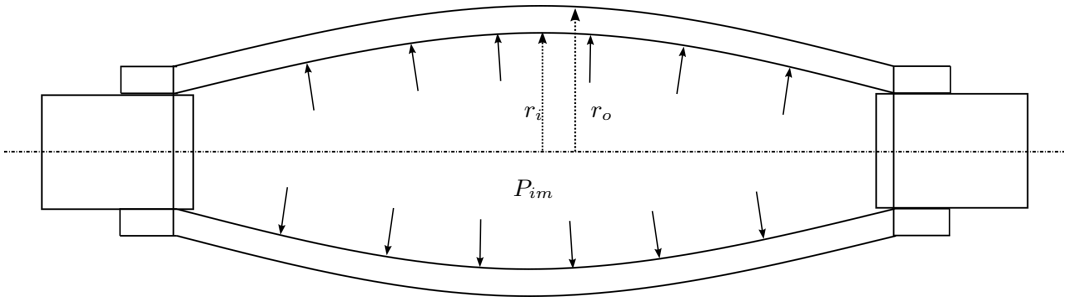

Figure 5.8: Schematic of inflation test for an artery.

allowing the continuous recording of the artery diameters. Then, the pressure was increased from 0 to 175 mmHg by steps of 25 mmHg, following a 5 minutes equilibration period per step (see Fig. 5.8).

Accordingly, the arterial wall is modeled as a thick wall cylinder, with axially constrained ends (see Fig. 5.9). The mechanical loading and boundary conditions to the inflation problem read as follows: an increasing internal pressure P_{im} is applied incrementally from 0 to 175 mmHg on the inner surface of the cylinder, while the outer surface is let traction free. Furthermore, a symmetry condition along the axial direction is considered at the two crosssections. The experiments reported an initial inner radius of $R_i = 0.17$ mm, and an outer radius of $R_o = 0.22$ mm, the wall thickness is divided into two equally thick sub-layers, the media and adventitia. The adventitia layer is modeled by employing the developed multi-scale model of Chapter 3. The media layer is divided into four equally thick sublayers, being alternatively an elastic lamellae and some interlamellar space (see Fig. 5.9). The mechanical properties of each of these layers are assigned according to Chapter 4.

The response of the FE model in terms of internal pressure versus inner radius evolution is compared to the experimental inflation results, as shown on Fig. 5.10 and the collagen fiber and fibril evolutions are also reported.

Two different simulations have been performed: the first one was run with the sets of parameters identical to the ones reported in Chapter 3 and 4 (see Table 5.2), i.e. with the free parameters being equal to: $\theta_{b-adv} = 39°$ and $\phi_{c-med} = 50°$; for the second one, the free parameters were adjusted so as to fit the experimental response; the best parameters read as: $\theta_{b-adv} = 40°$ and $\phi_{c-med} = 33°$. Fig. 5.10 reports the results of these two simulations (respectively labelled model A and

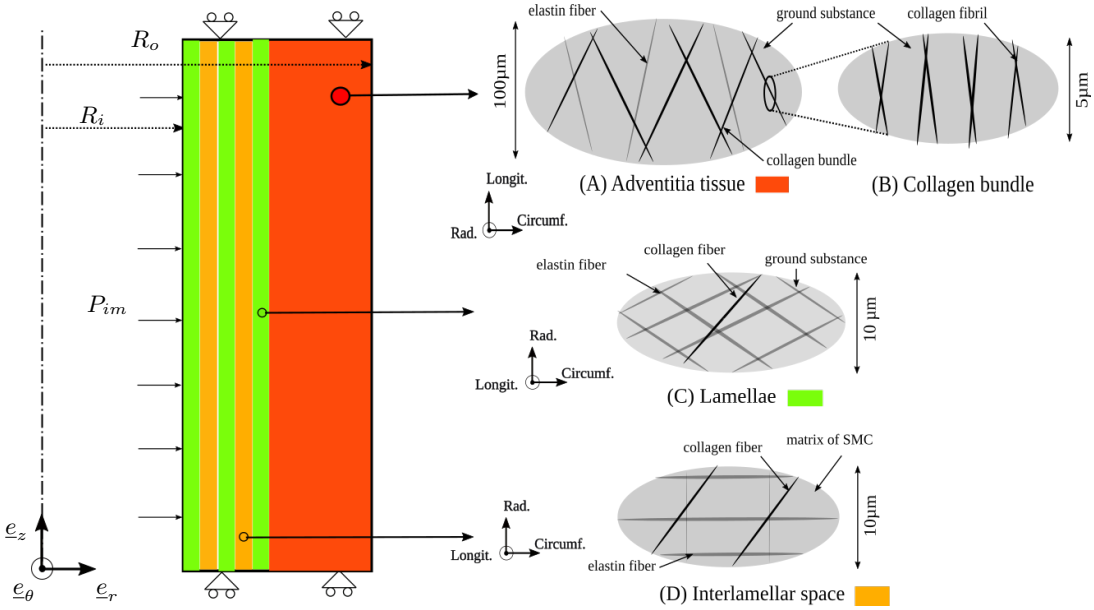

Figure 5.9: Inflation of an artery regarded as a thick-walled cylinder made of adventitia, elastic lamellae and interlamelar space. The initial inner radius of $R_i = 0.17$ mm, and an outer radius of $R_o = 0.22$ mm.

model B). One notices that they fail at correctly reproducing the experimental curve. This may be due to a different microstructural composition or morphology. To investigate this aspect, several simulations were performed to capture the mechanical properties of the mouse renal artery. These investigations illustrate that there are two ways to achieve better prediction of the mouse renal artery's mechanical response: (i) reducing the volume fraction of the collagen fibers, and (ii) increasing the level of hydration of the collagen fibers.

First, a simulation (labelled as FEM model C) was performed where the fraction of collagen fibers was reduced in both layers: media and adventitia layers, $f_{c-la} = f_{c-in} = 5\%$ and $f_{f-b} = 15\%$. Furthermore, the degree of adventitial collagen fibril crimping was increased and set as $\theta_{f-b} = 43°$. The results illustrated that the FEM model (C) provides a better estimation of the mechanical response of the mouse renal artery (see Fig. 5.10, model C: $R^2 = 0.71$).

The alternative solution to obtain a better prediction of the mechanical response of the unknown microstructure mouse renal artery is increasing the level of hydration of collagen fibers, in particular in the media layer. According to the

Parameters		Collagen	Elastin	Ground substance
mechanical constant		$E_b = 250$ MPa	$E_{el} = 1$ MPa	$E_m = 0.01$ MPa
		$\nu_b = 0.34$	$\nu_e = 0.34$	$\nu_m = 0.34$
volume fraction	upper scale	$f_{b-ad} = 30\%$	$f_{el-ad} = 20\%$	$f_{m-ad} = 1 - \sum_i f_i$
	lower scale	$f_{f-b} = 30\%$	NA	NA
orientation	upper scale	$\theta_{b-ad} =$ Free parameter	$\theta_{el-ad} = 0^\circ$	NA
		$\phi_{b-ad} = 90^\circ$	$\phi_{el-ad} = 90^\circ$	NA
	lower scale	$\theta_{f-b} = 35^\circ$	NA	NA
		$\phi_{b-ad} = 90^\circ$	NA	NA

Parameters		Collagen	Ground substance
mechanical constant		$E_c = 250$ MPa	$E_{m-la} = 0.01$ & $E_{m-in} = 0.05$ MPa
		$\nu_b = 0.34$	$\nu_m = 0.34$
volume fraction	Lamellae	$f_{c-la} = 25\%$	$f_{m-la} = 1 - \sum_i f_i$
	Interlamellar space	$f_{c-in} = 25\%$	$f_{m-in} = 1 - \sum_i f_i$
orientation	Lamellae	$\theta_{c-med} = 85^\circ$	NA
		$\phi_{c-med} =$ Free parameter	NA
	Interlamellar space	$\theta_{c-med} = 85^\circ$	NA
		$\phi_{c-med} =$ Free parameter	NA

Parameters		Elastin 1	Elastin 2	Elastin 3
mechanical constant		$E_{el1} = 1$ MPa	$E_{el2} = 1$ MPa	$E_{el3} = 1$ MPa
		$\nu_{el1} = 0.34$	$\nu_{el2} = 0.34$	$\nu_{el3} = 0.34$
volume fraction	Lamellae	NA	$f_{el2-la} = 30\%$	$f_{el3-la} = 5\%$
	Interlamellar space	$f_{el1-in} = 5\%$	$f_{el2-in} = 5\%$	$f_{el3-in} = 5\%$
orientation	Lamellae	NA	$\theta_{el2-med} = 90^\circ$	$\theta_{el3-med} = 0^\circ$
		NA	$\phi_{el2-la} = 70^\circ$	$\phi_{el3-la} = 90^\circ$
	Interlamellar space	$\theta_{el1-med} = 90^\circ$	$\theta_{el2-med} = 90^\circ$	$\theta_{el3-med} = 0^\circ$
		$\phi_{el1-in} = 0^\circ$	$\phi_{el2-in} = 70^\circ$	$\phi_{el3-in} = 90^\circ$

Table 5.2: Summary of the model parameters and constants.

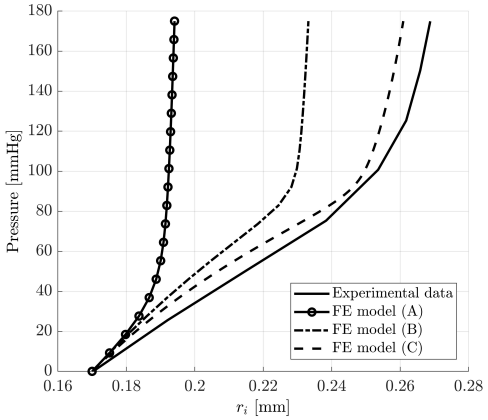

Figure 5.10: Comparing FE model with inflation experiment on the mouse renal artery[35]. FEM model (A) : $\theta_{b-adv} = 39°$ and $\phi_{c-med} = 50°$. FEM model (B): $\theta_{b-adv} = 40°$ and $\phi_{c-med} = 33°$. FEM model (C): $\theta_{f-b} = 43°$, $f_{c-la} = f_{c-in} = 5\%$ and $f_{f-b} = 15\%$.

literature, the media layer contains collagen type III fibers, which have a lower elastic modulus as compared to the fibers made of collagen type I. Asgari et al. [2] showed that the elastic modulus of a tissue decreases exponentially as the ratio of Col-III:Col-I increases. For the sake of simplicity, we previously considered the same mechanical properties for the collagen fibers in the adventitia and media layers ($E = 250$MPa). In the lower scale RVE of the adventitia model, the collagen fibrils have a Young's modulus of E=250 MPa, which leads to a modulus of the collagen fibers of E = 50 MPa after homogenization (which accounts for their hydration degree). Consequently, we decided to assign the hydrated medial collagen fibers the lattest value for their Young's modulus. Accordingly, the model is able to better capture the mechanical response of the mouse renal artery, when this change is added to the previously detailed modifications in the parameters (see Fig. 5.11, model D: $R^2 = 0.76$).

The value of stress and displacement at the center of the 30 quadrilateral elements across the thickness of the artery were illustrated at three pressures during the inflation test; namely, 0 mmHg, 90 mmHg, and 175 mmHg (see Fig. 5.12). From the inner radius $R_i = 0.17$mm, the first 15 elements represent the media layer, and the other 15 elements belong to the adventitia layer. The media layer is divided into four equally thick sublayers, being alternatively an

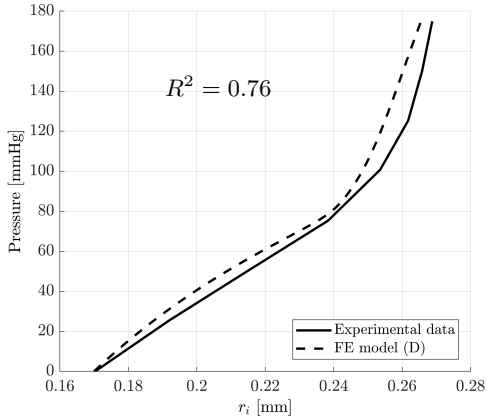

Figure 5.11: Comparing FE model with inflation experiment on the mouse renal artery[35]. FEM model (D) : $\theta_{b-adv} = 40°$, $\phi_{c-med} = 32°$, $\theta_{f-b} = 43°$, and $f_{c-la} = f_{c-in} = f_{f-b} = 15\%$.

elastic lamellae and an interlamellar space, where each of these sublayers contains three elements.

The displacement field across the thickness is displayed on Fig. 5.11, at two values of the pressure field, namely 90 mmHg and 175 mmHg. One can distinguish different slopes on these curves, corresponding to the different layers of the tissue, which have different homogenized stiffnesses. The displacement across the thickness is shown on the Fig. 5.12 (a) for the pressure of 90 mmHg and 175 mmHg, where the two slopes belonging to the media and adventitia layers are distinguishable. Fig. 5.12 (b), Fig. 5.12 (c), and Fig. 5.12 (d) show respectively the stresses along radial, circumferential and axial directions at the center of the 30 elements across the thickness of the artery. The stresses increase by increasing the pressure. The level of stress along circumferential and radial direction decrease across the thickness from the inner radius to the outer radius. The fluctuations in the media layer are due to the presence of the lamellae and interlamellar space. The level of axial stress at the interface between the adventitia and the media was the lowest as the fibers at this place experienced less rotation compared to the other places in the media (see Fig. 5.13(b)).

The collagen fiber orientation across the thickness of the artery are shown on the Fig. 5.13 for the three pressures. Note that $\theta°$ represents the orientation of fibers in the axial-circumferential plane and $\phi°$ represents the orientation of fibers

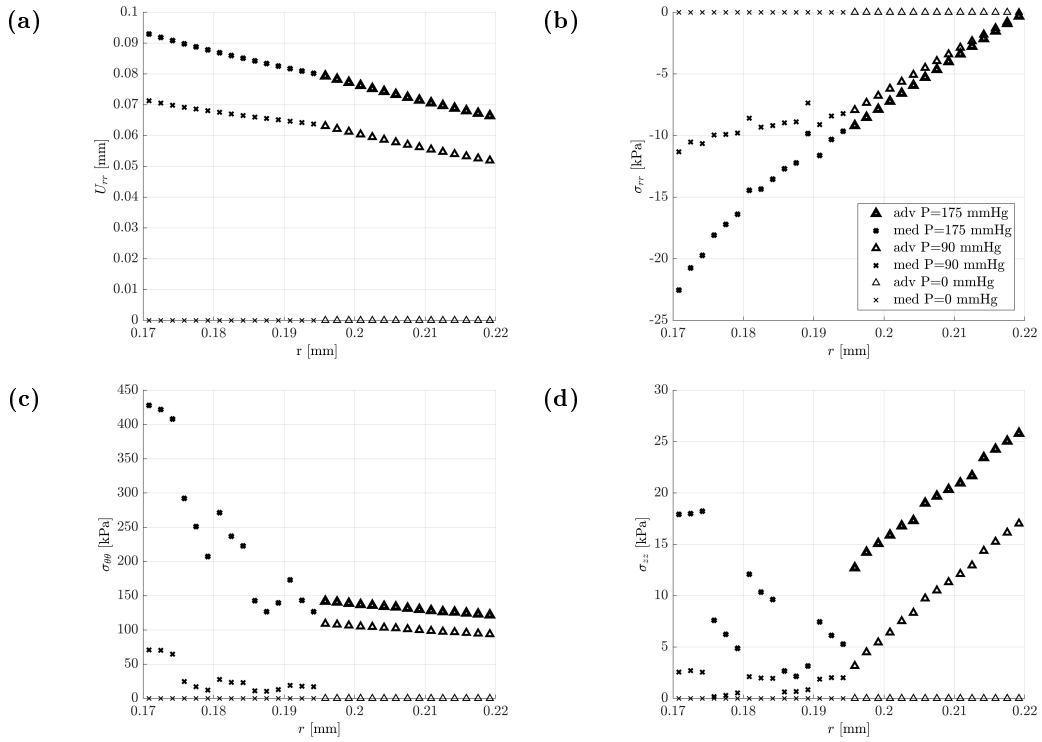

Figure 5.12: (a) Radial displacement, (b) radial stress, (c) circumferential stress, and (d) axial stress at the center of the elements across the thickness of the artery.

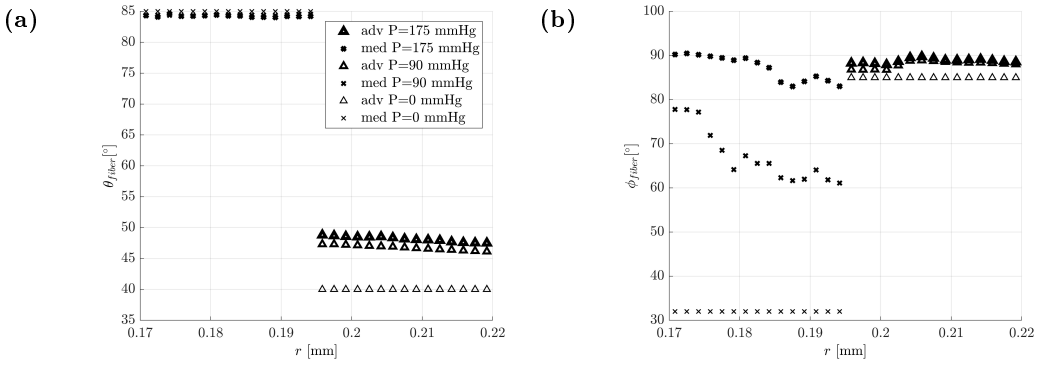

Figure 5.13: Fiber reorientation at the center of elements across the thickness of the artery at three internal pressures. (a) The orientation of fibers in the axial-circumferential plane. (b) The orientation of fibers in the radial-circumferential plane.

in the radial-circumferential plane of the artery. At the initial instant, collagen fibers are oriented at 40° in the adventitia and 85° in the media layer with respect to the axial direction in the axial-circumferential plane (see Fig. 5.13(a)). This angle increases in the adventitia layer by increasing the internal pressure of the artery, such that at the interface of adventita and media, where the adventitia experiences the higher radial and circumferential stresses, we have the largest reorientation. However, in the media layer, the orientation of fibers in the radial-circumferential plane almost remain fixed (85°) (see Fig. 5.13(a)), but the fibers experienced a large rotation in the radial-circumferential plane from 32° to 90° (see Fig. 5.13(b)).

The collagen fibrils are oriented initially with an angle of 43° with respect to the collagen bundle orientation (θ_{f-adv}) in the adventitia. The results demonstrate that increasing the internal pressure also induces an evolution of the fibrils orientation. Fig. 5.14 shows that the fibrils were reoriented toward the direction of the collagen bundles by increasing the internal pressure, i.e. they undergo decrimping. The region with maximum circumferential stress corresponds also to the region where the fibrils experienced the largest decrimping.

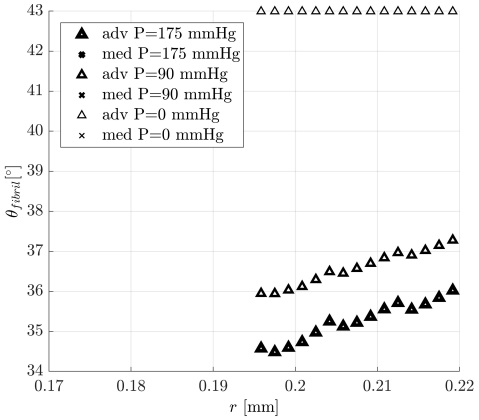

Figure 5.14: Fibril reorientation at the center of elements across the thickness of the artery at three internal pressures.

5.6 Discussion

The multiscale micromechanical model was implemented in the finite element formulation to simulate the inflation of an artery. For the sake of simplicity and in order to reduce the computational costs, several simplification assumptions have been made to solve the problem. The arterial geometry was simplified to a hollow cylinder and the initial configuration was considered as stress-free and strain-free. Due to the hypoelastic formulation of the problem, it is assumed that the stiffness remains constant during the load increment for infinitely small time steps dt. It is also assumed that the deformation during the time interval dt is small such that the stress field and the applied pressure at time t are in equilibrium on the configuration at time $t + dt$, and that the update of the stiffness tensor does not induce a further imbalance.

After validating the home-made finite element solver, the multi-scale constitutive model described and validated in Chapter 3 and Chapter 4 for the human coronary artery was implemented in the finite element solver. The variation of pressure-radius was calculated during the internal pressure simulation and compared with the experimental results of the mouse renal artery [35]. The result for the pressure-radius variation exhibited the same trend as the experiment, although the response for the human coronary artery, i.e. with the free parameters being set to $\theta_{b-adv} = 39°$ and $\phi_{c-med} = 50°$ was stiffer as compared to the mouse

renal artery. Since we did not have access to microstructural images for these tests, we decided to vary the free parameters (i.e. we chose $\theta_{b-adv} = 40°$ and $\phi_{c-med} = 32°$) as well as the volume fraction and hydration of the collagen fibers. It was shown to provide a good estimation of the mechanical response of the artery. Furthermore, the stress distribution through the arterial wall revealed good accordance with fiber orientation, which has also been observed experimentally [157, 82]. The results show the capability of the model to capture the microstructural evolution as well as the macroscopic mechanical response of the artery over time from fiber evolving configurations to structural modeling.

5.7 Conclusion

In conclusion, we have shown that the hypoelastic formulation in the framework of continuum micromechanics is capable of accurately predicts the microscale fiber kinematics and macroscopic mechanical response of the artery over time from fiber evolving configuration to structural modeling. This model could provide new insights into structural constitutive modeling of arteries to incorporate the patient-specific features from microstructure up-to arterial geometry of the patient, since the model permits the investigation of different parameters such as fibers orientation and fraction on the macroscopic response of an artery, as well as damage occurring at the fiber level. As a perspective towards patient-specific simulation, the present model can be integrated inside finite element commercial software to solve the complex geometry of the artery in 3D and without the simplifications which have been made in this study.

General Conclusion

As we discussed, the physical mechanisms and microstructural evolution that occur within the microstructure of the artery dictate its mechanical properties. To investigate these microstructural mechanisms and their macroscopic mechanical consequences, we proposed a hypoelastic constitutive model in the framework of continuum micromechanics, taking into account universal patterns (representative volume element) of the hierarchical organization of arteries at different scales.

- For the sake of simplicity, the minimum of microstructural information, which is essential to obtain reliable predictions of macroscopic mechanical behavior of the artery. The main orientation of collagen and elastin fibers, as well as their volume fractions, were obtained from image analysis of the arterial images and considered in our representative volume element (RVE). The representation of the fiber network in the form of the principal orientation of fibers was also used in some well-established constitutive models [45, 62, 61, 63].

- To the best of our knowledge, the developed constitutive model is the first to address the nonlinearity of the arterial tissue through the collagen bundle reorientation and the anisotropy through the preferred orientation of the fibers as it has been observed experimentally [22, 82]. In our model, elastin fiber, collagen fibril, and soft ground matrix were modeled as hypoelastic material (hypoelastic modulus and the hypoelastic Poisson's ratio) and the only source of non-linearity is due to microstructural evaluation. Hypoelastic formulation accounts for the large rotation and deformation such that at higher stresses the fibers can generate shear stresses to rotate more than the matrix (non-affine deformation). The fibers at upper scale RVE reoriented toward the load direction (fiber decrimping) and the fibrils

in the lower scale RVE tend to be aligned with the fiber direction (fibril decrimping), while the fibril decrimping does not occur right after applying the load. All these microstructural phenomena are in good agreement with experimental observations [82, 22].

- In the model, the matrix phase and fibers are isotropic material, while the homogenized RVE behaves anisotropically. The anisotropy behavior of the model comes from the shape and the orientation of the fibers within the RVEs. The latter has been also applied in the framework of continuum micromechanics to model the anisotropic behavior of bone [40, 41, 39].

- The fiber interaction has been correctly predicted by the Mori-Tanaka assumption [94]. In the media layer, the higher fraction of fibers limits their rotation compared to the rotation of fibers in the adventitia layer. This observation is in good agreement with the experimental measurements [82, 22]. Although Mori-Tanaka scheme only considers the modeling of fiber-matrix interaction, in which fibers can only interact between each other through the matrix rather than the direct interaction between the network of fibers. However, considering all these interactions in a complex biological tissue through the implementation of the finite element method is computationally expensive [76].

- The multiscale micromechanical model was implemented in the finite element formulation to simulate the inflation of an artery. For the sake of simplicity and for reducing the computational costs, several simplification assumptions have been made to solve the problem. The results show the capability of the model to capture the microstructural evolution as well as the macroscopic mechanical response of the artery over time from fiber evolving configurations to structural modeling. An agreement was observed between the simulation and experiment both for fibers reorientations and macroscopic mechanical response of the artery.

The modeling of these microstructural phenomena and access to the microstructural deformation and stresses is crucial for the constitutive model to be capable of accounting for the growth and remodeling, damage and modeling of other pathologies. The proposed model has also some limitations:

- The complexity of tissue microstructures cannot be modelled in every detail. Thus, constituents with known physical quantities (shape, volume fraction and Young's modulus) are identified. These physical quantities introduced as physical parameters in the model for each constituent such as shape, volume fraction, orientation, and homogeneous mechanical properties. Determining these parameters is a challenging part of building the constitutive model, although most of them were shown to be constant from sample to sample.

- Although fibers are oriented randomly in all directions in the tissue, the model considers only the main orientation family fibers. The model also can account for a probability distribution function of fiber orientation as it was tested during the implementation. However, for a statistically valid sampling size, we needed a large number of fibers which made the computational cost very high.

- The biological components are known as complex heterogeneous and nonlinear materials, for instance, proteins are even modeled as a polymer chain [70]. However, in the proposed model, the elementary constituents were modeled as isotropic linear elastic at lower scale RVEs. For the sake of simplicity and in order to account for the microstructural phenomena and to illustrate its effect on the macroscopic mechanical response, the constituents were assumed as isotropic linear elastic. However, some experimental observation supports this assumption. For instance, fibrils have been shown to behave almost linearly at the lower scale in their deformation range [141, 70].

Future work will permit to extend the proposed arterial constitutive model in contributing to:

- Growth and remodeling: as this micromechanical framework has become a reliable tool to model hard tissues (bone) [40, 41, 97, 143], it is expected that it can also become a basic tool to study the contribution of different microstructural components in the mechanical behavior of the artery. This will be beneficial in predicting the evolution of the tissue mechanical response overtime during pathologies inducing remodeling and damage of

the extracellular matrix [122, 105, 142]. This will imply coupling the current version of the model with biological considerations in the near future.

- Accounting for further microstructural mechanisms: The model is capable to include the pre-strain in the microstructure at the fiber network level. Due to the existence of the pre-strain in the artery [13, 23], this could improve the model to have a better prediction of arterial structure mechanical response. This can also be extended to incorporate the microstructural damage at the fiber network level.

- Patient-specific simulation: the constitutive model could be integrated into the finite element commercial software to incorporate the patient-specific features from the microstructure up-to arterial geometry of the patient.

A | Eshelby auxiliary tensor

The Eshelby auxiliary tensor $\mathbb{L}$ is defined as $\mathbb{L}(x) = \int_{\Omega_I} \mathbb{G}(x, x')dV(x')$, where $\mathbb{G}(x, x')$ is the elastic Green's function. The elastic Green's function is the velocity field $\underline{v}(\underline{x})$, solution of the momentum balance in which the elastic constitutive function and compatibility equation have been incorporated, i.e. the solution of $C^m_{ijkl}u_{k,li} + b_j = 0$, when the body force $\underline{b}$ is a delta function, i.e. $b_j(x) = \delta(x - x')\delta_{kj}$, and $\mathbb{C}^m$ is the stiffness of an infinite homogeneous matrix [31]. The components of the Eshelby auxiliary tensor for the ellipsoid with a basis frame aligned with the axes of the ellipsoid (see Fig. A.1) are equal to:

$$
\begin{aligned}
L_{1111} &= Qa^2 I_{aa} + RI_a \\
L_{2222} &= Qb^2 I_{bb} + RI_b \\
L_{3333} &= Qc^2 I_{cc} + RI_c \\
L_{2112} &= L_{2211} = Qb^2 I_{ab} + RI_a \\
L_{3113} &= L_{3311} = Qc^2 I_{ac} + RI_a \\
L_{1212} &= Qb^2 I_{ab} - RI_a \\
L_{1313} &= Qc^2 I_{ac} - RI_a \\
L_{1122} &= L_{1221} = Qa^2 I_{ab} + RI_b \\
L_{2121} &= Qa^2 I_{ab} - RI_a \\
L_{3223} &= L_{3322} = Qc^2 I_{ab} + RI_b \\
L_{2323} &= Qc^2 I_{bc} - RI_b \\
L_{3131} &= L_{1331} = Qa^2 I_{ac} + RI_c \\
L_{3131} &= Qa^2 I_{ac} - RI_c \\
L_{2233} &= Qb^2 I_{bc} - RI_c \\
L_{3232} &= L_{2332} = Qb^2 I_{bc} + RI_c
\end{aligned}
\tag{A.1}
$$

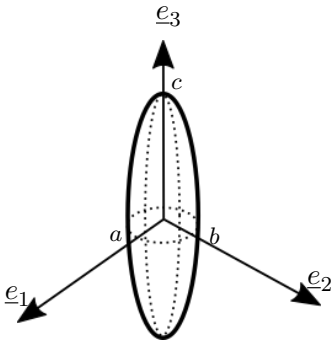

Figure A.1: Ellipsoidal inclusion with principal axess of a, b, and c.

where a, b, and c are the principal axes of the ellipsoid, and $Q = \frac{3}{8\pi(1-\nu^m)}$ and $R = \frac{1-2\nu^m}{8\pi(1-\nu^m)}$. ν^m is the Poisson's ratio of the matrix. The Eshelby auxiliary tensor depends on the shape and orientation of the inclusion as well as the stiffness of the surrounding medium. An infinitely long cylinder fiber is assumed as an ellipsoid with a circular transverse section, i.e. $a = b = 1$ when the longest axis approaches infinity, $c \to \infty$. Thus, the I terms which are defined in terms of standard elliptic integrals [96] can be modified as follows,

$$\begin{aligned} I_a &= \frac{4\pi b}{a+b} \\ I_b &= \frac{4\pi a}{a+b} \\ I_c &= 0 \\ I_{ab} &= \frac{4\pi}{3(a+b)^2} \\ c^2 I_{ac} &= \frac{1}{3} I_a \\ I_{aa} &= \frac{4\pi}{3a^2} - I_{ab} \\ I_{bb} &= \frac{4\pi}{3b^2} - I_{ab} \\ c^2 I_{cc} &= 0 \end{aligned} \tag{A.2}$$

An oblate spheroid is assumed as an ellipsoid when the two principal axes

approach infinity, i.e. c & $b \to \infty$. Then, the I terms can be modified as follows,

$$\begin{aligned} I_a &= \frac{4\pi}{a} \\ I_b &= 0 \\ I_c &= 0 \\ I_{ab} &= 0 \\ c^2 I_{ac} &= \frac{1}{3} I_a \\ I_{aa} &= \frac{4\pi}{3a} \\ I_{bb} &= 0 \\ c^2 I_{cc} &= 0 \end{aligned} \tag{A.3}$$

The fourth-order Eshelby concentration tensors for strain rate and spin were introduced in the Eqs. (2.26) and (2.27) are respectively equal to [31]:

$$\begin{aligned} S_{ijmn} &= \frac{1}{2}(L_{iklj} + L_{jkli}), \\ R_{ijmn} &= \frac{1}{2}(L_{iklj} - L_{jkli}), \end{aligned} \tag{A.4}$$

B | Image processing

The stacks of images from Krasny experiments [82] were analyzed to determine the volume fractions and orientation of collagen and elastin fibers in the adventitia and media layers. In total, we analyzed 12 stacks of images, coming from four samples tested in the longitudinal, circumferential and diagonal directions respectively. In each case, the initial configuration which is reported is analyzed after few cycles of preconditioning in the load direction. These images were analyzed with ImageJ through the Otsu thresholding technique [103] to compute the volume fractions of elastin and collagen. The orientation of fibers was analyzed using orientationJ, a series of ImageJ plugins for directional image analysis [107, 114], as well as the 2D fast Fourier transformation method proposed by [82]. The results are shown for the adventitia in Table C.1 and for media in Table C.2. Note that the orientation values are reported in these tables are the main orientations that were obtained from 2D fast Fourier transformation.

Measurement	Sample 1			Sample 2		
	circ	long	diag	circ	long	diag
Collagen volume fraction [%]	24 ± 5	23±8	30± 5	-	4 ±3	18 ± 7
Elastin volume fraction [%]	4±2	2±1	9±2	-	2±1	11±5
Colllagen fiber orientation [°]	15	93	65	80	0&95	60
Elastin fiber orientation [°]	7	0&90	8	32&17	20	20

Measurement	Sample 3			Sample 4		
	circ	long	diag	circ	long	diag
Collagen volume fraction [%]	5 ± 3	21 ± 10	7 ± 3	-	12 ±5	9±5
Elastin volume fraction [%]	14± 5	16 ± 5	5 ±4	-	3±2	7±5
Colllagen fiber orientation [°]	16	75	5	-	74	11
Elastin fiber orientation [°]	16	80	0	-	11	86

Table B.1: The collagen and elastin fibers orientation and volume fraction from image analysis of adventitia stacks' images.

Measurement	Sample 1			Sample 2		
	circ	long	diag	circ	long	diag
Collagen volume fraction [%]	19±5	18±5	20±5	19±5	-	-
Elastin volume fraction [%]	22±10	21 ±10	25±5	18±3	-	-
Colllagen fiber orientation [°]	88	85	87	90	-	81
Elastin fiber orientation [°]	96	80	83	89	-	87

Measurement	Sample 3			Sample 4		
	circ	long	diag	circ	long	diag
Collagen volume fraction [%]	30±5	27±5	33±10	-	25±5	20±5
Elastin volume fraction [%]	26±5	21±5	31±5	-	17±5	17±5
Colllagen fiber orientation [°]	96	94	94	-	87	97
Elastin fiber orientation [°]	88	94	93	-	58	94

Table B.2: The collagen and elastin fibers orientation and volume fraction from image analysis of media stacks' images.

Bibliography

[1] Aaron and Gosline. Elastin as a random-network elastomer: A mechanical and optical analysis of single elastin fibers. *Biopolymers*, 20(6):1247–1260, 1981.

[2] Meisam Asgari, Neda Latifi, Hossein K Heris, Hojatollah Vali, and Luc Mongeau. In vitro fibrillogenesis of tropocollagen type iii in collagen type i affects its relative fibrillar topology and mechanics. *Scientific reports*, 7(1):1392, 2017.

[3] SN Atluri and ANTONIO Cazzani. Rotations in computational solid mechanics. *Archives of Computational Methods in Engineering*, 2(1):49–138, 1995.

[4] Gang Bao and Subra Suresh. Cell and molecular mechanics of biological materials. *Nature materials*, 2(11):715–725, 2003.

[5] Yakov Benveniste. A new approach to the application of mori-tanaka's theory in composite materials. *Mechanics of materials*, 6(2):147–157, 1987.

[6] DH Bergel. The static elastic properties of the arterial wall. *The Journal of physiology*, 156(3):445–457, 1961.

[7] Panagiotis Berillis. The role of collagen in the aorta's structure. *The open circulation and vascular journal*, 6(1), 2013.

[8] Daniele Bianchi, Michele Marino, and Giuseppe Vairo. An integrated computational approach for aortic mechanics including geometric, histological and chemico-physical data. *Journal of biomechanics*, 49(12):2331–2340, 2016.

[9] B Budiansky, JW Hutchinson, and S Slutsky. Void growth and collapse in viscous solids. In *Mechanics of solids*, pages 13–45. Elsevier, 1982.

[10] Alan C Burton. Relation of structure to function of the tissues of the wall of blood vessels. *Physiological reviews*, 34(4):619–642, 1954.

[11] Amnon Buxboim, Irena L Ivanovska, and Dennis E Discher. Matrix elasticity, cytoskeletal forces and physics of the nucleus: how deeply do cells 'feel'outside and in? *J Cell Sci*, 123(3):297–308, 2010.

[12] Peter B Canham, Peter Whittaker, Sharon E Barwick, and Monika E Schwab. Effect of pressure on circumferential order of adventitial collagen in human brain arteries. *Canadian journal of physiology and pharmacology*, 70(2):296–305, 1992.

[13] L Cardamone, A Valentin, JF Eberth, and JD Humphrey. Origin of axial prestretch and residual stress in arteries. *Biomechanics and modeling in mechanobiology*, 8(6):431, 2009.

[14] Cristina Cavinato, Pierre Badel, Witold Krasny, Stephane Avril, and Claire Morin. Experimental characterization of adventitial collagen fiber kinematics using second harmonic generation imaging microscopy: Similarities and differences across arteries, species and testing conditions. 2020.

[15] Cristina Cavinato, Clementine Helfenstein-Didier, Thomas Olivier, Sabine Rolland Du Roscoat, Norbert Laroche, and Pierre Badel. Biaxial loading of arterial tissues with 3d in situ observations of adventitia fibrous microstructure: A method coupling multi-photon confocal microscopy and bulge inflation test. *Journal of the mechanical behavior of biomedical materials*, 74:488–498, 2017.

[16] Huan Chen, Xiaomei Guo, Tong Luo, and Ghassan S. Kassab. A validated 3d microstructure-based constitutive model of coronary artery adventitia. *Journal of Applied Physiology*, 121(1):333–342, 2016.

[17] Huan Chen, Yi Liu, Mikhail N. Slipchenko, Xuefeng Zhao, Ji-Xin Cheng, and Ghassan S. Kassab. The layered structure of coronary adventitia under mechanical load. *Biophysical journal*, 101(11):2555–2562, 2011.

[18] Huan Chen, Tong Luo, Xuefeng Zhao, Xiao Lu, Yunlong Huo, and Ghassan S. Kassab. Microstructural constitutive model of active coronary media. *Biomaterials*, 34(31):7575–7583, 2013.

[19] Huan Chen, Mikhail N Slipchenko, Yi Liu, Xuefeng Zhao, Ji-Xin Cheng, Yoram Lanir, and Ghassan S Kassab. Biaxial deformation of collagen and elastin fibers in coronary adventitia. *Journal of Applied Physiology*, 115(11):1683–1693, 2013.

[20] Matthias Chiquet, David E Birk, Carsten G Bönnemann, and Manuel Koch. Collagen xii: protecting bone and muscle integrity by organizing collagen fibrils. *The international journal of biochemistry & cell biology*, 53:51–54, 2014.

[21] Nusrat Choudhury, Olivier Bouchot, Leonie Rouleau, Dominique Tremblay, Raymond Cartier, Jagdish Butany, Rosaire Mongrain, and Richard L Leask. Local mechanical and structural properties of healthy and diseased human ascending aorta tissue. *Cardiovascular Pathology*, 18(2):83–91, 2009.

[22] Ming-Jay Chow, Raphaël Turcotte, Charles P Lin, and Yanhang Zhang. Arterial extracellular matrix: a mechanobiological study of the contributions and interactions of elastin and collagen. *Biophysical journal*, 106(12):2684–2692, 2014.

[23] Cheng-Jen Chuong and Yuan-Cheng Fung. Residual stress in arteries. In *Frontiers in biomechanics*, pages 117–129. Springer, 1986.

[24] John M Clark and Seymour Glagov. Transmural organization of the arterial media. the lamellar unit revisited. *Arteriosclerosis: An Official Journal of the American Heart Association, Inc.*, 5(1):19–34, 1985.

[25] S Cusack and A Miller. Determination of the elastic constants of collagen by brillouin light scattering. *Journal of molecular biology*, 135(1):39–51, 1979.

[26] Antonio D'Amore, John A Stella, William R Wagner, and Michael S Sacks. Characterization of the complete fiber network topology of planar fibrous tissues and scaffolds. *Biomaterials*, 31(20):5345–5354, 2010.

[27] Dehkordi, Fatahian, A Parchami, et al. Scleroprotein and vascular smooth muscle cell distribution of common carotid media in sheep and goats. *Bulgarian Journal of Veterinary Medicine*, 13(4):211–217, 2010.

[28] Koert P Dingemans, Peter Teeling, Jaap H Lagendijk, and Anton E Becker. Extracellular matrix of the human aortic media: an ultrastructural histochemical and immunohistochemical study of the adult aortic media. *The Anatomical Record: An Official Publication of the American Association of Anatomists*, 258(1):1–14, 2000.

[29] Philip Boone Dobrin. Mechanical properties of arteries. *Physiological reviews*, 58(2):397–460, 1978.

[30] Ambroise Duprey, Khalil Khanafer, Marty Schlicht, Stéphane Avril, David Williams, and Ramon Berguer. In vitro characterisation of physiological and maximum elastic modulus of ascending thoracic aortic aneurysms using uniaxial tensile testing. *European Journal of Vascular and Endovascular Surgery*, 39(6):700–707, 2010.

[31] John D Eshelby. The determination of the elastic field of an ellipsoidal inclusion, and related problems. *Proc. R. Soc. Lond. A*, 241(1226):376–396, 1957.

[32] Paul Farand, André Garon, and Gerard E Plante. Structure of large arteries: orientation of elastin in rabbit aortic internal elastic lamina and in the elastic lamellae of aortic media. *Microvascular research*, 73(2):95–99, 2007.

[33] Gilles Faury. Function–structure relationship of elastic arteries in evolution: from microfibrils to elastin and elastic fibres. *Pathologie Biologie*, 49(4):310–325, 2001.

[34] Gilles Faury, Gail M Maher, Dean Y Li, Mark T Keating, Robert P Mecham, and Walter A Boyle. Relation between outer and luminal diameter in cannulated arteries. *American Journal of Physiology-Heart and Circulatory Physiology*, 277(5):H1745–H1753, 1999.

[35] Gilles Faury, Mylène Pezet, Russell H Knutsen, Walter A Boyle, Scott P Heximer, Sean E McLean, Robert K Minkes, Kendall J Blumer, Attila Kovacs, Daniel P Kelly, et al. Developmental adaptation of the mouse

cardiovascular system to elastin haploinsufficiency. *The Journal of clinical investigation*, 112(9):1419–1428, 2003.

[36] Alan Freed. Anisotropy in hypoelastic soft-tissue mechanics, i: theory. *Journal of Mechanics of Materials and Structures*, 3(5):911–928, 2008.

[37] Alan David Freed. Hypoelastic soft tissues. part i: theory. *Acta mechanica*, 213(1-2):189–204, 2010.

[38] Pierre Fridez, A Makino, H Miyazaki, J-J Meister, K Hayashi, and N Stergiopulos. Short-term biomechanical adaptation of the rat carotid to acute hypertension: contribution of smooth muscle. *Annals of biomedical engineering*, 29(1):26–34, 2001.

[39] Andreas Fritsch, Luc Dormieux, Christian Hellmich, and Julien Sanahuja. Mechanical behavior of hydroxyapatite biomaterials: an experimentally validated micromechanical model for elasticity and strength. *Journal of Biomedical Materials Research Part A*, 88(1):149–161, 2009.

[40] Andreas Fritsch and Christian Hellmich. 'universal'microstructural patterns in cortical and trabecular, extracellular and extravascular bone materials: micromechanics-based prediction of anisotropic elasticity. *Journal of Theoretical Biology*, 244(4):597–620, 2007.

[41] Andreas Fritsch, Christian Hellmich, and Luc Dormieux. Ductile sliding between mineral crystals followed by rupture of collagen crosslinks: experimentally supported micromechanical explanation of bone strength. *Journal of theoretical biology*, 260(2):230–252, 2009.

[42] Thomas J Fuchs and Joachim M Buhmann. Computational pathology: Challenges and promises for tissue analysis. *Computerized Medical Imaging and Graphics*, 35(7-8):515–530, 2011.

[43] Marisa Garcia and Ghassan S Kassab. Right coronary artery becomes stiffer with increase in elastin and collagen in right ventricular hypertrophy. *Journal of Applied Physiology*, 106(4):1338–1346, 2009.

[44] T Christian Gasser, Ray W Ogden, and Gerhard A Holzapfel. Hyperelastic modelling of arterial layers with distributed collagen fibre orientations. *Journal of the royal society interface*, 3(6):15–35, 2005.

[45] T Christian Gasser, Ray W Ogden, and Gerhard A Holzapfel. Hyperelastic modelling of arterial layers with distributed collagen fibre orientations. *Journal of the royal society interface*, 3(6):15–35, 2006.

[46] K Genovese, YU Lee, AY Lee, and JD Humphrey. An improved panoramic digital image correlation method for vascular strain analysis and material characterization. *Journal of the mechanical behavior of biomedical materials*, 27:132–142, 2013.

[47] Paul Germain. The method of virtual power in continuum mechanics. part 2: Microstructure. *SIAM Journal on Applied Mathematics*, 25(3):556–575, 1973.

[48] Colin A Grant, David J Brockwell, Sheena E Radford, and Neil H Thomson. Tuning the elastic modulus of hydrated collagen fibrils. *Biophysical journal*, 97(11):2985–2992, 2009.

[49] Ellen M Green, Jessica C Mansfield, James S Bell, and C Peter Winlove. The structure and micromechanics of elastic tissue. *Interface focus*, 4(2):20130058, 2014.

[50] SE Greenwald, JE Moore, A Rachev, TPC Kane, and J-J Meister. Experimental investigation of the distribution of residual strains in the artery wall. *Journal of biomechanical engineering*, 119(4):438–444, 1997.

[51] Namrata Gundiah, Mark B Ratcliffe, and Lisa A Pruitt. Determination of strain energy function for arterial elastin: experiments using histology and mechanical tests. *Journal of biomechanics*, 40(3):586–594, 2007.

[52] Xinxiao Han, Hongyi Li, Wenda Hua, Luru Dai, Zhuo Ao, Fulong Liao, and Dong Han. Fluid in the tissue channels of vascular adventitia investigated by afm and tem. *Clinical hemorheology and microcirculation*, 67(2):173–182, 2017.

[53] Zvi Hashin. Analysis of composite materials—a survey. *Journal of Applied Mechanics*, 50(3):481–505, 1983.

[54] Darren Haskett, Gregory Johnson, Aifang Zhou, Urs Utzinger, and Jonathan Vande Geest. Microstructural and biomechanical alterations of the

human aorta as a function of age and location. *Biomechanics and modeling in mechanobiology*, 9(6):725–736, 2010.

[55] George M Hass. Elastic tissue. i. description of a method for the isolation of elastic tissue. *AMA Arch Pathol*, 34:807–819, 1942.

[56] Kozaburo Hayashi and Emiko Shimizu. Composition of connective tissues and morphometry of vascular smooth muscle in arterial wall of doca-salt hypertensive rats–in relation with arterial remodeling. *Journal of biomechanics*, 49(7):1225–1229, 2016.

[57] Michael R Hill, Xinjie Duan, Gregory A Gibson, Simon Watkins, and Anne M Robertson. A theoretical and non-destructive experimental approach for direct inclusion of measured collagen orientation and recruitment into mechanical models of the artery wall. *Journal of biomechanics*, 45(5):762–771, 2012.

[58] R Hill. The essential structure of constitutive laws for metal composites and polycrystals. *Journal of the Mechanics and Physics of Solids*, 15(2):79–95, 1967.

[59] Rodney Hill. Elastic properties of reinforced solids: some theoretical principles. *Journal of the Mechanics and Physics of Solids*, 11(5):357–372, 1963.

[60] Nicholas HG Holford, Hui C Kimko, Jon PR Monteleone, and Carl C Peck. Simulation of clinical trials. *Annual review of pharmacology and toxicology*, 40(1):209–234, 2000.

[61] A Gerhard Holzapfel. Nonlinear solid mechanics ii. 2000.

[62] Gerhard A Holzapfel, Thomas C Gasser, and Ray W Ogden. A new constitutive framework for arterial wall mechanics and a comparative study of material models. *Journal of elasticity and the physical science of solids*, 61(1-3):1–48, 2000.

[63] Gerhard A. Holzapfel, Gerhard Sommer, Christian T. Gasser, and Peter Regitnig. Determination of layer-specific mechanical properties of human coronary arteries with nonatherosclerotic intimal thickening and

related constitutive modeling. *American Journal of Physiology-Heart and Circulatory Physiology*, 289(5):–2048, 2005.

[64] Jay D Humphrey. Mechanics of the arterial wall: review and directions. *Critical Reviews^{TM} in Biomedical Engineering*, 23(1-2), 1995.

[65] Jay D Humphrey. Vascular adaptation and mechanical homeostasis at tissue, cellular, and sub-cellular levels. *Cell biochemistry and biophysics*, 50(2):53–78, 2008.

[66] Jay D Humphrey. *Cardiovascular solid mechanics: cells, tissues, and organs*. Springer Science & Business Media, 2013.

[67] Jay D Humphrey and Gerhard A Holzapfel. Mechanics, mechanobiology, and modeling of human abdominal aorta and aneurysms. *Journal of biomechanics*, 45(5):805–814, 2012.

[68] Jay D Humphrey, T Kang, P Sakarda, and M Anjanappa. Computer-aided vascular experimentation: a new electromechanical test system. *Annals of biomedical engineering*, 21(1):33–43, 1993.

[69] Jay D Humphrey and KR Rajagopal. A constrained mixture model for growth and remodeling of soft tissues. *Mathematical models and methods in applied sciences*, 12(03):407–430, 2002.

[70] Atsushi Ikai. *The world of nano-biomechanics*. Elsevier, 2016.

[71] Richard C Jin and Joseph Loscalzo. Vascular nitric oxide: formation and function. *Journal of blood medicine*, 1:147, 2010.

[72] Rebecca C Johnson, Jane A Leopold, and Joseph Loscalzo. Vascular calcification: pathobiological mechanisms and clinical implications. *Circulation research*, 99(10):1044–1059, 2006.

[73] Y Pedro Kato, David L Christiansen, Rita A Hahn, Sheu-Jane Shieh, Jack D Goldstein, and Frederick H Silver. Mechanical properties of collagen fibres: a comparison of reconstituted and rat tail tendon fibres. *Biomaterials*, 10(1):38–42, 1989.

[74] Joseph T Keyes, Darren G Haskett, Urs Utzinger, Mohamad Azhar, and Jonathan P Vande Geest. Adaptation of a planar microbiaxial

optomechanical device for the tubular biaxial microstructural and macroscopic characterization of small vascular tissues. *Journal of biomechanical engineering*, 133(7):075001, 2011.

[75] Joseph T Keyes, Danielle R Lockwood, Urs Utzinger, Leonardo G Montilla, Russell S Witte, and Jonathan P Vande Geest. Comparisons of planar and tubular biaxial tensile testing protocols of the same porcine coronary arteries. *Annals of biomedical engineering*, 41(7):1579–1591, 2013.

[76] Alex Khang, Daniel P Howsmon, Emma Lejeune, and Michael S Sacks. Multi-scale modeling of the heart valve interstitial cell. In *Multi-scale Extracellular Matrix Mechanics and Mechanobiology*, pages 21–53. Springer, 2020.

[77] Su-A Kim, Seong-Mi Park, Mi-Na Kim, Yong-Hyun Kim, Dong-Hyuk Cho, Chul-Min Ahn, Soon Jun Hong, Do-Sun Lim, and Wan Joo Shim. The relationship between mechanical properties of carotid artery and coronary artery disease. *European Heart Journal–Cardiovascular Imaging*, 13(7):568–573, 2011.

[78] Hiroaki Kitano. Computational systems biology. *Nature*, 420(6912):206, 2002.

[79] Ryan G Koch, Alkiviadis Tsamis, Antonio D'Amore, William R Wagner, Simon C Watkins, Thomas G Gleason, and David A Vorp. A custom image-based analysis tool for quantifying elastin and collagen micro-architecture in the wall of the human aorta from multi-photon microscopy. *Journal of biomechanics*, 47(5):935–943, 2014.

[80] Petra Kochova, Zbynek Tonar, Vit M Matejka, Jitka Sviglerova, Milan Stengl, and Jitka Kuncova. Morphology and mechanical properties of the subrenal aorta in normotensive and hypertensive rats. *Biomedical Papers of the Medical Faculty of Palacky University in Olomouc*, 152(2), 2008.

[81] Witold Krasny, Hélène Magoariec, Claire Morin, and Stéphane Avril. Kinematics of collagen fibers in carotid arteries under tension-inflation loading. *Journal of the mechanical behavior of biomedical materials*, 77:718–726, 2018.

[82] Witold Krasny, Claire Morin, Hélène Magoariec, and Stéphane Avril. A comprehensive study of layer-specific morphological changes in the microstructure of carotid arteries under uniaxial load. *Acta biomaterialia*, 57:342–351, 2017.

[83] Peter Lanzer, Manfred Boehm, Victor Sorribas, Marc Thiriet, Jan Janzen, Thomas Zeller, Cynthia St Hilaire, and Catherine Shanahan. Medial vascular calcification revisited: review and perspectives. *European heart journal*, 35(23):1515–1525, 2014.

[84] Kewei Li, Ray W Ogden, and Gerhard A Holzapfel. A discrete fibre dispersion method for excluding fibres under compression in the modelling of fibrous tissues. *Journal of The Royal Society Interface*, 15(138):20170766, 2018.

[85] Kewei Li, Ray W Ogden, and Gerhard A Holzapfel. An exponential constitutive model excluding fibres under compression: Application to extension–inflation of a residually stressed carotid artery. *Mathematics and Mechanics of Solids*, 23(8):1206–1224, 2018.

[86] Yaozhi Luo, Xian Xu, Tanmay Lele, Sanjay Kumar, and Donald E Ingber. A multi-modular tensegrity model of an actin stress fiber. *Journal of biomechanics*, 41(11):2379–2387, 2008.

[87] Franco Maceri, Michele Marino, and Giuseppe Vairo. An insight on multiscale tendon modeling in muscle–tendon integrated behavior. *Biomechanics and modeling in mechanobiology*, 11(3-4):505–517, 2012.

[88] Ryley A Macrae, Karol Miller, and Barry J Doyle. Methods in mechanical testing of arterial tissue: a review. *Strain*, 52(5):380–399, 2016.

[89] Sylvain Marchais, AP Guerin, B Pannier, G Delavaud, and Gérard London. Arterial compliance and blood pressure. *Drugs*, 46(2):82–87, 1993.

[90] Michele Marino. *Constitutive Modeling of Soft Tissues*. 01 2018.

[91] Michele Marino and Giuseppe Vairo. Multiscale elastic models of collagen bio-structures: from cross-linked molecules to soft tissues. In *Multiscale computer modeling in biomechanics and biomedical engineering*, pages 73–102. Springer, 2013.

[92] Arabella Mauri, Raoul Hopf, Alexander E Ehret, Catalin R Picu, and Edoardo Mazza. A discrete network model to represent the deformation behavior of human amnion. *Journal of the mechanical behavior of biomedical materials*, 58:45–56, 2016.

[93] Gregorio S Montes. Structural biology of the fibres of the collagenous and elastic systems. *Cell biology international*, 20(1):15–27, 1996.

[94] Tanaka Mori and K Tanaka. Average stress in matrix and average elastic energy of materials with misfitting inclusions. *Acta metallurgica*, 21(5):571–574, 1973.

[95] Claire Morin, Stéphane Avril, and Christian Hellmich. The fiber reorientation problem revisited in the context of eshelbian micromechanics: theory and computations. *Pamm*, 15(1):39–42, 2015.

[96] Claire Morin, Stéphane Avril, and Christian Hellmich. Non-affine fiber kinematics in arterial mechanics: a continuum micromechanical investigation. *ZAMM-Journal of Applied Mathematics and Mechanics/Zeitschrift für Angewandte Mathematik und Mechanik*, 2018.

[97] Claire Morin and Christian Hellmich. A multiscale poromicromechanical approach to wave propagation and attenuation in bone. *Ultrasonics*, 54(5):1251–1269, 2014.

[98] Kazuaki Nagayama and Takeo Matsumoto. Mechanical anisotropy of rat aortic smooth muscle cells decreases with their contraction. *JSME International Journal Series C Mechanical Systems, Machine Elements and Manufacturing*, 47(4):985–991, 2004.

[99] Mathieu Nierenberger. *Mécanique multiéchelles des parois vasculaires : expérimentation, imagerie, modélisation.* PhD thesis, Université de Strasbourg, 2013.

[100] Mary K. O'Connell, Sushila Murthy, Samson Phan, Chengpei Xu, JoAnn Buchanan, Ryan Spilker, Ronald L. Dalman, Christopher K. Zarins, Winfried Denk, and Charles A. Taylor. The three-dimensional micro-and nanostructure of the aortic medial lamellar unit measured using 3d confocal and electron microscopy imaging. *Matrix Biology*, 27(3):171–181, 2008.

[101] Keiko Ookawa, Masaaki Sato, and Norio Ohshima. Changes in the microstructure of cultured porcine aortic endothelial cells in the early stage after applying a fluid-imposed shear stress. *Journal of biomechanics*, 25(11):1321–1328, 1992.

[102] Michael F O'rourke and Junichiro Hashimoto. Mechanical factors in arterial aging: a clinical perspective. *Journal of the American College of Cardiology*, 50(1):1–13, 2007.

[103] N. Otsu. A threshold selection method from gray level histograms. *IEEE Trans. Systems, Man and Cybernetics*, 9:62–66, March 1979. minimize inter class variance.

[104] Hans Oxlund, Jan Manschot, and A. Viidik. The role of elastin in the mechanical properties of skin. *Journal of biomechanics*, 21(3):213–218, 1988.

[105] Maria-Ioana Pastrama, Stefan Scheiner, Peter Pivonka, and Christian Hellmich. A mathematical multiscale model of bone remodeling, accounting for pore space-specific mechanosensation. *Bone*, 107:208–221, 2018.

[106] Shelly R Peyton and Andrew J Putnam. Extracellular matrix rigidity governs smooth muscle cell motility in a biphasic fashion. *Journal of cellular physiology*, 204(1):198–209, 2005.

[107] Zsuzsanna Püspöki, Martin Storath, Daniel Sage, and Michael Unser. Transforms and operators for directional bioimage analysis: a survey. In *Focus on Bio-Image Informatics*, pages 69–93. Springer, 2016.

[108] KR Rajagopal and AR Srinivasa. On a class of non-dissipative materials that are not hyperelastic. *Proceedings of the Royal Society A: Mathematical, Physical and Engineering Sciences*, 465(2102):493–500, 2008.

[109] KR Rajagopal and AR Srinivasa. A gibbs-potential-based formulation for obtaining the response functions for a class of viscoelastic materials. *Proceedings of the Royal Society A: Mathematical, Physical and Engineering Sciences*, 467(2125):39–58, 2010.

[110] Mario Raspanti, Marina Protasoni, Alessandro Manelli, Stefano Guizzardi, Vittorio Mantovani, and Andrea Sala. The extracellular matrix of

the human aortic wall: ultrastructural observations by feg-sem and by tapping-mode afm. *Micron*, 37(1):81–86, 2006.

[111] Paul H Ratz. Mechanics of vascular smooth muscle. *Comprehensive physiology*, 6(1):111–168, 2011.

[112] Paul H Ratz. Mechanics of vascular smooth muscle. *Comprehensive physiology*, 2015.

[113] Paul H Ratz, Krystina M Berg, Nicole H Urban, and Amy S Miner. Regulation of smooth muscle calcium sensitivity: Kcl as a calcium-sensitizing stimulus. *American Journal of Physiology-Cell Physiology*, 288(4):C769–C783, 2005.

[114] Rana Rezakhaniha, Aristotelis Agianniotis, Jelle Tymen Christiaan Schrauwen, Alessandra Griffa, Daniel Sage, CVC vd Bouten, FN Van de Vosse, Michaël Unser, and Nikolaos Stergiopulos. Experimental investigation of collagen waviness and orientation in the arterial adventitia using confocal laser scanning microscopy. *Biomechanics and modeling in mechanobiology*, 11(3-4):461–473, 2012.

[115] Aaron Romo, Pierre Badel, Ambroise Duprey, Jean-Pierre Favre, and Stéphane Avril. In vitro analysis of localized aneurysm rupture. *Journal of Biomechanics*, 47(3):607–616, 2014.

[116] Charles S Roy. The elastic properties of the arterial wall. *The Journal of physiology*, 3(2):125–159, 1881.

[117] Sylvain Roy, Christophe Boss, Rana Rezakhaniha, and Nikos Stergiopulos. Experimental characterization of the distribution of collagen fiber recruitment. *Journal of Biorheology*, 24(2):84, 2010.

[118] Jean Salençon. *Handbook of continuum mechanics: General concepts thermoelasticity*. Springer Science & Business Media, 2012.

[119] Abbas Samani, Judit Zubovits, and Donald Plewes. Elastic moduli of normal and pathological human breast tissues: an inversion-technique-based investigation of 169 samples. *Physics in medicine & biology*, 52(6):1565, 2007.

[120] Zenon J Samila and Stefan A Carter. The effect of age on the unfolding of elastin lamellae and collagen fibers with stretch in human carotid arteries. *Canadian journal of physiology and pharmacology*, 59(10):1050–1057, 1981.

[121] Naoki Sasaki and Singo Odajima. Stress-strain curve and young's modulus of a collagen molecule as determined by the x-ray diffraction technique. *Journal of biomechanics*, 29(5):655–658, 1996.

[122] Stefan Scheiner, Peter Pivonka, and Christian Hellmich. Poromechanical stimulation of bone remodeling: a continuum micromechanics-based mathematical model and experimental validation. In *Poromechanics V: Proceedings of the Fifth Biot Conference on Poromechanics*, pages 1867–1876, 2013.

[123] JTC Schrauwen, A Vilanova, R Rezakhaniha, N Stergiopulos, FN Van De Vosse, and PHM Bovendeerd. A method for the quantification of the pressure dependent 3d collagen configuration in the arterial adventitia. *Journal of structural biology*, 180(2):335–342, 2012.

[124] Andreas J Schriefl, Georg Zeindlinger, David M Pierce, Peter Regitnig, and Gerhard A Holzapfel. Determination of the layer-specific distributed collagen fibre orientations in human thoracic and abdominal aortas and common iliac arteries. *Journal of the Royal Society Interface*, page rsif20110727, 2011.

[125] Igor Sevostianov and Mark Kachanov. On some controversial issues in effective field approaches to the problem of the overall elastic properties. *Mechanics of Materials*, 69(1):93–105, 2014.

[126] Zhilei L Shen, Mohammad Reza Dodge, Harold Kahn, Roberto Ballarini, and Steven J Eppell. Stress-strain experiments on individual collagen fibrils. *Biophysical journal*, 95(8):3956–3963, 2008.

[127] Frederick H Silver, Joseph W Freeman, Istvan Horvath, and William J Landis. Molecular basis for elastic energy storage in mineralized tendon. *Biomacromolecules*, 2(3):750–756, 2001.

[128] Michael Smith. *ABAQUS/Standard User's Manual, Version 6.9*. Dassault Systèmes Simulia Corp, United States, 2009.

[129] Dimitrios P Sokolis. Passive mechanical properties and structure of the aorta: segmental analysis. *Acta physiologica*, 190(4):277–289, 2007.

[130] Jonathan Stricker, Tobias Falzone, and Margaret L Gardel. Mechanics of the f-actin cytoskeleton. *Journal of biomechanics*, 43(1):9–14, 2010.

[131] Triantafyllos Stylianopoulos and Victor H Barocas. Multiscale, structure-based modeling for the elastic mechanical behavior of arterial walls. *Journal of biomechanical engineering*, 129(4):611–618, 2007.

[132] P Suquet. Effective properties of nonlinear composites. In *Continuum micromechanics*, pages 197–264. Springer, 1997.

[133] Lucas H Timmins, Qiaofeng Wu, Alvin T Yeh, James E Moore Jr, and Stephen E Greenwald. Structural inhomogeneity and fiber orientation in the inner arterial media. *American Journal of Physiology-Heart and Circulatory Physiology*, 298(5):H1537–H1545, 2010.

[134] Zbyněk Tonar, Petra Kochová, and Jiří Janáček. Orientation, anisotropy, clustering, and volume fraction of smooth muscle cells within the wall of porcine abdominal aorta. 2008.

[135] Zbyněk Tonar, Tereza Kubíková, Claudia Prior, Erna Demjén, Václav Liška, Milena Králíčková, and Kirsti Witter. Segmental and age differences in the elastin network, collagen, and smooth muscle phenotype in the tunica media of the porcine aorta. *Annals of Anatomy-Anatomischer Anzeiger*, 201:79–90, 2015.

[136] Zbyněk Tonar, Stanislav Nemecek, Radek Holota, Jitka Kocova, Vladislav Treska, Jiri Molacek, Tomáš Kohoutek, and Sarka Hadravska. Microscopic image analysis of elastin network in samples of normal, atherosclerotic and aneurysmatic abdominal aorta and its biomechanical implications. *J Appl Biomed*, 1(3):149–160, 2003.

[137] Jeffrey R Tonniges, Benjamin Albert, Edward P Calomeni, Shuvro Roy, Joan Lee, Xiaokui Mo, Susan E Cole, and Gunjan Agarwal. Collagen fibril ultrastructure in mice lacking discoidin domain receptor 1. *Microscopy and Microanalysis*, 22(3):599–611, 2016.

[138] Alkiviadis Tsamis, Jeffrey T Krawiec, and David A Vorp. Elastin and collagen fibre microstructure of the human aorta in ageing and disease: a review. *Journal of the Royal Society Interface*, 10(83):20121004, 2013.

[139] Tatsuo Ushiki. Collagen fibers, reticular fibers and elastic fibers. a comprehensive understanding from a morphological viewpoint. *Archives of histology and cytology*, 65(2):109–126, 2002.

[140] Tatsuo USHIKI and Masashi MURAKUMO. Scanning electron microscopic studies of tissue elastin components exposed by a koh-collagenase or simple koh digestion method. *Archives of histology and cytology*, 54(4):427–436, 1991.

[141] Joost AJ van der Rijt, Kees O van der Werf, Martin L Bennink, Pieter J Dijkstra, and Jan Feijen. Micromechanical testing of individual collagen fibrils. *Macromolecular bioscience*, 6(9):697–702, 2006.

[142] Bernard Van Varik, Roger Rennenberg, Chris Reutelingsperger, Abraham Kroon, Peter de Leeuw, and Leon J Schurgers. Mechanisms of arterial remodeling: lessons from genetic diseases. *Frontiers in genetics*, 3:290, 2012.

[143] Viktoria Vass, Claire Morin, Stefan Scheiner, and Christian Hellmich. Review of "universal" rules governing bone composition, organization, and elasticity across organizational hierarchies. In *Multiscale Mechanobiology of Bone Remodeling and Adaptation*, pages 175–229. Springer, 2018.

[144] J Vosshougi and HW Weizsäcker. Elastic properties of blood vessels in simple elongation. In *Biomechanics: Current Interdisciplinary Research*, pages 251–256. Springer, 1985.

[145] Jessica E Wagenseil and Robert P Mecham. Vascular extracellular matrix and arterial mechanics. *Physiological reviews*, 89(3):957–989, 2009.

[146] Joseph Walpole, Jason A Papin, and Shayn M Peirce. Multiscale computational models of complex biological systems. *Annual review of biomedical engineering*, 15:137–154, 2013.

[147] Hannah Weisbecker, David M Pierce, Peter Regitnig, and Gerhard A Holzapfel. Layer-specific damage experiments and modeling of human

thoracic and abdominal aortas with non-atherosclerotic intimal thickening. *Journal of the mechanical behavior of biomedical materials*, 12:93–106, 2012.

[148] Hannah Weisbecker, Michael J Unterberger, and Gerhard A Holzapfel. Constitutive modelling of arteries considering fibre recruitment and three-dimensional fibre distribution. *Journal of The Royal Society Interface*, 12(105):20150111, 2015.

[149] Sarah M Wells, B Lowell Langille, J Michael Lee, and S Lee Adamson. Determinants of mechanical properties in the developing ovine thoracic aorta. *American Journal of Physiology-Heart and Circulatory Physiology*, 277(4):H1385–H1391, 1999.

[150] Marco PE Wenger, Laurent Bozec, Michael A Horton, and Patrick Mesquida. Mechanical properties of collagen fibrils. *Biophysical journal*, 93(4):1255–1263, 2007.

[151] Thomas N Wight. Cell biology of arterial proteoglycans. *Arteriosclerosis: An Official Journal of the American Heart Association, Inc.*, 9(1):1–20, 1989.

[152] Alexandra Witthoft, Alireza Yazdani, Zhangli Peng, Chiara Bellini, Jay D Humphrey, and George Em Karniadakis. A discrete mesoscopic particle model of the mechanics of a multi-constituent arterial wall. *Journal of The Royal Society Interface*, 13(114):20150964, 2016.

[153] Harvey Wolinsky and Seymour Glagov. A lamellar unit of aortic medial structure and function in mammals. *Circulation research*, 20(1):99–111, 1967.

[154] Jiang Xiong, Shen Ming Wang, Wei Zhou, and Jan Guo Wu. Measurement and analysis of ultimate mechanical properties, stress-strain curve fit, and elastic modulus formula of human abdominal aortic aneurysm and nonaneurysmal abdominal aorta. *Journal of vascular surgery*, 48(1):189–195, 2008.

[155] Lanti Yang, Kees O Van der Werf, Carel FC Fitié, Martin L Bennink, Pieter J Dijkstra, and Jan Feijen. Mechanical properties of native and

cross-linked type i collagen fibrils. *Biophysical journal*, 94(6):2204–2211, 2008.

[156] Lanti Yang, KO Van der Werf, Pieter J Dijkstra, Jan Feijen, and Martin L Bennink. Micromechanical analysis of native and cross-linked collagen type i fibrils supports the existence of microfibrils. *Journal of the mechanical behavior of biomedical materials*, 6:148–158, 2012.

[157] Xunjie Yu, Yunjie Wang, and Yanhang Zhang. Transmural variation in elastin fiber orientation distribution in the arterial wall. *Journal of the mechanical behavior of biomedical materials*, 77:745–753, 2018.

[158] André Zaoui. Structural morphology and constitutive behaviour of microheterogeneous materials. In *Continuum micromechanics*, pages 291–347. Springer, 1997.

[159] André Zaoui. Continuum micromechanics: survey. *Journal of Engineering Mechanics*, 128(8):808–816, 2002.

[160] Shahrokh Zeinali-Davarani, Yunjie Wang, Ming-Jay Chow, Raphaël Turcotte, and Yanhang Zhang. Contribution of collagen fiber undulation to regional biomechanical properties along porcine thoracic aorta. *Journal of biomechanical engineering*, 137(5):051001, 2015.

[161] Yi Zhu, Hongyu Qiu, Jerome P Trzeciakowski, Zhe Sun, Zhaohui Li, Zhongkui Hong, Michael A Hill, William C Hunter, Dorothy E Vatner, Stephen F Vatner, et al. Temporal analysis of vascular smooth muscle cell elasticity and adhesion reveals oscillation waveforms that differ with aging. *Aging cell*, 11(5):741–750, 2012.

[162] Aikaterini Zoumi, Xiao Lu, Ghassan S Kassab, and Bruce J Tromberg. Imaging coronary artery microstructure using second-harmonic and two-photon fluorescence microscopy. *Biophysical journal*, 87(4):2778–2786, 2004.

Modélisation mécanique multi-échelle des tuniques de la paroi artérielle à partir de l'évolution des réseaux de fibres organiques

Résumé:

Les tissus artériels sont constitués de réseaux de collagène et d'élastine diversement organisés et présentent un comportement anisotrope hautement non linéaire avec la capacité de supporter de grandes déformations réversibles. Ces dernières s'accompagnent d'un réarrangement morphologique progressif de la microstructure induit par le chargement. Dans cette thèse, le rôle important de la microstructure sur la réponse artérielle macroscopique nous a motivé à développer un modèle multi-échelle détaillé de la paroi artérielle. Le modèle tient compte des motifs universels à différentes échelles dans les deux couches mécaniquement importantes des artères, à savoir l'adventice et la media. Le cadre de la micromécanique des milieux continus a été utilisé dans une approche incrémentale pour calculer la contrainte, la déformation et les réorientations de fibres. Les extensions du problème d'inclusion de la matrice d'Eshelby permettent d'obtenir des expressions analytiques pour les tenseurs de concentration, qui relient le tenseur de vitesse de déformation macroscopique à la vitesse de déformation et les tenseurs de spin moyennés sur les phases, à la vitesse de déformation appliquée macroscopiquement. Dans le modèle, la vitesse de déformation donne accès à la contrainte moyenne dans chaque phase, et le tenseur de spin permet de déterminer la rotation de la fibre induite par la charge. Le modèle adventitiel proposé tient compte à la fois de la déformation et du réalignement du collagène. La media est constituée d'un empilement de lamelles et d'un espace interlamellaire; les lamelles et l'espace interlamellaire sont tous deux homogénéisés à partir de VER. De plus, le modèle de comportement multi-échelle a été implémenté dans une formulation éléments finis, afin de réaliser des calculs de structure sur l'artère. Le modèle a été validé par rapport à différents ensembles de données expérimentales sur des échantillons artériels de différentes espèces (lapin, humain, souris). Les résultats montrent que le modèle est capable d'estimer la contribution de chaque composant dans la réponse macroscopique du tissu pour différents chargements et peut prédire avec précision à la fois la réponse macroscopique et la cinématique microscopique des fibres. Nous pensons qu'un tel modèle pourrait aider à prédire l'évolution de la réponse mécanique du tissu au fil du temps, par exemple lors d'un remodelage ou d'une lésion.

Mots-clefs : Micromécanique du continu, Homogénéisation, Elasticité à grande déformation, Tissus mous, Modélisation constitutive, Méthode des éléments finis non linéaires.

LAYER-SPECIFIC MULTISCALE MECHANICAL MODELING OF ARTERIAL STRUCTURES WITH EVOLVING FIBER CONFIGURATIONS

Abstract:
Arterial tissues are made of variously organized collagen and elastin networks and exhibit a highly nonlinear anisotropic behavior with the ability to sustain large reversible strains and to undergo a load-induced progressive morphological rearrangement of the microstructure. In the present study motivated by these specificities of arterial mechanics, we developed a detailed multi-scale model of the arterial wall. The model accounts for the universal patterns across different scales in the two mechanically significant layers of arteries, namely the adventitia and the media. The framework of finite strain continuum micromechanics was employed in an incremental approach to compute stress, strain, and fiber reorientations. The extensions of Eshelby's matrix-inclusion problem allowed for deriving analytical expressions for the concentration tensors. These concentration tensors relate the macroscopic strain rate tensor to the strain rate and spin tensors averaged over the constituents of the microstructure, to the macroscopically applied strain rate. In the model, the strain rate is related to the averaged stress in each constituent, and the spin tensor is related to the load-induced fiber rotation. The proposed adventitial model accounts for both collagen decrimping and realignment. The media is modeled as a stack of lamellae and interlamellar space; both lamellae and interlamellar space being homogenized with relevant representative volume element (RVE). Furthermore, the multi-scale constitutive model was implemented in a finite element formulation to solve the structural model of the artery. The model was validated against different experimental data sets on arterial samples from different species (rabbit, human, mouse). The results show that the model is able to estimate the contribution of each component into the macroscopic response of the tissue for different loading and can predict both the macroscopic response and microscopic fiber kinematics accurately. We submit that such model would help in predicting the evolution of the mechanical tissue response overtime during, for instance, remodeling and growth or damage.

Keywords: Continuum micromechanics, Homogenization, Large strain elasticity, Soft tissue, Constitutive modeling, Nonlinear finite element method.